ISTANBUL TECHNICAL UNIVERSITY ★ GRADUATE SCHOOL OF SCIENCE ENGINEERING AND TECHNOLOGY

AN INVESTIGATION OF PHASE TRANSITIONS IN SELF-ASSEMBLED PEPTIDE NANOTUBES USING DIELECTRIC AND INFRARED SPECTROSCOPY

M.Sc. THESIS

Abuzer Orkun AYDIN

Department of Physics Engineering

Physics Engineering Programm

MART 2020

ISTANBUL TECHNICAL UNIVERSITY ★ GRADUATE SCHOOL OF SCIENCE ENGINEERING AND TECHNOLOGY

AN INVESTIGATION OF PHASE TRANSITIONS IN SELF-ASSEMBLED PEPTIDE NANOTUBES USING DIELECTRIC AND INFRARED SPECTROSCOPY

M.Sc. THESIS

Abuzer Orkun AYDIN
(509181101)

Department of Physics Engineering

Physics Engineering Programme

Thesis Advisor : Prof. Dr. Ferid SALEHLİ

MART 2020

ISTANBUL TEKNİK ÜNİVERSİTESİ ★ FEN BİLİMLERİ ENSTİTÜSÜ

**KENDİLİĞİNDEN ORGANİZE PEPTİD NANOTÜPLERDE
MEYDANA GELEN FAZ GEÇİŞLERİNİN
DİELEKTRİK VE KIZILÖTESİ SPEKTROSKOPİ İLE İNCELENMESİ**

YÜKSEK LİSANS TEZİ

Abuzer Orkun AYDIN

(509181101)

Fen Bilimleri Enstitüsü

Fizik Mühendisliği Programı

Tez Danışmanı: Prof. Dr. Ferid SALEHLİ

MART 2020

Abuzer Orkun Aydın, a M.Sc. student of İTU Graduate School of Science Engineering and Technology student ID 509181101, successfully defended the thesis entitled "AN INVESTIGATION ON PHASE TRANSITIONS IN PEPTIDE NANOTUBES USING DIELECTRIC AND INFRARED SPECTROSCOPY", which he prepared after fulfilling the requirements specified in the associated legislations, before the jury whose signatures are below.

Thesis Advisor :   **Prof. Dr. Ferid Salehli**   ....
                         İstanbul Technical University

Jury Members :   **Prof. Dr. Faik MİKAİLZADE**   ....
                         Gebze Technical University

                         Prof. Dr. Hakan Özgür ÖZER   ....
                         Istanbul Technical University

Date of Submission : 10 March 2020
Date of Defense   : 26 March 2020

To my wife,

FOREWORD

This thesis was financially supported by TÜBİTAK 115F227 project in collabration with FCT Portugal and Aveiro University.
This thesis is a product of rough times in my life. I specially thanks for all the understanding and help of Prof. Dr. Ferid Salehli.

TABLE OF CONTENTS

ABBREVIATIONS

FF NT/MT : Diphenylalanine nanotube/microtube

BDS : Broadband dielectric spectrosopy

FTIR : Fourier transform infrared spectroscopy

XRD : X-ray Diffraction

QENS : Quasielastic Neutron Scattering

NMR : Nuclear Magnetic Resonance

PLAS : Positron Lifetime Annihiliation Spectroscopy

VFT : Vogel-Fulcher-Tamman

MCM-41 : Mobile Composition of Matter Number – 41

LLCP : Liquid-Liquid Phase Transition

FSC : Fragile-to-Strong Phase Transition

TMD : Temperature of Maximum Density

LDL : Low Density Liquid

HDL : High Density Liquid

LDA : Low Density Amorph

HDA : High Density Amorph

SYMBOLS

ε	: Dielectric Constant
ε'	: Real Part of the Dielectric Constant
ε''	: İmaginary Part of the Dielectric Constant
τ	: Relaxation Time
ω	: Frequency
k	: Wavenumber
T	: Temperature
k_B	: Boltzmann constant
E_A	: Activation Energy
α	: Thermal Expansion Coefficient
k_T	: Isothermal Compressiblity
c_P	: Isobaric Heat Capacity
ρ	: Density
S	: Entropy
V	: Molar Volume
T_S	: Singularity Temperature
T_g	: Glass Transition Temperature
T_f	: Freezing Temperature
T_H	: Homogeneous Nucleation Temperature
T_x	: Crystallisation Temperature
μ	: Dipole Moment
Q	: Normal Coordinates

LIST OF TABLES

AN INVESTIGATION OF PHASE TRANSITIONS IN SELF-ASSEMBLED PEPTIDE NANOTUBES USING DIELECTRIC AND INFRARED SPECTROSCOPY

SUMMARY

Discovery of self-assembly processes of cyclic and aromatic peptide opened new opportunities for biomimetic functional materials, which can pave the way to bottom-up engineering of environmental friendly electronics or optics. Especially, self-assembly of diphenylalanine peptides in aqueous solutions results in highly organised microtubes consists of hexagonal nanotubes (FF NT/MT) with high structural and chemical stability. Furthermore, diphenylalanine nanotubes are claimed to posses electronic, optical and many non-linear polarisation properties such as ferroelectricity. The origin of its properties are believed to be its lattice structure by many researchers. Despite great effort was made, for twenty years, on FF NT/MT a feasible application is not yet discovered. We believe that any further attempt will be futile, unless the the structure of the peptide nanotubes and the origin of their physical properties are fully understood.

In primary structure, diphenylalanine molecules contains of two hydrophobic phenyl rings, one carboxyl group and one protonated amino group. The later two moieties residing on the opposite ends of the molecule, build head-to-tail chains with adjacent FF molecules forming a dipeptide hexamer unit closing around the water molecules trapped inside. This structure expands parallel to the normal of FF hexamer plane and forming the nanotubes with a van-der Waals diameter of 10 Å. Outlying hydrophobic phenyl rings joined together with π-π interactions completing the microtube structure. Completed peptide backbone has a well-defined hexagonal lattice structure $P6_1$. Periodically arranged functional groups provide H-Bond donor and acceptor sites. Together with the water wire stretching along the c-axis of nanotubes, there exists three nanoconfinement regions in FF NT/MT. Relatively larger free volume between the hexagonal rings has to be considered as an additional sites for residing water molecules.

Water has extensive hydrogen bonded tetrahedral network, which differentiates itself from simple liquids of similar molecular weigh and structure. Anomalous nature of water known to be an outcome its structure. In search for the origings of observed phenomena, researchers were able to cool water down to 229 K. Nevertheless, for measurements on bulk water it is near impossible to enter the so called 'No man's land', where spontaneous crystalisation is unavoidable.

Confined water has special attributes such as the ability to by-pass crystalisation and enter into 'No Man's Land'. Pioneering measurements on confined water in nanoporous materials or solutions provided many fullfiling information. Besides, many authors revealed couplings between dynamical or vibrational properties of hydration water and proteins such as lysine or lyzozyme. In accordance with these later findings, water is accepted as constituent of protein or polypeptide dynamics and structure.

Even though FF NT/MT is a system of dipeptide sequences, we assume that it's properties are defined by its inherent, confined water molecules as in proteins. Keeping that in mind, we employed Broadband Dielectric Spectroscopy (BDS) and Fourier Transform Infrared Spectroscopy (FTIR) in wide temperature ranges to investigate dynamical and vibrational properties of confined water in FF NT/MT.

BDS experiments are conducted in wide frequency (10^{-2} Hz – 10^{9}) and temperature (100 K – 450 K) range. We have revealed successive phase transitions of water molecules confined in 1nm hexamer rings and between hexamer rings in FF peptide, former having a slower process. In the vicinity of 195 K, dielectric measurements revealed the onset of long-range tetrahedral hydrogen bond ordering between water molecules in distinct regions. As a result of a structural phase transition at about 230 K, frustration of hydrogen bonds leads to local tetrahedral arrangements. Exothermic trend of DSC curve in temperature range 160 K-230K and the singularity at 230 K, reinforces the claim of ordering dipoles and structural phase transition, respectively. DSC measurements on FF NT/MT confirms the structural phase transition at 230 K, with a singularity in heat flow signal. Two glass transitions at 205K and 133K are found related with water clusters in distinct confinement regions. Dielectric response maximum at room temperature can be understood as increased reorientational contribution of water dipoles due to loss of long-range interactions. This later finding gives a clue about the observed phenomena related with polarization.

The vibrational characteristics of both confined water and peptide backbone is revealed in FTIR spectroscopy in MIR region (1000 cm^{-1} – 6000 cm^{-1}) and in temperature range between 88 K and 320 K. Three specific spectral region is identified; OH-Stretching band (3000 cm^{-1} – 3500 cm^{-1}), CH-Stretching band (2820 cm^{-1} – 2980 cm^{-1}) and combination of Amide I/II vibrations with OH-Bending (1470 cm^{-1} – 1700 cm^{-1}). OH-Stretching is deconvoluted into 6 Gaussian modes related with confined water with a split about 3250 cm^{-1}, indicating strong coupling with peptide backbone. This split disappeared as temperature is approached to phase transition at 195 K, where an abrupt increase in infrared absorbance intensity is observed. The band shape remained the same resembling tetrahedral water network until the second phase transition at about 230 K. Above 230 K, long-range tetrahedral range is lost and intensity of OH-Stretching bonds are frustrated. These phase transitions are in line with the dielectric measurements. Further evidence of peptide-water coupling is obtained in CH-Stretching and Amide I/II region, where band intensities are sensitive to mentioned phase transitions.

In conclusion, we have revealed the structure and explicit phase transitions of water confined in self-assembled diphenylalanine nanostructures. The observed phase transitions are first in literure concerning the confined water and FF NT/MT. We claim, depending on our results, that observed functional properties of FF NT/MT are caused by dipole contributions of confined water in the system.

KENDİLİĞİNDEN ORGANİZE PEPTİD NANOTÜPLERDE MEYDANA GELEN FAZ GEÇİŞLERİNİN DİELEKTRİK VE KIZILÖTESİ SPEKTROSKOPİ İLE İNCELENMESİ

ÖZET

Halkalı ve aromatik peptitlerin kendiliğinden–organizasyon süreçlerinin keşfi, biyomimetik fonksiyonel malzemelerin "sondan-başa" mühendisliği ile geri dönüştürebilirliği yüksek elektronik ve ya optik cihazların üretimi konusunda yeni ufuklar açtı. Özellikle, kendiliğinden-organize difenilalanin peptitlerin sulu çözeltilerde ve oda sıcaklığında sentezi ile ortaya çıkan heksagonal nanotüp/mikrotüp (FF NT/MT) sistemleri sergiledikleri yüksek mekanik ve kimyasal kararlılık nedeniyle oldukça merak uyandırdı. Yapılan incelemeler sonucunda, FF NT/MT'ni n oda sıcaklığında elektronik, optik ve pek çok doğrusal-olmayan polarizasyonla ilişkili , ferroelektrik etki gibi, özelliklerinin olduğu ortaya çıktı. Daha önceki çalışmalarda, fonksiyonel özellikleri, bilinen benzer özelliklere sahip katı-hal cisimlerde olduğu gibi merkezcil simetrisi olmayan heksagonal kristal yapıdan kaynaklandığı öne sürüldü. Buna rağmen, yaklaşık 20 yıldır süre gelen araştırmacalar sonucu difenilalanin peptitlerle uygulanabilirliği olan bir teknoloji ortaya konulamadı. FF NT/MT yapısı doğru bir şekilde ortaya konmadığı ve fonskiyonel özelliklerinin kaynağı doğru bir şekilde anlaşılmadığı sürece diğer denemelerin de başarısızlıkla sonuçlanacağını düşünüyoruz.

Difenilalanine peptitlerin birincil yapısı, iki adet hidrofobik phenyl grubunun bir alanin ile birleşmesiyle oluşmaktadır. Bu yapıda iki adet hidrofobik fenil grubunun yanı sıra, negatif yüklü karboksil ve pozitif yüklü amino grubu bulunmaktadır. Bu hidrofilik gruplar, birincil yapıdaki difenilalanin moleküllerinin sulu çözeltiye sokulmasıyla birlikte aralarında hidrojen bağı kurarak "baştan-kuyruğa" zincirlerle dipeptide (FF) altıgen ünitesini oluşturmaktadır. Dahası, bu yapısı FF hexamer yüzey normaline paralel bir şekilde c-ekseni boyunca birleşerek su moleküllerini hidrofilik iç yüzeyde tuzaklamaktadır. Bu şekilde meydana gelen nanotüpün Van-der-Waals çapı 1 nm olarak belirlenmiştir. Yapılan kristalografik çalışmalarda bu yapının $P6_1$ heksagonal örgüsü ortaya konmuştur. Oluşan nanotüpler hidrofobik fenil gruplarının (π-π) istiflenmesi ile birbirine bağlanarak boyutları uzunlukları 100 - 500 µm arasında değişen mikrotüpleri meydana getirmektedirler. Mikrotübün merkezinde hidrofobik bir kanal bulunmaktadır. Meydana gelen FF NT/MT sisteminde su molekülleri FF nanotüplerin hidrofilik iç yüzeylerinde periyodik bir şekilde yerleşmiş olan karboxil ve amino gruplarına bağlı bir şekilde tuzaklanmış olarak c-ekseni boyunda dizilmiş bir "su kablosu"nu meydana getirmektedir. Dahası, heksagonal halkarın arasında oluşan görece olarak daha büyük serbest hacimlerde kalmış su ile birlikte su dağılımı birbirinden bağımsız şekilde iki ayrı nanotuzaklanmada yerleşmektedir.

Su moleküllerinin yaygın hidrojen bağları ile birbirine bağlanarak tetrahedral su ağı oluşturması, aynı moleküler kütleye sahip diğer moleküllerde rastlanmayan fiziksel özellikler göstermesine yol açmaktadır. Suya ait herkesçe bilinen anomalilerin

kaynağında bu yapının yattığı öne sürülmüştür. Hidrojen bağlarının enerjisi kovalent bağ ile Van-der-Waals bağ enerjileri arasında kalarak, su moleküllerinin oda sıcaklığında sıvı halde kalmasını sağlamaktadır. Dahası, düşük sıcaklıklara gidildikçe artan hidrojen bağı düzen parametresi, suya ait termodinamik tepki fonsksiyonlarında görülen anomalilere kaynak olmaktadır. Bahsi geçen, fenomenlerin kaynağına inebilmek amacıyla araştırmacılar yığın suyu 229 K sıcaklığına kadar soğutmayı başardılar. Ancak, ani kristalleşme "İnsansız Bölge" olarak adlandırılan ve homojen çekirdeklenme ile kesin bir şekilde sınırı çizilmiş olan bölgeye giren ölçümlerin yapılmasını imkansız hale getirmektedir.

Tuzaklanmış su, kristallenmeyi atlayarak "İnsansız Bölge"ye girebilmek gibi bir özelliğe sahiptir. Bu özelliği kullanarak yapılan çalışmalar, nanogözenekli yapılarda ve ya yoğun çözeltilerde aşırısoğutulmuş suyun incelenmesine olanak sağlayarak oldukça yararlı bilgiler edinilmesini sağlamıştır. Ayrıca, bazı çalışmalar lizin ve ya lizozim gibi proteinlerde tuzaklanmış suyun özellikleri ile proteinlerin dinamik ve titreşimsel özellikleri arasında ilişkilerin bulunduğunu göstermişler. Benzer bulguların ışığında, suyun polipeptit ve protein dinamiğin ana bileşenlerinden biri olduğu iddia edilmektedir.

FF NT/MT sistemi bir dipeptit yapısı olduğundan dolayı, sistem içerisinde tuzaklanmış olan suyun difenilalaninin yapısal ve fonksiyonel özelliklerinden sorumlu olduğunu düşünmekteyiz. Bu hipotezi araştırmak adına FF NT/MT geniş sıcaklık aralığında Genişbandt Dieletrik Spektroskopi (GDS) ve Fourier Dönüşümlü Kızılötesi Spektroskopi (FDKS) uygulanarak dinamik ve titreşimsel özellikleri incelenmiştir.

GDS ölçümleri geniş frekans (10^{-2} Hz– 10^9 Hz) aralığında ve 100 K- 450 K sıcaklıkları arasında yapılmıştır. İncelemeler sonucunda, 1nm FF heksamer örgüde kısıtlanmış su moleküllerine ait ardışıklı faz geçişlerini tespit ettik. Bahsedilen heterojen iç hacim, görece hızlı ve görece yavaş dielektrik süreçlerin varlığını ortaya koydu. 195 K sıcaklığında ortaya çıkan faz geçişi, uzun-menzilli tetrahedral su örgüsnün tamamlanarak farklı tuzaklanmalarda su gruplarının birbirine bağlandığını göstermektedir. Ardından 230 K'de gerçekleşen faz geçişi ile hidrojen bağları kırılarak bu örgü sonlanmış ve kısa menzilli yerel düzenler meydana gelmiştir. Yapılan Diferansiyel Taramalı Kalorimetri (DTS), bu gözlemlerle uyumlu olarak 195 K'de ısı akışı sinyalinde değişim ve 230 K'de bir tekillik göstermektedir. Ayrıca 160 K – 230 K aralığında gözlemlenen exothermic süreç hidrojen bağlarının kurulduğu bilgisini doğrulamaktadır. İki farklı tuzaklanma pozisyonunda bulunan su gruplarına ait camsı geçiş sıcaklıkları, 205 K ve 133 K olarak saptanmıştır. Oda sıcaklığında gözlemlenen dielektrik geçirgenlik maksimum değeri, tetrahedral örgüden bağımsız kalmış su moleküllerinin döngüsel dipol katkılarını göstermektedir. Bu son bulgu, FF NT/MT ye ait polarizasyonla ilişkili gözlemlenmiş bulguların su molekülleri ile ilişkili olduğunu göstermektedir.

Fourier Dönüşümlü Kızılötesi Spektroskopi incelemeleri, (1000 cm^{-1} – 6000 cm^{-1}) aralığında ve 88 K-320 K sıcaklıkları arasında uygulanmıştır. Sonuç olarak üç farklı titreşim bandı bulunmuştur. Bunlar; OH-gerilme bandı (3000 cm^{-1} – 3500 cm^{-1}), CH-gerilme bandı (2820 cm^{-1} – 2980 cm^{-1}) ve Amide I/II bandı ile OH-bükülme bandının kombinasyonundan (1470 cm^{-1} – 1700 cm^{-1}) oluşmaktadır. OH-gerilme bandı ikiye ayrılmış şekilde FF NT/MT içerisindeki su konumlarının heterojenliğini göstermektir. OH-gerilme bandına ait Gauss modları 195 K'de pik yapıp 230 K e kadar aynı düzeyde seyretmektedir. 230 K'den yüksek sıcaklıklarda ise soğrulma şiddetleri tükenmiştir. Bu gözlem dielektrik spektroskopi sonuçları ile aynı sonuca işaret etmektedir. CH-

gerilme bandı faz geçişlerinde tepki vererek peptit-su ilişkisini ortaya koymuştur. Aynı gözlem Amide I/II ve OH-bükülme bantlarının ortaklaşa dinamiklerinde de görülmektedir.

Sonuç olarak, FF NT/MT sisteminde tuzaklanmış su moleküllerinin yapısı ve faz geçişleri ortaya konmuştur. Bu faz geçişleri literatürde bir ilktir. Sonuçlarımız, FF NT/MT fonksiyonel özelliklerinin sistem içerisinde bulundan su molekülleri ile ilişkili olduğunu göstermektedir.

1. INTRODUCTION

Complex biomaterials possesing high levels of geometrical organization are frequent in nature. Life itself is a result of electrochemical and mechanical interactions between this highly organised substances like carbohydrates, lipids and peptides. Despite, the top-down approach of synthetic materials, this building blocks of life are following a bottom-up design, in other words self-assembly processes [1]. This newly discovered phenomenon has encouraged researchers to apply similar approaches to build stuctures beyond resolution limits [2]. Understanding structure and properties of self-assembled macromolecules is essential to achieve success in engineering of functional biomaterials.

Investigation of self-assembled peptides have been pioneered by Ghadiri *et.al.* with the discovery of cyclic peptide nanotubes [3]. They've gathered lattice parameters, using X-ray diffraction and vibrational spectroscopy of the material displaying periodically assembled hollow nanotubes. Potential of constructing biomimetic ion channels, nanotemplates for metal casting or confining environment for molecules using these tubular materials urged researchers to investigate similar peptide structures.

Diphenylalanine (H-Phe-Phe-OH, FF) is a short aromatic dipeptide which is the core recognition motif of Amyloid-β which is responsible for many neurodegenerative diseases such as Alzheimer[4]. Besides, authors have shown that naturaly occuring amyloids also self-assemble into bionanomaterials as functional fibers in fungie and bacteria or protective films in egg envelopes. Using FF monomers, researchers developed a method to trigger nanotube(NT) self-assembly, which then bundles into microtubes (MT)[5]. FF nanotubes posses well defined crystallographic hexagonal structure. Water is confined in the hydrophilic channels composed of FF hexamers packed via π-π interactions.

Starting with the seminal work of Görbitz *et.al.* there has been series of researchs on properties and self-assembly process on FF nanotubes. Unique electronic[6] and optical [7,8] combined with high rigidity [9] and chemical stability [10] makes FF NT/MT a promising biodegradable canditate for electronic or optical waveguide applications. Furthermore, by controlling the effects of nonlinear polarization such as piezoelectricity [11,12] and second harmonic generation [13,14] new designs for micromechanical or microelectronic switches can be developed. Recently, energy harvesters based on piezoelectricity observed in FF MT/NT have been suggested for biomedical purposes [15]. Reversible piezoresponse in self-assembled peptide nanotubes under an external electric field indicates its potentials as an environmental friendly ferroelectric material[11,16].

Water molecules play crucial role both in the self-assembly process and stability of the FF NT/MT [17,18]. Protonated amino and carboxyl functional groups in the inner surface of nanotubes provide abundant sites for H-Bond formation[19]. Water molecules locate according to the periodical distribution of these moieties and the water network in the core of hydrophilic nanochannel is formed through extensive H-Bond. It should be noted that the Van-der-Waals diameter of the peptide nanotubes is about 1 nm[5].

Studies have shown that water crystallization and glass transition can be avoided in confinements with diameters less than 3 nm [20, 21, 22]. Consequently, confined water has paved a way to probe 'no-man's land' between 150 K - 230K, where otherwise the spontaneous crystallisation makes it quite difficult for measurements in bulk water [24, 25].

As suggested by Ghadiri *et al* [3], peptide nanotubes provide a confining environment for the molecules such as water. Probing kinetics and thermodynamics of FF NT/MT can provide valuable information about both peptide-water interplay and 'no man's land'. Furthermore, we believe that functional properties of self-assembled diphenylalanine nanostructures arise from the anomalous behavior of confined water in the system.

As seen in the literature, nonlinear effects observed in FF NT/MT are attributed to nonsymmetric peptide lattice [23]. But, it can be supposed that, ordered and periodical locations of H_2O molecules with high dipole moments plays an important role in observed physical properties of FF peptides.

Regarding dynamics of confined water in the literature [22], it is aimed to investigate the dielectric permittivity and dynamic properties of water molecules confined in FF NT/MT. Therefore, Broadband Dielectric Specktroscopy (BDS) in wide frequency (10^{-2} Hz – 10^9 Hz) and temperature range (90K – 450 K) used.

Diferent confinements of water molecules in peptide nanochannel imposes different constraints of hydrogen bonded network. Consequently, it is expected to observe this heterogenity on the vibrational spectrum of water. For this reason, Fourier Transform (FTIR) Infrared Spectroscopy in wide frequency (1000 cm^{-1} – 6000 cm^{-1}) an temperature (90 K – 330 K) is used. FTIR experiments are focused on OH-stretching and OH-bending modes.

In this thesis, dynamic and vibrational properties of FF NT/MT system are investigated by BDS and FTIR to understand the origins of physical properties of self-assembled diphenylalanine nanostructures in direct relation with the properties of confined, supercooled water.

The thesis structure is organised follows: Chapter 1 is devoted to introduction, where general interests of the current is drawn with the statement of the purpose. In Chapter 2, a short review of literature regarding diphenylalanine is given with its structure and general aspects of self-assembly process. Furthermore, a summary of FF NT/MT's phyiscal properties are given. Literature review of water's anomalies, supercooled and confined water are presented in Chapter 3. Related work with our research are summarised to give insight about the inherent problems. In Chapter 4, we present the details and results with discussions of the broad temperature (100 K – 450 K) BDS measurements on FF NT/MT. Next, in Chapter 5, we present details and results with discusion of FTIR measurements in temperature range 90 K to 320 K. Obtained results are summarised in Chapter 6. Finally, concluding remarks have been drawn in Chapter 7.

2. SELF-ASSEMBLED DIPHENYLALANINE PEPTIDE MICRO/NANOTUBES

In last twenty years, there have been vast amount of work on the diphenylalanine macromolecules due to it's pronounced potential for bottom-up biomimetic engineering. Researchers utilized diverse experimental and computational methods to reveal the properties of self-assembled FF structures.

2.1 Structure of Self-Assembled Diphenylalanine Nanotubes

FF molecules consist of two covalently bonded phenylalanine amino acids. Primary structure hosts two hydrophobic phenyl rings besides one hidrophilic carboxyl (COO^-) and one protonanted amino ($NH3+$) functional group (Figure 2.1).
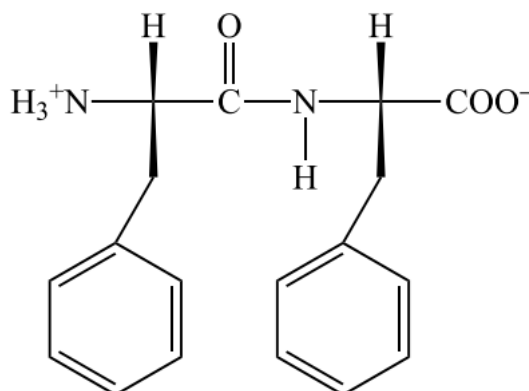
Figure 2.1: Primary structure of L-Phe-L-Phe (FF) [5].

In his work, Görbitz obtained lattice paramaeters of self-assembled FF NT/MT data using XRD; a=b=24.0709, c=5.4560 which belongs to non-symmetric $P6_1$ space group [5]. Six diphenylalanine molecules form the hexamer via H-Bonds between amino and carboxyl moeities, which is why it is called head-to-tail structure. The remaining H atom in amino and hydrogen acceptor carboxyl groups is bound with non-covalent bonds with the confined water molecules on the surface of FF hexagonal rings. The remining space is filled with water molecules following the periodicity provided by the proton donor and acceptor groups in the peptide backbone (Figure 2.2). This simple motif is wrapped around c-axis building 3D structure. Aromatic (π-π) interactions

between phenyl rings forces nanotubes to bundle and form the microtubes with tubular walls [19, 26, 27].
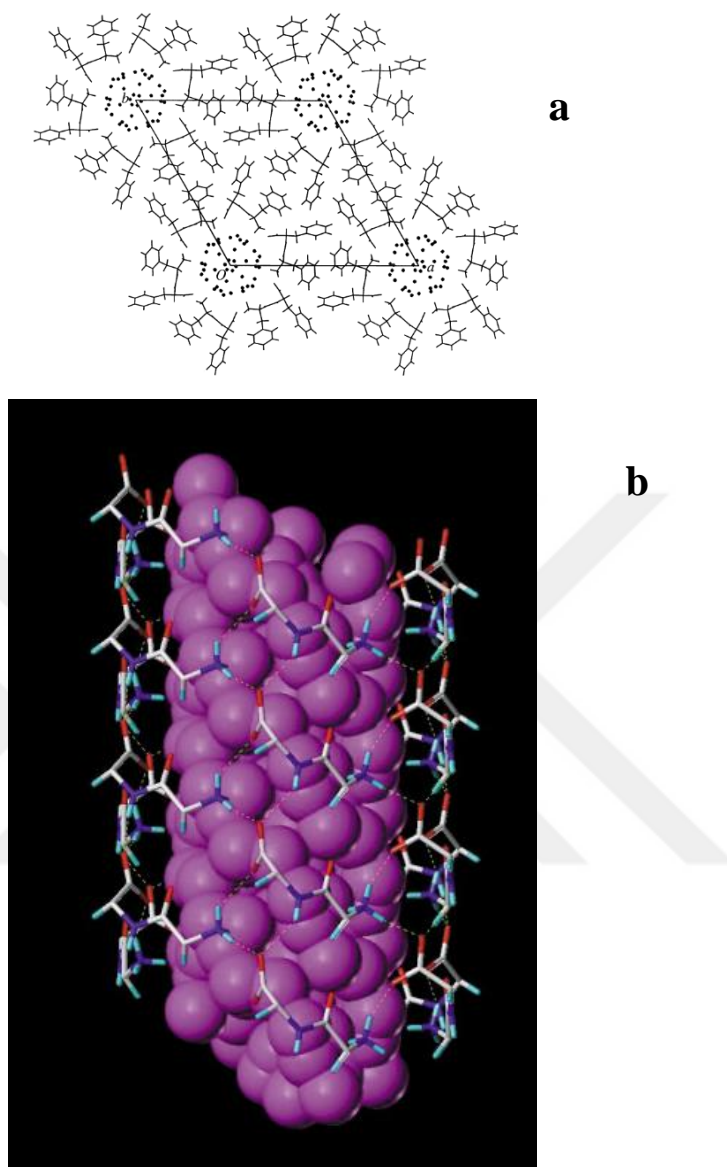
Figure 2.2: (a) Unit cell of FF NT/MT. View from basal plane (0001). Dots denote water molecules. (b) Water molecules occupations in the nanochannel of diphenyalanine nanotubes according to Görbitz. Dashed lines show hydrogen bonds between NH_3^+ and COO^- functional groups [5].

Hidrophilic versus hydrophobic interactions drive the self-assembly process. Andrade-Filho *et al* used theoretical calculations, demonstrating same results with the experimental data obtained by Görbitz, to demonstrate the role of solvent concentration on FF self-assembly. His group obtained concluding evidence that by 20-21 water molecule per hexamer the hexagonal FF NT/MT the structure becomes

stable[27]. With lesser water molecules, a transition into orthorombic symmetry occurs. Thus a certain solvent ratio is needed to obtain FF NT/MT.

Researchers have obtained nanofibers, microrods [7], nanovesicles [17] by controlling water and FF concentration or sonification duration. These systems are irrelevant with this research.

2.2 Diphenylalanine Self-Assembly Process

Basic approach to trigger FF NT/MT self-assembly has two steps. First, by detanuration, dipeptide molecules are decomposed to their primary structure in different solvents. Second, by hydration, hydrophilic vs hydrophobic dynamics is triggered.

Görbitz et.al. used alcohol/DMSO solvent for the denaturation process. Then rapid evaporation of aqueous solution with concetration about 5-200 mg mL at 80 °C finalised the hydration and so FF NT/MT self-assembly [5]. In his work the method demonstrated somehow obscure.

Reches and Gazit, provided a clear approach [29]. Lyophilized peptides are solved in organic solvent 1,1,1,3,3,3 hexafluora-2-propanol (HFP) with a concentration above 100 mg mL^{-1}. After the acqueous solution is obtained in μm range peptide nanotube self-assembly ended within seconds.

Soon after unique properties of FF NT/MT is observed researchers looked for methods allign microtubes. Combining their method with rapid evaporation Reches and Gazit menaged to grow vertically alligned FF microtubes on siliconized glass [30]. Another method used for vertical aligned FF NT/MT (nanoforest) is PVD. Researchers used peptide monomer solved in HFP to coat any surface [31]. The last technique reported for horizontal alignment of microtubes by pulling a substrate out of the peptide HFP solution with certain velocities [15]. It has to be noted that apart from the standard method employed by Reches and Gazit the resulting nanotubes have different structural and physical properties. Thus our investigation on peptide nanotubes will be limited by diphenylalanine synthesis by standard method only as described in [29].

2.3 Properties and Potential Applications of FF NT/MT

Self-assembled diphenyalanine structures are investigated by many researchers to gather their physical properties.

Rigidity of diphenylalanine nanostructures are measured by Kol *et al* [32] with AFM tip by indenting individual microtubes ranging from 100nm to 300nm in diameter. Point stiffness of microtubes is obtained from the derivative of force-distance curve as 160 N/m. They utilized a finite element calculation using the tube stiffness data to calculate the Young's modulus as about 19 GPa. Lijiang Niu's group used the beam bending method with AFM to investigate the elasticity of the microtubes [33]. They obtained the Young's modulus about 27 GPa and also shear modulus as 0.21 GPa. The high ratio of Young's modulus to shear modulus demonstrates the anisotropy of the nanostructures and explained by longitudinal H-Bonds. Azeri *et al* investigated the extraordinary stiffness this 'soft' matter by modeling molecular interactions inside peptide nanostructure [9]. He suggests that the "zipper-like" aromatic interlocks of 6 dipeptide containing two phenyl rings each might be reason of high stability. Adding Van-der-Waals and π-π interactions he calculated a Young's modulus about 8.8 GPa which is still below the experimental result. According to the researcher the the role of water should be considered to understand the difference.

Thermal stability of is confirmed in dry samples until 150 °C and in wet samples until 121 °C [10]. In the same work, chemical stability of peptide nanotubes in different organic solvent at room temperature is investigated. SEM pictures demonstrate the geometrical stability of samples in aceton, acetonitrile, ethanole, methanol and 2-propanol. The thermal and chemical stability means a potential for future lithographic procedures.

Electronic properties of peptide self-assemblies are calculated by Akdim *et al* with a DFT modeling of well-ordered tubular nanostructures and a direct bandgap along c-axis is found [6]. The lowest energy band-gap for FF nanotubes if found to be 4.48 eV which is consistent with photoluminescence results obtained by Minjie Wang *et al* [34]. With this high band-gap FF nanotubes can be classified as wide bandgap semiconductors such as silicion carbide (2.9 eV) and ghallium nitride (3.39 eV). Furthermore Wang showed that additon or loss of water molecules resulted in a redshift or blueshift in the photoluminescence peak.

Optical properties of diphenylalanine crystal structures with smooth surfaces are examined with local illumination microscopy by Qi Li *et al* [15]. Rhodamine B was added to HFP/Water solution then coassembled with FF. When these FF microtubes are illuminated from one end, emmission at the other end is observed. There is no emmision from the body. The out-coupled light decreases exponentialy along c-axis with a atteniation length of 8µm. Handelman *et al* explained optical properties by quantum confinement in diphenylalanine self-assembly [8].

Biopiezoelectricity, a non-linear polariation phenomenon in biological matter, was found by Kholkin *et al* with a transverese coefficient $d_{15}=35$ pm/V for a microtube with 100nm diameter using piezoresponse force microscopy (PFM)[12]. This electromechanical coupling lasted for long periode of drive (tens of minutes) without any visible degradation. Researchers showed that this piezoelectricity is also reversible. The temperature dependence of this phenomenon was investigated by Bystrov *et al* [11]. The room temperature longitudinal piezoelectric coefficient is measured as $d_{33}=30$ pm/V, which exceeds $LiNbO_3$. The piezoresponse decreases towards 150 °C, which is irreversible after 100 °C. They found an irreversible phase transition from non-centrosymmetric hexagonal ($P6_1$) to orthorombic crystal structure at 150 °C. The same phase transition was observed by thermal evoluation of piezoresponse and SHG experiments [35]. After phase transition the structure is in antiferroelectric phase. The polarization cannot be switched, thus this material is unsuitable for high density data storage applications. In another work, Bystrov *et al* calculated the polarization along the c-axis using X-ray diffraction data and found the value to be 0.023 C/m^2 [16].

Second harmonic generation (SHG) in FF microtubes, an another non-linear polarization related phenomenon, and its thermal treatment were investigated by Khanra *et al* [13]. Non-linear optical coefficient; two transverse component d_{15} and d_{31} and one longitudinal d_{33} component were obtained by SHG polarimetry on individual microtubes with lengths of hundreds of micron range, inner diameters of in a few hundreds of nanometers range and outer diameter in the range 5-15 µm. The high ratio of the shear to longitudinal components, $d15 / d33$, shows the anisotropy of non linear coefficient and increases with increase tube diameter. P-polarization changes with tube diameters, whereas s-polarization remains constant for all diameters.

Uniform polarization of FF nanostructures encouraged researchers to build energy harvesters or power generators by alligning FF microtubes. Nguyen's group alligned the nanostructures and obtained an open-circuit voltage of 1.4 V, power density of 3.3 nW/cm, current of 39.2 nA by applying a force about 60N [14]. Stacking three such generators, they are able to feed enough power to a seven-segment LCD display. Another attempt was made by Lee's group to harvest piezoelectric energy, by parallel allignment of nanotubes [15]. They've found the shear piezoelectric coefficient d_{15}=46.6 pm/V. The group has managed to obtain an open-circuit voltage of 2.8 V, power density of 8.2 nW/cm, current of 37.4 nA by applying a force about 42 N, which exceed the previous attempt.

Although many researchers attempted to explained the observed properties by the crystal structure of FF NT/MT as solid state phenomena [11, 12, 13] or by quantum confinement [8] others investigated the role of water. In TGA, former structrue displayed greater thermal stability. Andrade-Filho's group investigated the water's role in the observed electronice properties [18]. They showed that dry peptide nanostructures are poor conductors. Furthermore, allignment of water molecules along the nanotube longitudinal axis gives rise to high dipole moment and hoping conductivity. The same group used a molecular dynamics simulation base on DFT to show that water keeps the stability of the structure [27]. In their work, removal of water results in a phase transition from hexagonal to orthorombic geometry. They proposed that 20-21 water molecules per hexamer is needed the structure stable. Kim *et al* showed that the rigidity of diphenylalanine crystalline nanotubes are higher than nanowires, which has one less H-Bond per motif due to loss of water [17].

3. WATER: AN ANOMALOUS LIQUID

Water is the most abundant molecule in earth and its athmosphere. Some calls water as "active matrix of life" [36], meaning that it doesn't only fill the gaps between biomolecules but it is essential for their functions. Liquid water has major role in four essential biological processes; oxidation, photosynthesis, hydrolisis and condensation [37]. On the other hand water is the key for stabilization of proteins, nucleotides, carbohydrates and lipids [38]. Therefore, understanding water's structure and properties are key to our knowledge on life. Despite being a relatively simple molecule, its structure and properties are not yet fully understood.

3.1 Structure of The Bulk Water

The water molecule is composed bonded hydrogen atoms at the vertices bonded to one oxygen atom at the center of vertice. This overall v-shaped structure is arranged with a intramoleculer OH distance of 0.957 Å and an angle of 104.52º in the gas phase, (Figure 3.1 b) [39]. This angle is similar close to internal angle of a planar pentagon 108 º and also an ideal tetrahedral angle of 109.47 º. This proximity might give rise to tetrahedral structure adopted by the condensed phase water structures. A closer inspection shows a large electronegativity difference $\Delta\chi = 1.24$ between oxygen and hydrogen atoms with partial charges of $\delta q = -0.7e$ and $\delta q = +0.35e$, respectively [40]. Classically calculated positions of electronegativity distributions are shown in Figure 1.3 a. Consequently, the dipole moment of gas phase water molecule becomes 1.84 D [41, 42]. Dipole moment of completely ionic bond would be 5.61 D, thus an OH bond can be considered as 1/3 ionic and 2/3 covalent [43]. The lone pairs and hydrogen atoms with forementioned electronegativty difference create tetrahedrally located proton acceptor and donor sites on water molecule (Figure 3.3 a). As a result, water molecules can interact with each other or molecules with electronegative surfaces through so called hydrogen bonding [44]. A typical water-water hydrogen bonding interaction energy is about 20 kJ mol^{-1} (5 kcal mol^{-1}), which is between a simple Van-der-Waals interaction about 1 kJ mol^{-1} and a covalent bond energy about 400 kJ mol^{-1} [45]. Hydrogen bond energy is approximately 10 $k_B T$ at room temperature, which

explains its liquid form at room temperature where most of other molecules of the similar molecular mass are in gaseous form.
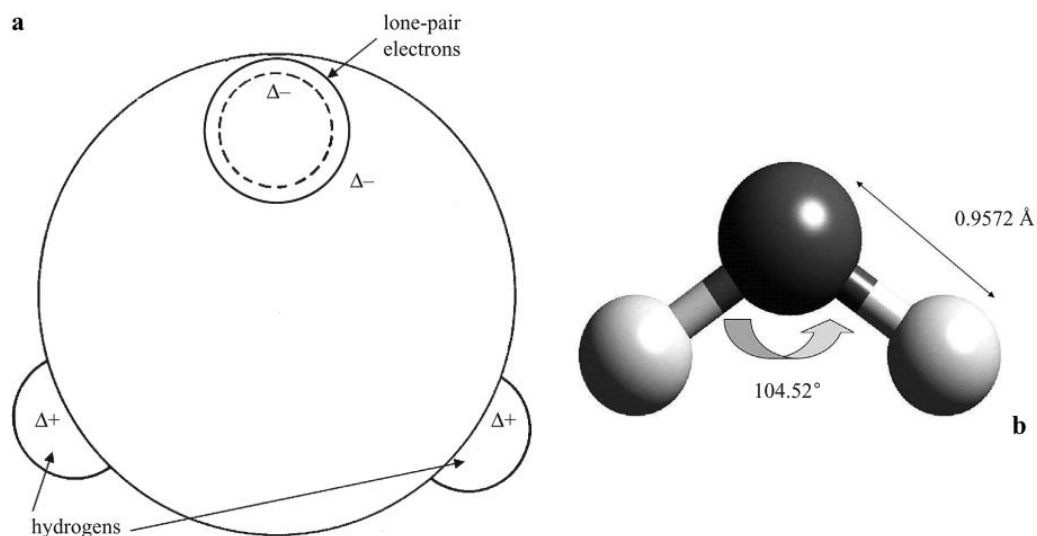
Figure 3.1: Classically calculated positions of lone pairs (Δ-) and hydrogen atoms (Δ+).The average molecular geomety of water structure (b) [45].

Bernal and Fowler described water-water hydrogen bonding rules in their seminal work in 1933 [46]. Each hydrogen atom in a water moleuce binds with oxygen of another water molecule and two lone pairs of oxygen are connected with hydrogen atoms of another two water molecules. As a result, a four-coordinated water tetrahedra with an approximate (O − O) distance 2.76 Å is constructed (Figure 3.2). This construction is further postulated that only one hydrogen atom can lie on each O-O axis forming O-H…O motif, by Pauling in 1935 [48]. Such an ice crystal is called hexagonal ice, Ih, in which the oxygen atoms are not in a close-packed arrangement, but a very wide open hydrogen bonded long-range tetrahedral network. Pauling calculated (3/2)N equally probable configurations for N water molecules, which leads to a residual entropy of 0.805 E.U which is a close approximation of the experimental value 0.87 E.U. It is remarkable that for 18 g ice, there are 1023 possible configurations. Although Pauling's analysis is a huge step in understanding water structure, it is oversimplified considering different electrostatic bond energies. Two neighboring water molecules can position themselves in oblique or inverse mirror-symmetry and oblique or inverse centre-symmtery, whose electrostatice bond energies vary [48]. Consequently, a variety of ice types with optimised lattice energies are expected and also observed in nature depending on temperature and pressure as summarised in Figure 3.3.
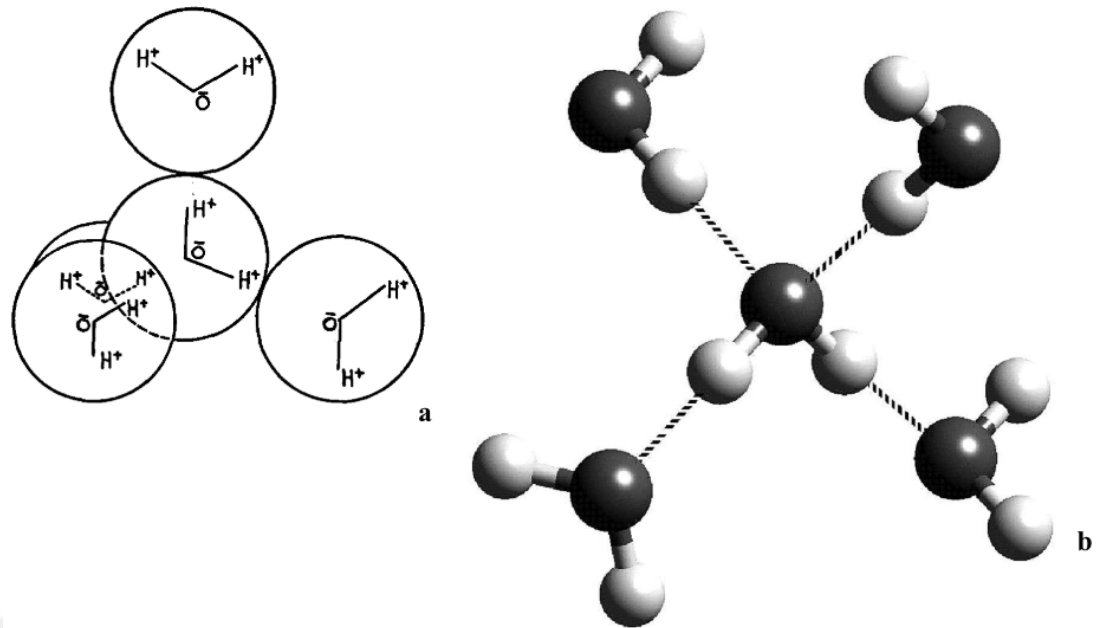
Figure 3.2: Water tetrahedra model shown by spherical volume model (a) and stick-ball model with dashed lines denoting hydrogen bonds (b) [39].

The strong directionality of hydrogen bonds causes dislocations in the Ih network. Although oxygen atoms remain in tetrahedral order, disorder of hydrogen bonds occur through propagation of dislocations. These packing faults cause infringement from Bernard-Fowler rules. Disorders in proton distribution are called Bjerrum defects [48]. There are two types of Bjerrum defects: L-defects, when no proton is located between two oxygen atoms and D-defects when two protons are located between two oxygen atoms. These faults in tetrahedral order migrates through the network, permitting dipole reorientations under external electric field. Another type of defects emerge when ionization occurs through proton jump from one water molecule to adjacent water molecule resulting an OH- and a H3O+ ion [48]. Ionisation defects remain in the system until two oppositely charged ions meet in the system.
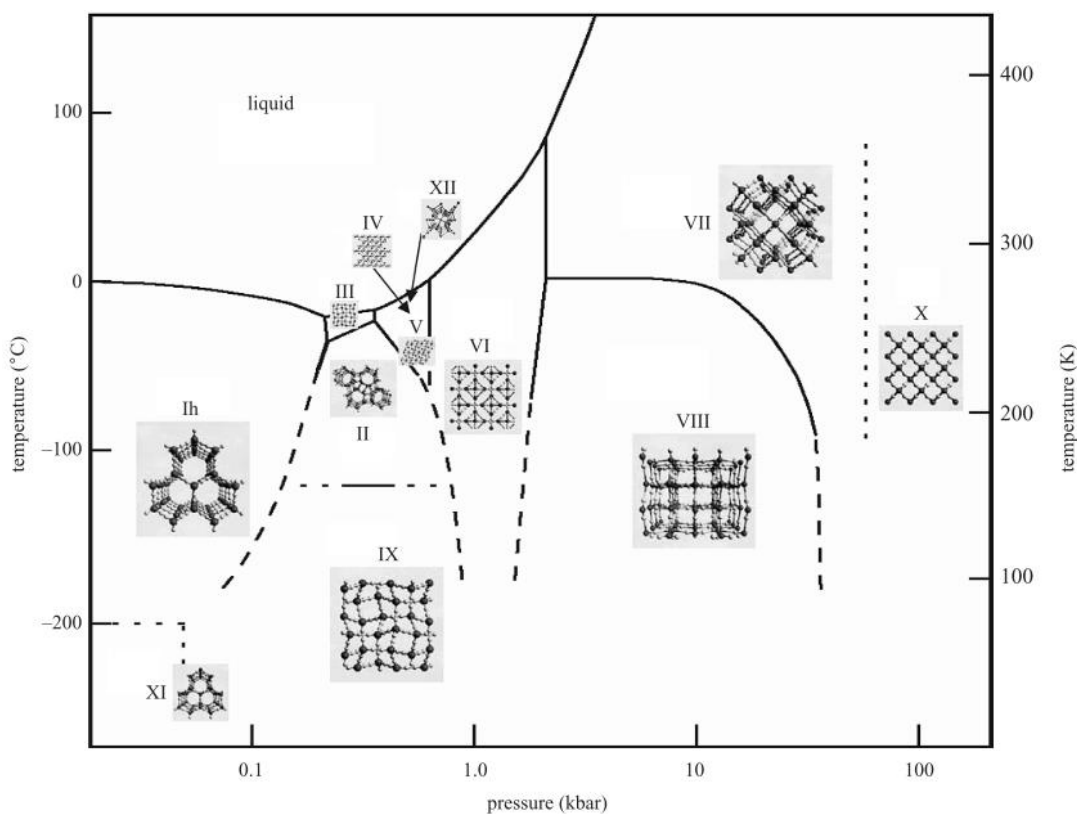
Figure 3.3: Phase diagram showing different types of ice [45].

Water has lower latent heat of fusion at athmospheric pressure, 6.01 kJ mol^{-1} with respect to the latent heat of sublimation at triple point conditions, 51 kJ mol^{-1} [49]. Consequently, the majority of hydrogen bonds are preserved upon melting, but with short-range interactions rather than crystallike long-range interactions [50]. A word of caution is needed here, that liquid water is not a crystal and the structure cannot be refered by any lattice. In the absence of lattice constraints interactions between water molecules are expected to continously diverse. Indeed, calculations have shown that first neighbour coordination of liquid water molecules range between 0 to 8 with an average of 4.4 (nearly tetrahedral) as can be seen from (Figure 3.4 b) [45]. Moreover, Sciortino *et al* proposed a bifurcated hydrogen bond, where one hydrogen atom has equal interaction energy with a sum equal to energy of a 'normal' hydrogen, consequently a hydrogen atom is bonded to two neighboring oxygen atoms [51]. Resulting molecule has local fivefold coordination, which explains relatively frequently fivefold symmetries in histogrom shown in (Figure 3.4 a). Authors have further argued that, proposed bifurcated H-bond defects in liquid water structure permits transitions between configurations. This argument might explain anomalously

14

high diffusion rates and the ability of being a good room temperature fluid with a relatively rigid H-bonded framework.
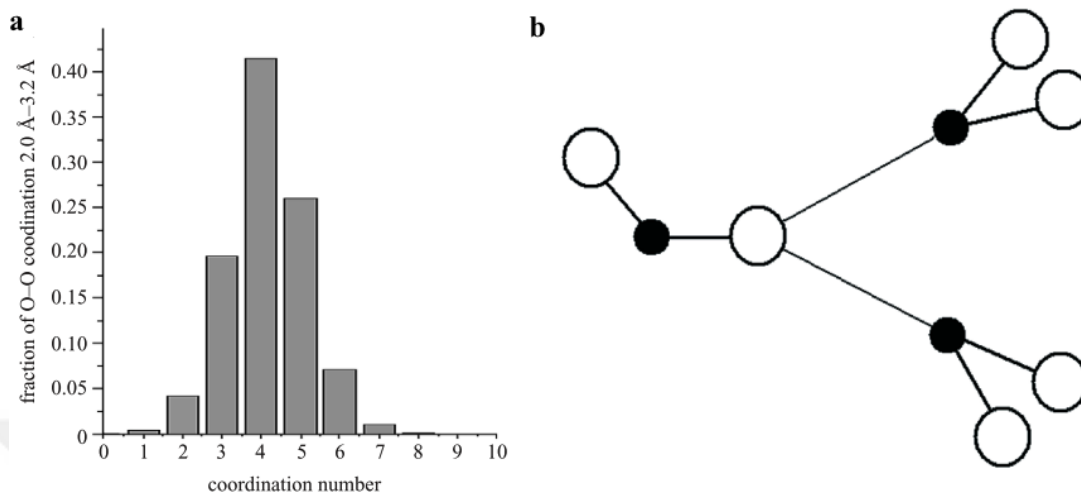
Figure 3.4: Histrogram of first-neighbour coordination numbers in liquid water (a). Bifurcated hydrogen bonds in water network resulting a fivefold coordinated region(b). Small, filled spheres denote hydrogen atoms and large, empty spheres denotes oxygen atoms [45].

3.2 Thermodynamical Anomalies of Water

Foremost anomaly of water is the fact that is in liquid state in ambient conditions, where molecules with similar mass remain mostly in gas phase. An explanation of this anomaly is given in Chapter 3.1. To summarize, strength of H-Bond network which is about 10 k_BT prevents the water molecules from the divisive effects of thermal fluctuations.
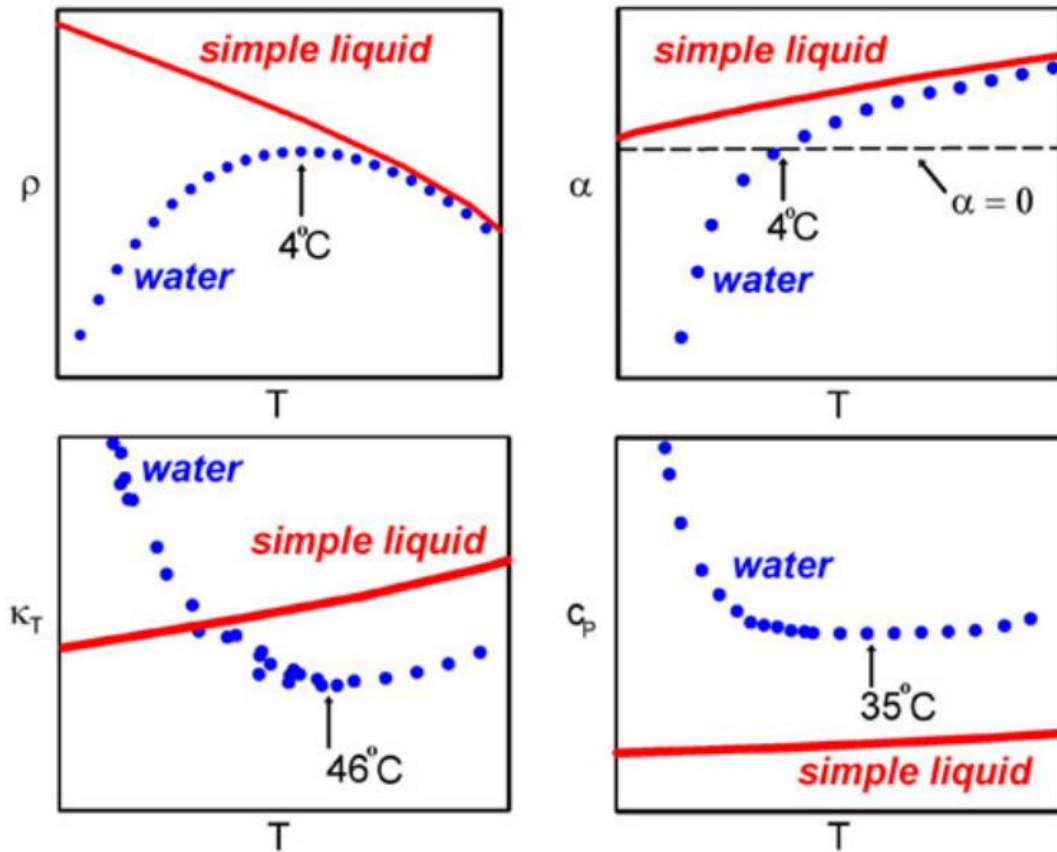
Figure 3.5: Comparison of temperature dependences of ρ-density, α thermal expansion coefficient, k_T-isothermal compressibility and c_P-isobaric heat capacity of water(blue dots) and a representative simple liquid (red line) [50].

In total there are 74 reported anomalies revealed by experiments up to date [52]. Four main thermodynamic anomalies in the vicinity of ambient conditions are shown in (Figure 3.5). Each panel corresponds to well known temperature dependences of density ρ, thermal expansion coefficient α, isothermal compressibility k_T and isobaric heat capacity c_P . The upper left figure shows the density anomaly of water when temperature decreases in the vicinity of 277 K. In high temperatures density line follows a similar trend as simple liquid with a negative slope. Upon cooling water's density bends and reaches a maximum value at 277K before evolving into a positive

slope regime in lower temeprature. Locii of the density maximum is called as Temperature of Maximum Density (TMD) in (P-T) diagram, which shifts to lower temperatures by increasing pressure). Crossing this line water behaves as a simple liquid and densifies with increasing temperature. TMD line for heavy water is shown in Figure 3.6.
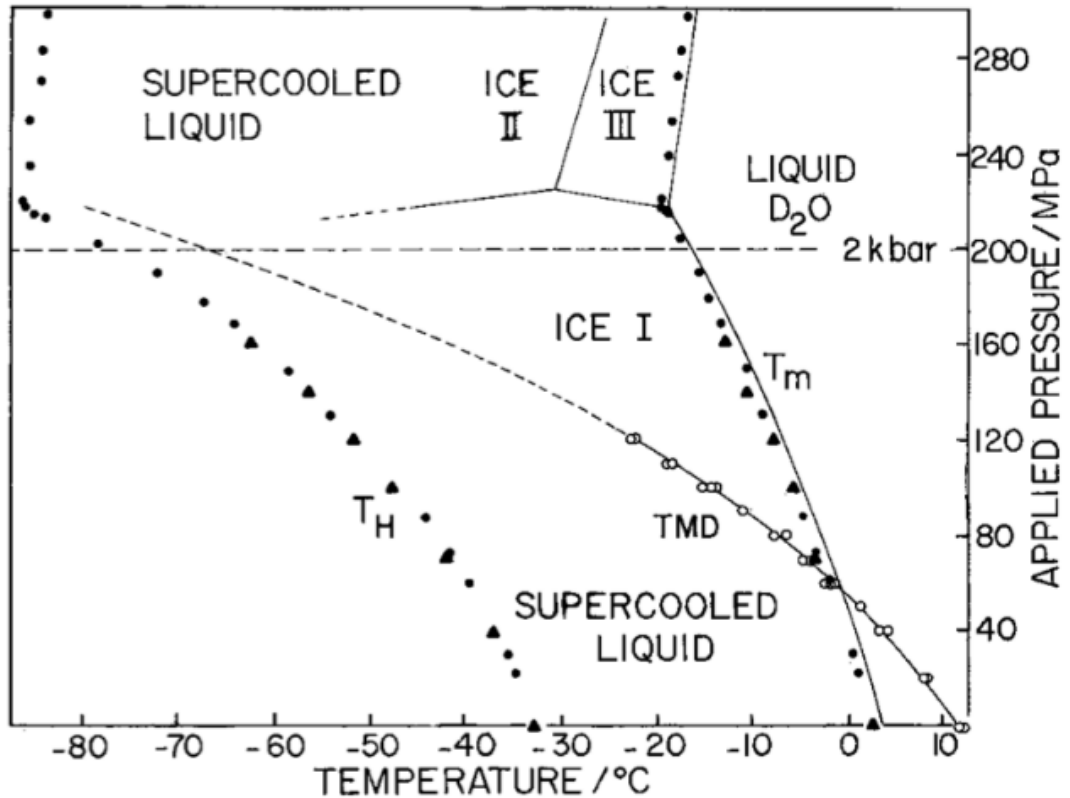
Figure 3.6: Phase diagram of heavy water' supercooled region [53] . TMD is the temperature of maximum density. T_m and T_H indicates melting temperature and homogeneous nucleation temperature respectively.

Thermodynamic response functions display anomalies in the vicinity of ambient temperature. In the upper left panel of Figure 3.5, thermal expansion coefficient α, crosses changes sign and becomes negative below 277 K, coinciding with TMD. From Figure 3.6, it is clear that anomaly α is suppressed to lower temperatures with increasing pressure. In the upper left panel, isothermal compressibility k_T, has a similar trend with simple liquids in high temperatures with a minimum at about 319 K. Upon cooling, k_T deviates from the monotonic increase of simple liquids and drastically increases below the temperature of the mentioned minimum. Furthermore, Debenedetti has shown that the occurrence of k_T minima is both related to TMD and second-order critical point of liquid-gas transition [50]. Similar to k_T, isobaric heat

17

capacity c_P exhibits a trend resembling simple liquids in high temperatures. At 308 K, c_P unpronounced minimum above which it dramatically increases to lower temperatures.

Response functions can be expressed in terms of entropy and volume fluctuatuations and correlations [54];

$$k_T = \frac{\langle (\delta V)^2 \rangle}{V k_B T} \tag{3.1}$$

$$c_P = \frac{\langle (\delta S)^2 \rangle}{N k} \tag{3.2}$$

$$\alpha = \frac{\langle \delta S \cdot \delta V \rangle}{V k_B T} \tag{3.3}$$

where k_B, T, N, S, and V denotes, Boltzmann constant, temperature, number of molecules, entropy and mean value of fluctuated volume for a fixed number of molecules, respectively. In simple liquids, volume and entropy fluctuations become smaller with decreasing temperature, whereas in water, these fluctuations become more pronounced in lower temperatures. Negative value of α indicates an anti-correlation of volume and entropy below 277 K, meaning that an increase in volume corresponds to a decrease in entropy. In simple liquids, volume and entropy are expected to be positively correlated also in lower temperatures. Anti-correlating volume and entropy in water can be explained with ordering the random tetrahedral network of liquid water. With lower thermal fluctuations, bond-angle diversity is regulated thus the orientational order parameter increases [55]. Moreover, spatial order parameter increase as a result of increased tetrahedral order. Consequently, the entropy of the system decreases whereas mean volume increases as a result of open tetrahedral network. Again tetrahedral hydrogen bonded network defines the anomalies in thermodynamic response functions. Although this network is not permanent as in ice, it offers a basis of explanation for thermodynamic anomalies of water.

Pioneering experiment of Angell and Speedly, revealed that isothermal compressiblity (Figure 3.7 a) of bulk water diverge in the vicinity of T_s = -45 ºC [56]. Isothermal compressiblity was found to obey mean-field theory with $k_T = \epsilon^\gamma$ where; $\epsilon = [(1 - T_s)/T_s]$. Authors refer this singularity to the cooperativity of tetrahedral hydrogen bond network.
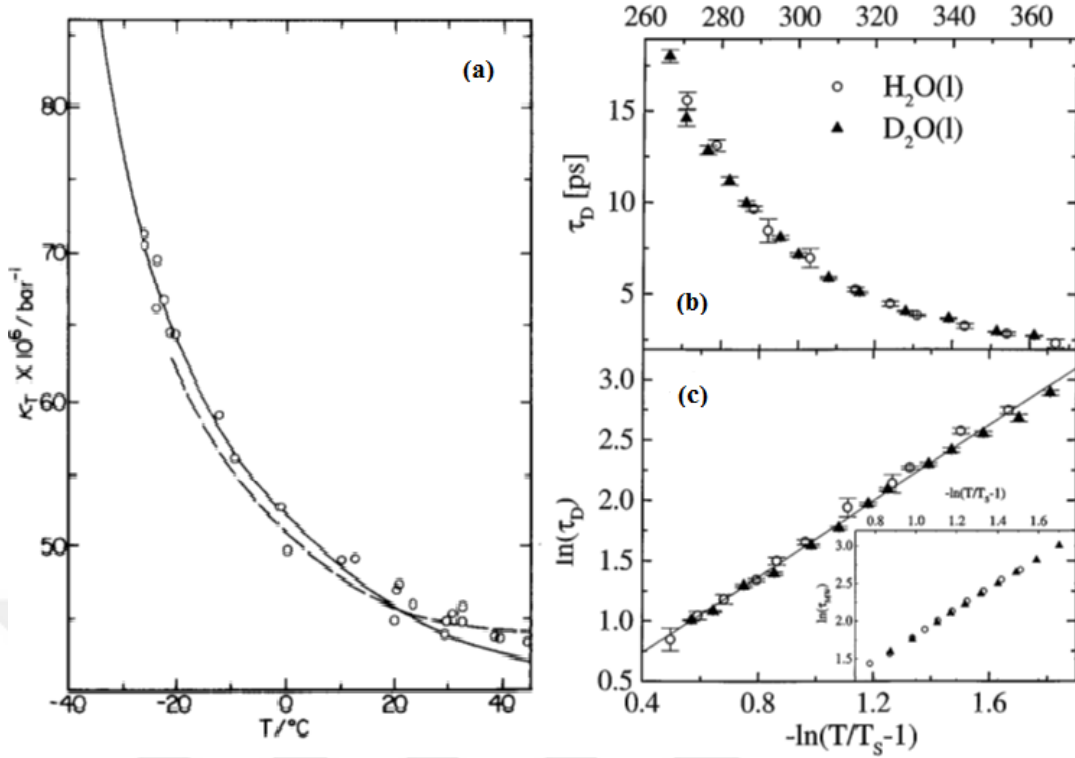
Figure 3.7: (a)Temperature dependence of isothermal compressiblity at ambient pressure [56]. (b,c) Temperature dependence of Debye relaxation time [57].

The result obtain by Angell and Speedy on the singularity of isothermal compressiblity at T_s = -45 °C was supported by Ronne *et al* in THz dielectric measurements of relaxation time (Figure 3.7 b,c) [57]. As seen from Figure 3.7 b,c, relaxation diverge with decreasing temperature. Temperature dependence of relaxation time obeys to mean-field formula where T_s was according to Angell's data.

Dynamical properties of water contain noteworthy anomalies such as in diffusion coefficient D as mean square displacement of particles. The diffusion coefficient D is related to liquid viscosity through well known Stokes-Einstein relation;

$$D = \mu k_B T \qquad (3.4)$$

with μ denoting mobility coefficient given for spherical particales as;

$$\mu = \frac{1}{6\pi\eta r} \qquad (3.5)$$

where η is the viscosity and r the radius of the particles. Principally in simple liquids obeying Stokes-Einstein law, D should decrease with decreasing temperatures. Furthermore, D is expected to decrease through compression, which hinders the

fluidity. In high temperatures, water behaves as a simple liquids, but at sufficiently low temperatures self-diffusion begins to increase with increasing temperatures [50]. Once again, an explanation of this anomaly can be given in terms of enhancement of hydrogen bond network at low temperatures. When pressure is applied on water at low temperatures, hydrogen bonds break allowing particles to gain fluidity.

The thermodynamic and dynamic anomalies discussed here are seem to persist their continuity in the supercooled region. Comprehensive experimental and theoretical work is required to understand origins of water's anomalies.

3.3 Supercooled, Metastable Phases of Liquids

Theory of metastable liquids is extensively studied by Debenedetti [58]. The physical conditions of this metastable state are defined by thermodynamic conditions and the existence of impurities or perturbations. Thermodynamics is the study of equilibrium states in indefinite lifetimes. On the other hand, when the system is trapped in minima of thermodynamic potentials in finite times, meta-equilibrium, in other words metastable state, emerges [58].

A metastable system will eventually evolve into a stable state, therefore the notion of time, namely kinetics has to be throughly examined. To be able to investigate a metastable state, its lifetime must be longer than the observation time. Furthermore, relaxation time related to structural rearrangement or establishment of equilibrium has to be much longer than the observation time, so that

$$\tau_{rel} \gg \tau_{obs} > \tau_{life} \tag{3.6}$$

If the special physical conditions are provided to system, such as extreme impurity of the sample or perfect smoothness of the container or minimised perturbation of the experimental setup, range of supercooled liquid regime can be expanded further below the freezing temperature. Eventually, two possible outcomes are expected as a result of supercooling; the sponteneous nucleation of system to stable ice state or the continuous transition into stable amorphous solid state, glass. Glass is a highly viscous material, by which extremely slow molecular motions does not permit spontenaous arrangments into equilibrium [59]. Consequently, there are two competing

characteristic time related to supercoolung phenomenon; the nucleation time required to crystallize a given volume fraction τ_1 and the structural relaxation time τ_2.

A representation of qualitative temperature dependences of τ_1 and τ_2 characteristic to a glass-forming liquid is given in Figure 3.8 [58]. The nucleation time τ_1, first decreases to a minimum and then increases with decreasing temperature. This nonmonotonic behavior of τ_1 is a combination of increasing thermodynamic driving force for nucleation and increasing viscosity [60] with decreasing temperature. Increased viscosity hinders molecular motions driving the crytalization dynamics [58]. On the other hand, structural relaxation time τ_2 is proportional to viscosity thus, it monotonically increases with increasing temperature from 10^{-12} sec to 10^2 and becomes comparable with time scale of macroscopical experiment with decreasing temperature. If the cooling is sufficiently rapid, i.e. faster than nucleation time, crystallisation is suppresed by quenching the sample down to a temperature where the molecular arrangements becomes structurally arrested. This phenomenon is called vitrification or glass transition [58]. The temperature when the relaxation time reaches to 10^2 is widely accepted as glass transition temperature, T_g.
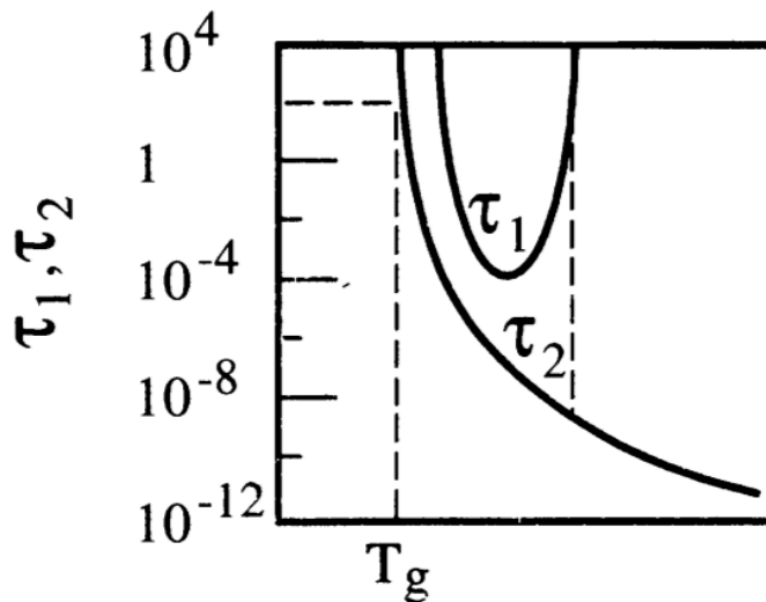
Figure 3.8:   Schematical representation of characteristic the nucleation time τ_1 and the structural relaxation time τ_2 [58]

3.4 Properties of Supercooled Water

Water is extremely poor glass-forming liquid at ambient conditions, because of its rapidly increasing nucleation rate below 273K [61]. The imagined competition between the nucleation time and the structural time for water is depicted in Figure 3.9. Bulk water can be cooled down to a limit where phase transition into hexagonal water occurs at homogeneous nucleation temperature T_H, [62]. Johari et al, hyperqenched bulk water inhibiting the nucleation of system into stable ice and observed glass transition temperature $T_G \cong 136$ K, where the liquid is structurally arrested [63, 64]. Researchers tried to enter to metastable region by thawing this vitrified state by heating from below, but their effort is failed as a result of an inevitable phase transition into cubic ice at $T_X = 150$ K [63, 64]. Consequently, an interval spanning 80 K is declared as "No-man's Land" between T_H and T_X, where experimenting is near impossible [65]. It is noteworthy, other researchers claim the temperature of glass transition to be $T_G \cong 165$ K, reflecting the difficulty of subject [66].
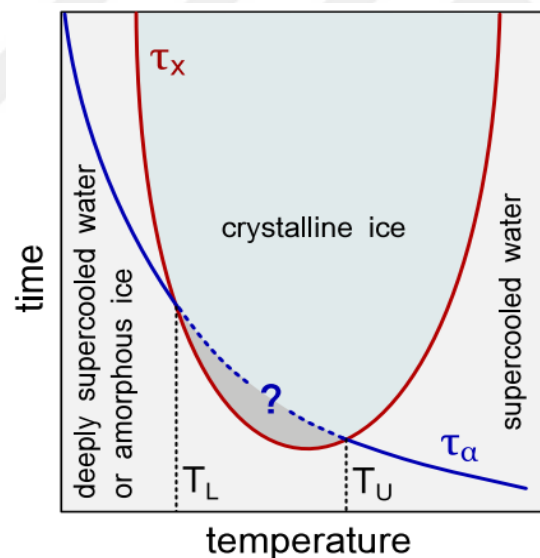
Figure 3.9: Imagined temperature dependances of the nucleation time scale τ_x and the structural relaxation τ_α of water [62]. T_U and T_L are the upper and lower temperature limits.

Nevertheless, an extensive number of experiments have been conducted to investigate the origins of water's anomalies (see Chapter 3.2) in its supercooled regime [62, 67]. In a recent study, researchers were able to probe evaporated water in supersonic down to 229 K using and ultrafast X-ray technique [68]. A large number of experiments revealed the polyamorphism of glassy water inhering a high density amorphous ice

(HDA) and a low density amorphous ice (LDA) [69, 70, 71]. Mishima et al discovered HDA by compressing I_h in low temperatures, whereas LDA is obtained by cooling below T_g in lower pressures than HDA [69]. Furthermore, a first order phase transition between LDA and HDA at about 6 kbar is revealed by the sudden change in volume and other thermodynamics properties of the system. Existence of polyamorphism in glassy water is later evidenced by neturon Diffraction [72] and Raman Spectroscopy [73].

3.5 Unifying Theories of Supercooled Water and Water's Phase Diagram

The existence of LDA-HDA phase transition together with the thermodynamical anomalies discussed in many theoretical hypothesis are proposed to inclusively explain anomalous behavior of water in its stable and metastable states. Three main scenarios are; stability-limit conjencture (retracing spinodal) [56], singularity free scenario [74] and the second critical point hypothesis [77].

The first unifying theory, stability-limit conjencture has been proposed by Speedy in 1982 [Speedy, 1982]. The theory predicts a limit of mechanical stability line (LMS) which behaves as a retracing spinodal in P-T diagram, bounding metastable supercooled and superheated states reverting to positive pressure in low temperatures. Thermodynamic response functions are expected to increse as they approach to this LMS line in P-T diagram. Debenedetti has proved thermodynamic inconsistency of this theory and there is no evidence of a LMS either experimetnally or computationaly [50].

Singularity free scenario theorised by Sastry *et al* is able to interpret both anomalies and polyamorphism of glassy water [74]. According to this scenario, increase of $k_{T,}$ c_P and decrease of α_P are direct consequence of negative slope TMD in P-T plane. Decreasings and increasing rates are sharp since the density anomaly reaches a finite maximum value. Authors used thermodynamic relations to succesfully predict trends of thermodynamic response functions. Furthermore, lattice model calculations on polyamorphism demonstrates sharper but finite increase of response functions and k_T maxime moved to lower temperatures with increasing pressure [74]. Singularity free scenario is a possible interpration of phase diagram but high resolution and refined experiments are required for further evidences.
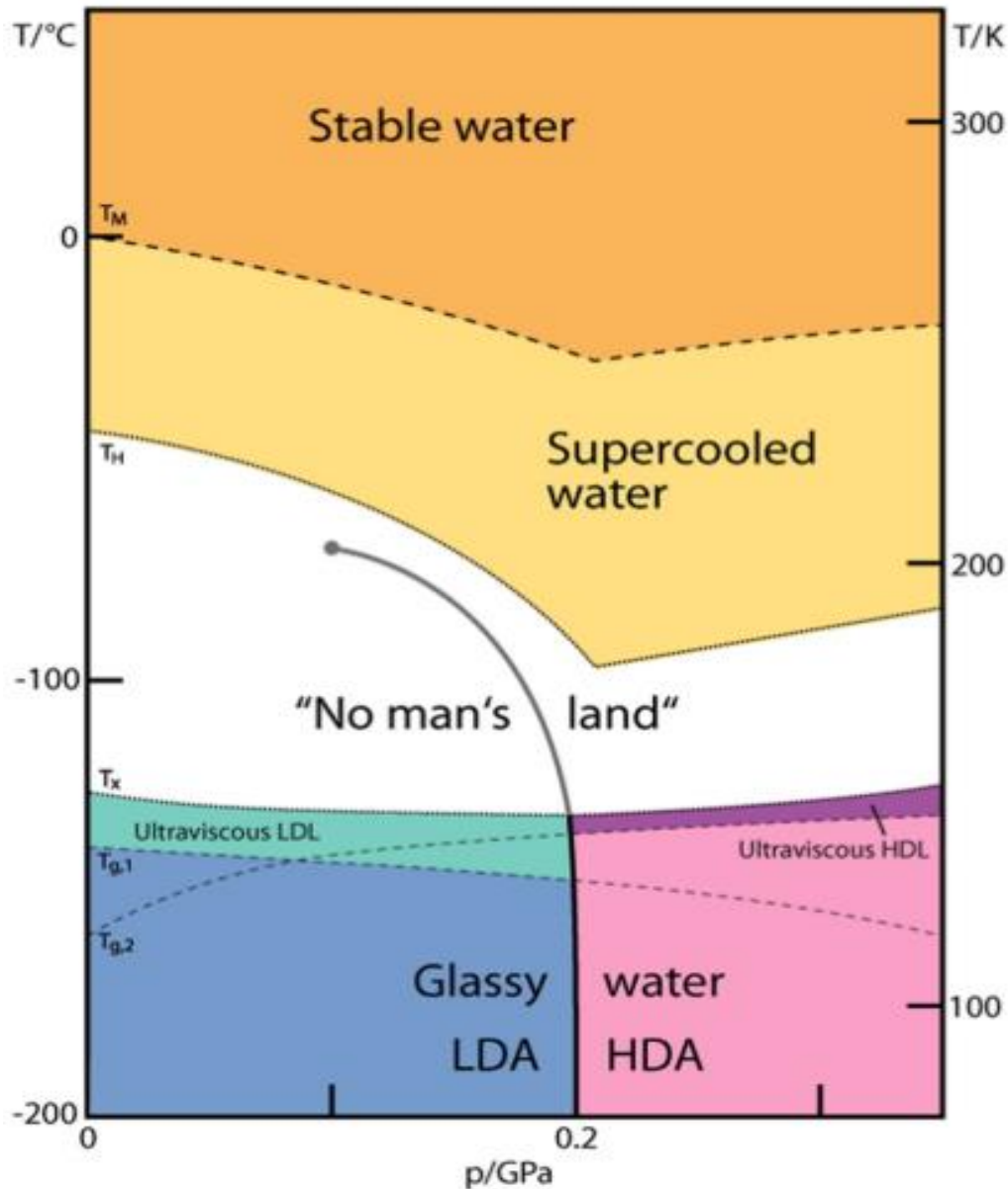
Figure 3.10: Phase diagramm of non-crystalline water. Crystalline water is only observed in "No man's land" region enclosed by homogeneous nucleation line T_H from above crystallization line T_X from below. Glass transition temperatures $T_{g,1}$ and $T_{g,2}$ seperating HDA, LDA from ultraviscous liquids HDL, LDL are taken from [75] and [76], respectively. Purported Widom Line ends at second critical point.

A last scenario, Liquid-liquid Critical Point (LLCP) hypothesis by Poole and co-workers is by far the most appreciated theoretical framework up to date [77, 50]. Their hypothesis base on phase diagram simulated by using ST2 water model. A summarising phase diagram is given in Figure 3.10. The main idea of the theory is the fact that the first order phase transition locii between HDA and LDA must, proceed to one phase region of 'no man's land' and terminate before reaching to T_H. As a consequence, thawing of the amorphous solid ices into ultraviscous high density liquid

(HDL) and low density liquid (LDL) phases is predicted. A liquid-liquid phase transition in the 'no man's land' is a natural consequence of these two distinct liquid phases present.

The presence of LLCP can acount for anomalies behaviors of thermodynamic response functions [78]. The correlation of isothermal compressiblity k_T and isobaric specific heat c_P with density and entropy fluctuations are given by equations 3.1 and 3.2. According to theory of critical phenomena, these quantities should diverge asymptotically associated with correlation lengths in the vicinity of LLCP [79]. Moreover, the first order phase transition between LDA and HDA is structurally arrested expresion of LLPT between LDL and HDL [50]. Meaning of the negative slope of LLPT locii in P-T requires an investigation to understand the nature of LDL and HDL states. Using the Clausius-Clapeyron equation;

$$\frac{dP}{dT} = \frac{\Delta s}{\Delta v} \tag{3.7}$$

where Δs and Δv denotes molar entropy and molar volume difference between two intersecting phases. Granted that the derivative in the left side has a negative value evaluated along the LLPT locii (Figure 3.11), equation 3.7 implies that HDL is more entropic and disordered in comparison with more open and structured LDL phase [77]. It should be underlined that, a correlation length maxima locii continuous into the one phase region in higher temperature and lower pressure side of LLCP. This line is called Widom Line (WL), whose schematical description in P-T Plane is depicted in Figure 3.10. Thermodynamic responses related to liquid fluctuations are expected to diverge asympotitaly upon crossing the WL [80, 81]. A similar line is observed in above liquid-vapor critical point [82].
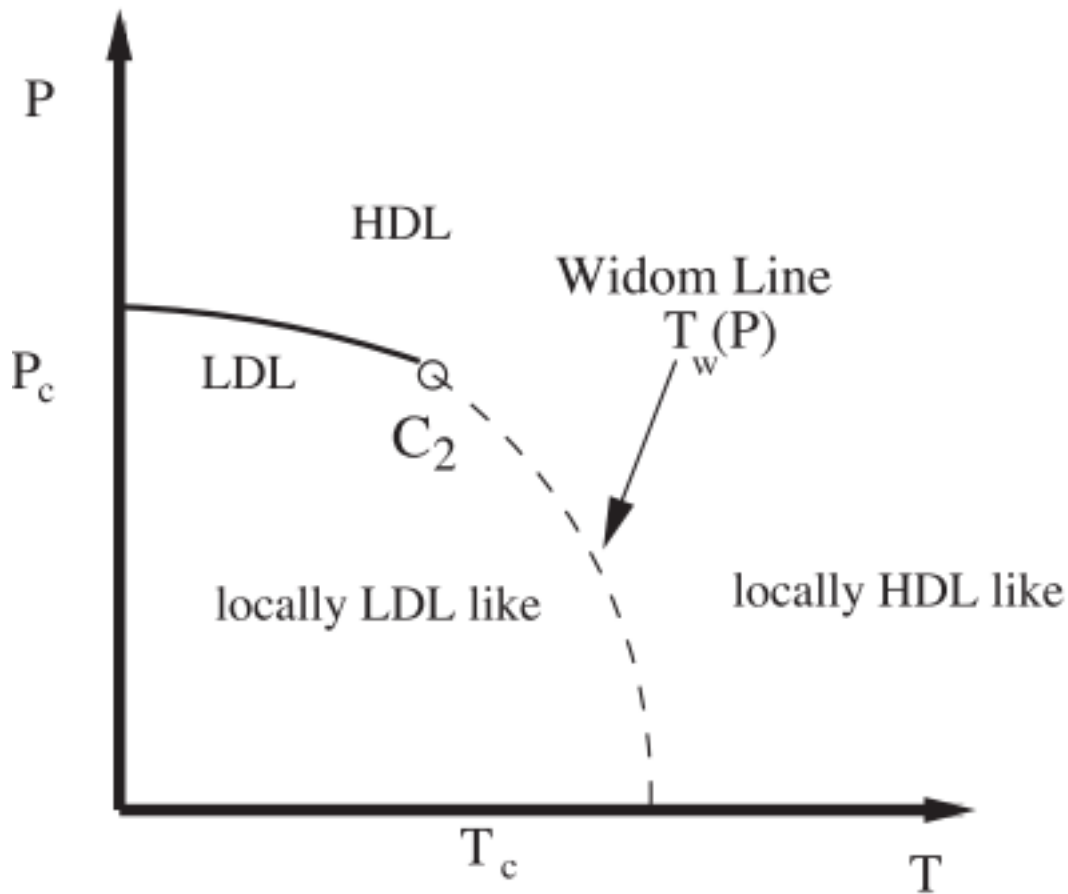
Figure 3.11: Schematical Representation of LLPT, second critical point C_2 and Widom Line T_W on the P-T plane [83]. In lower temperature and lower pressure side of the Widom Line, water behaves locally LDL like and locally HDL, otherwise.

A decisive experimental evidence of LLCP does not exist, since it is yet impossible to experimentally explore "no man's land" of bulk water. Mishima and Stanley, conducted a pioneering experiment following the line of metastable ice IV [65]. Eventually, they intrepreted the sharp variation around T = 220 K and P = 100 MPa as the second critical point. Due to the fact that, this observation can also be accounted by singularity free scenario, this work is a fundamental but not definitive proof of second critical point hypothesis.

3.6 Fragile to Strong Transition

Fragility can be defined as the rate of structural change metric meaning that on cooling, the viscosity of a fragile liquid reaches the infinity rapidly when it is plotted against T/T_g, where T_g is the glass transition [84]. We know that using equation 3.8 viscosity

η is inversely proportional to D. Diffusion of a fragile liquid can be modelled by Vogel-Fulcher-Tamman equation;

$$D = D_0 exp\left(-\frac{B}{T-T_0}\right) \tag{3.8}$$

with D_0 denotes the diffusion at infinite temperature and B=D/T_0, where T_0 is known as Kauzmann temperature where the viscosity value diverges and D is the strength parameter [13].There is another class of liquids based on their viscosity, called strong liquids. In this case D is modelled according to Arrhenius equation;

$$D = D_0 exp\left(-\frac{E_a}{k_B T}\right) \tag{3.9}$$

where E_a is the activation energy. In strong liquids dynamical properties of system is dominated by activated processes. An example plot of shear viscosity η vs T/T_g is given in Figure 3.12.

Ito *et al* argues that water is a fragile liquid in ambient conditions and using Kauzman's argument, for normal cooling rates one would expect that T_g of water to be located between 200 K and 220 K [84]. Nevertheless, the fact that earlier works done by Johari and co-workers defines the glass transition as $T_g{\sim}136$ K, strongly suggests that as a result of a dynamical crossover water becomes a strong liquid in low temperatures. Therefore, a fragile-to-strong crossover (FSC) is proposed in 'no man's land'.

Computational simulations based on different water models confirmed the presence of FST [85, 86]. Furthermore a relation between LLCP and FSC is confirmed by closely laying positions in P-T plane, obtained by computational model [67]. An experimental evidence of FSC for bulk water up to date is not possible due to spontaneous nucleation.
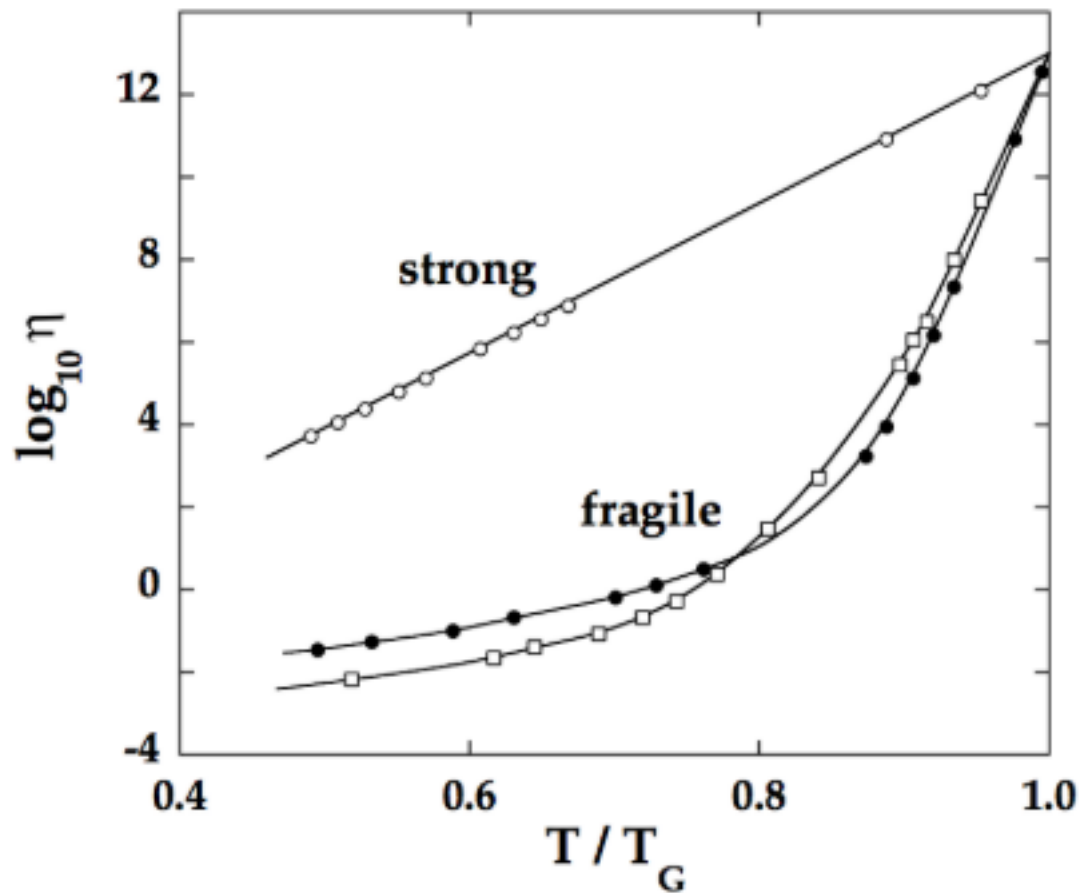
Figure 3.12: Arrhenius plot of of shear viscosities of typical glass-forming liquids [87]. Open circles and squares are silica and o-terphenyl, in order. Filled circles belong to an ionic melt of composition [KNO3]0.6[Ca(NO)3]2]0.4.

3.7 Supercooled Water in Confined Geometries

Restricting the size of the water domains by geometrical confinement makes it possible for researchers to enter 'no man's land' avoiding the crystalisation when liquid water is cooled from room temperature or when amorphous solid water is heated from lower temperatures [88, 20, 89]. Although a decisive evidence is not available, it is widely excepted that results obtained from confined water in low temperatures can be compared with supercooled water [90]. Bypassing crystallisation in confined geometries depends on many parameters, but water molecules intercalated in MCM-41cylindrical pores does not form ice if the pore diameter is 20 Å or less [91, 92]. There have been many nanoporous materials used both as hard [91, 93, 94 , 95, 96] and soft [97, 84] confinement. Here, hard or soft defines porous rigid materials or dense solutions, respectively. In this chapter, I will focus mostly on water confined in MCM-41 silica subtrates with hydrophilic cylindrical pores of a few nanometer diameters [90], since they are the most appropriate material to FF NT/MT.
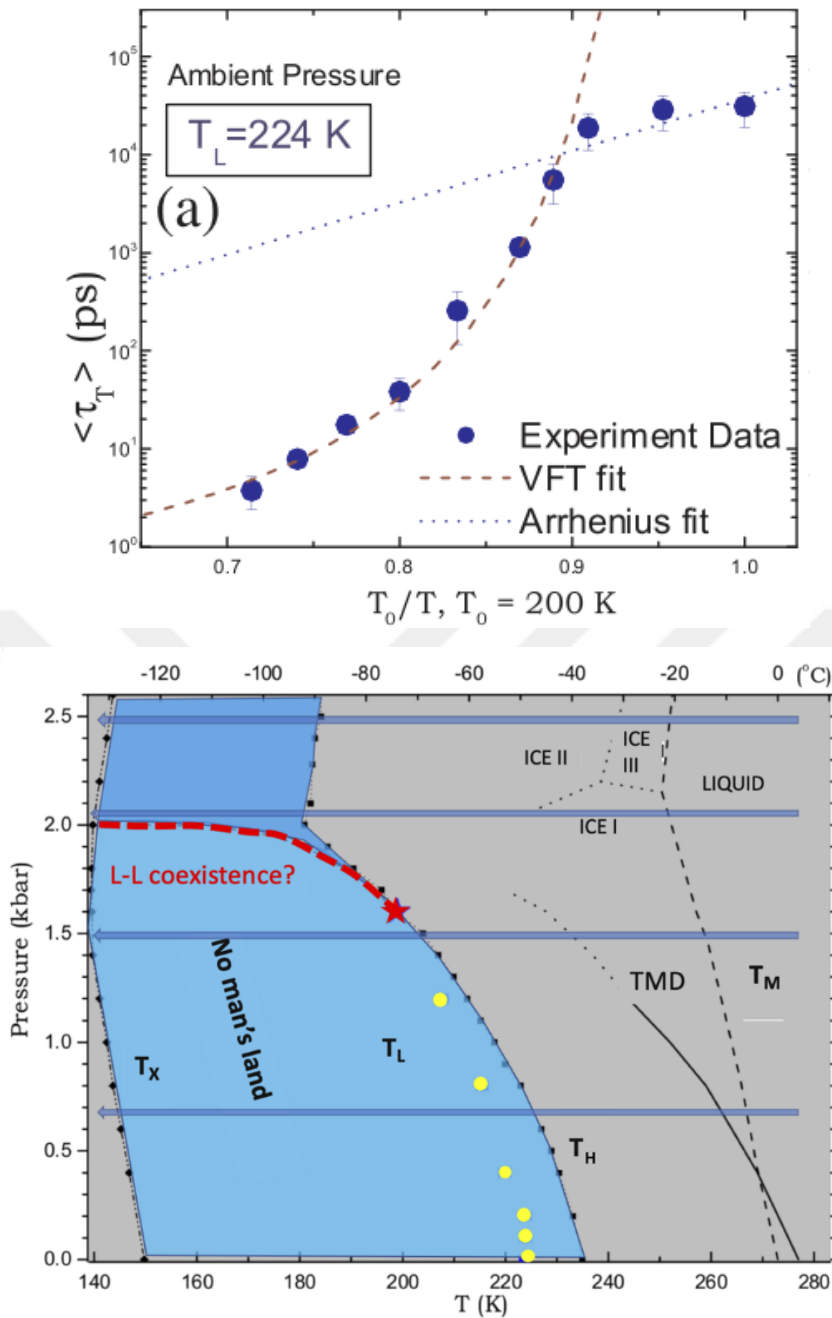
Figure 3.13: (a) Temperature dependence of translational relaxation time $<\tau_L>$ [98]. (b) The phase diagram of water in supercooled region [100]. TMD is the temperature of maximum density. T_M, T_H and T_X indicates melting temperature, homogeneous nucleation temperature and crystalization temperature of amorphous solid water, respectively. Blue region between T_H and T_X lines is 'No man's land', with light blue; LDL and dark blue; HDL. Dashed red line denotes the LLPT locii between LDL and HDL ends at red star resembling the purported second critical point. Yellow dots are the FSC positions on P-T plane found by Liu *et al* [98]

Liu and co-workers, were managed to avoid crystallisation of water inside MCM-41-S (14 Å) and using high resolution QENS revelad a cusplike crossover from VFT behavior to Arrhenius behavior, so called fragile-to-strong transition at $T_L = 224$ K at

ambient pressure [98] (Figure 3.13 a). Furthermore, researchers claimed that they obtained the termination of FSC locii at 200 K and 1600 kbar second critical point, which can be seen from Figure 3.13 b. A similar result, $T_{FSC} = 225$ K was obtained by Chen *et al* using NMR technique in addition to QENS [89]. Accordingly, they've compared rotational and translational dynamics pointing the same crossover in that temperature. Additionaly, they've argued a violation of Stokes-Einstein relation (SER) in diffusivity. Subsequently, Kumar has obtained the latter result and argued that heterogenities in the confined water's structure are the cause of SER breakdown [83]. The author argued that HDL is less dynamical heterogeneous than LDL which explains further violation of SER after below a crossover at about 225 K, assigned as FSC temperature. Similar results were obtained in favor of the FST, consequently of LLCP hypothesis [94, 88].

Recently, Stefanutti and co-workers tested Liu's prediction by employing FTIR spectroscopy for water confined in same MCM-41-S porous silica on isobaric lines, long-blue arrows in Figure 3.13 b [100]. Suprisingly, authors encountered distinctive vibrational bands related to ice phase of water in FIR region. At ambient pressure they've observed a combination of ice and supercooled water between 243 K and 253 K, which becomes fully crystalline ice on further cooling. Authors concluded that a single experimental method with narrow range is not enough to understand properties of confined water, since water's responses dispersed in a broad experimental range and time scales. In a recent review paper, Cerveny *et al* stated that a FSC can be observed down to 180 K when cooperative aranged regions reaches the confinement size in BDS measurements [90]. In lower temperature region dynamics is a universal β-relaxation with activation energy $E_A = 0.5 \pm 0.03$ eV. In the same review paper, authors argued that water in the pore inners solidifies at about 225 K, wheras interfacial water remains liquid and experiences glass transition at about 180 K[90].

Regarding the glass transition, there are deviating values in the literature. Swenson argued that incompleted tetrahedral bonds must speed up the dynamics and for that matter T_g must be in higher temperatures than 136 K [91]. Using positron annihilation lifetime spectroscopy (PLAS) Roussenova and co-workers determined the glass transition as $T_g = 190 \pm 2$ K [101], where $\alpha\beta$-crossover comes to happen.

Vibrational spectroscopy of nanoconfined/supercooled water reveals an increase on the low frequency side of the OH-Stretching region, which is attributed to LDL with

k ~ 3100 cm^{-1} by Mallamace *et al* [97]. A similar band was also found in lysozime-water system [102]. An alternatif explanation of this band would be the increasing coupling of water with the environment through extensive hydrogen bonded network. It is known that hydrogen bond number decreases OH-stretching band's frequncy [103]. Skinner calculated infrared band shapes under strong coupling, meaning hydrogen bonds with an acceptor group, and obtained a band shape with increased intensity in lower frequency with a splitting from 3260 cm^{-1} [104], which is shown in Figure 3.14.
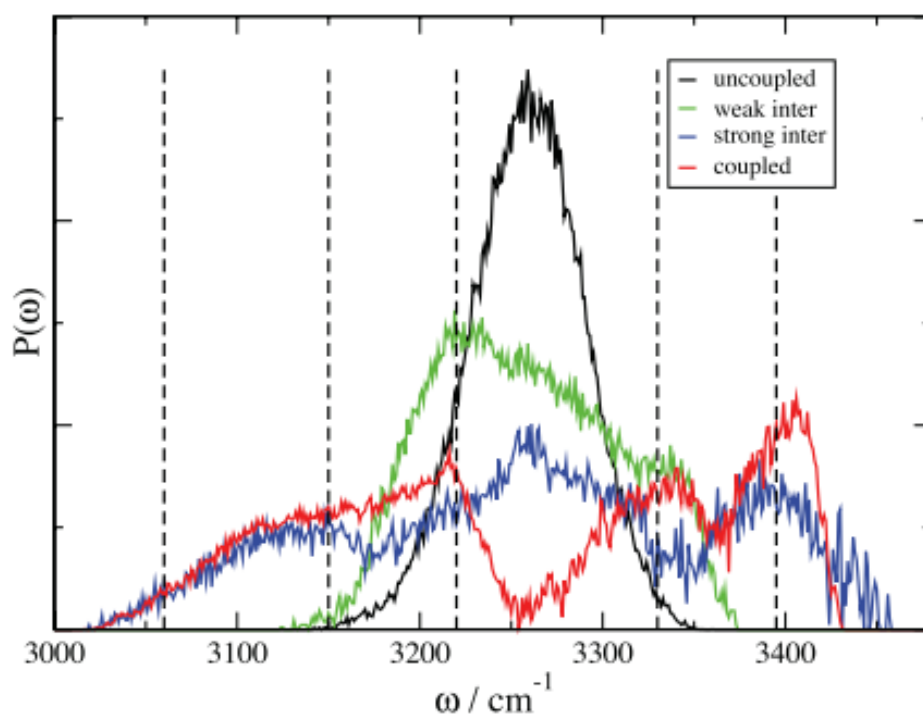
Figure 3.14: OH-stretching absorption probability densies calculated for water molecules [104].

4. BROADBAND DIELECTRIC SPECTROSCOPY OF FF NT/MT

4.1 Sample Preparation

As explained in Chapter 2.2, standard procedure from the literature [30, 5] is endorsed for the sample preparation.

Main approach in sample preparation in our experiments is to keep native state of FF NT/MT. To achieve this samples were prepared on the stainless steel electrodes and isolated from environment. The idea is to keep the states of resident water intact. From discussions in the introduction hygroscopicity of the FF NT/MT is obvious.

The FF building blocks in lyophilized form were dissolved in 1,1,1,3,3,3-hexafluoro-2-propanol with a ratio of 100 mg mL^{-1}. Then the the solution is hydrated in ddH_2O to trigger nanotube self-assembly process in room temperature. The evaporation of HFP and water took place in room temperature and athmospheric conditions.

The obtained microtubes with well-developed crystal surfaces are uniformly distributed on the elelctrode (Figure 4.1). Microtubes have central tubular channel with diameter approximately 0.1 µm[32]. This empty space does not pertmit to measure the exact value of dielectric constant. Sample thickness is about 10 µm.
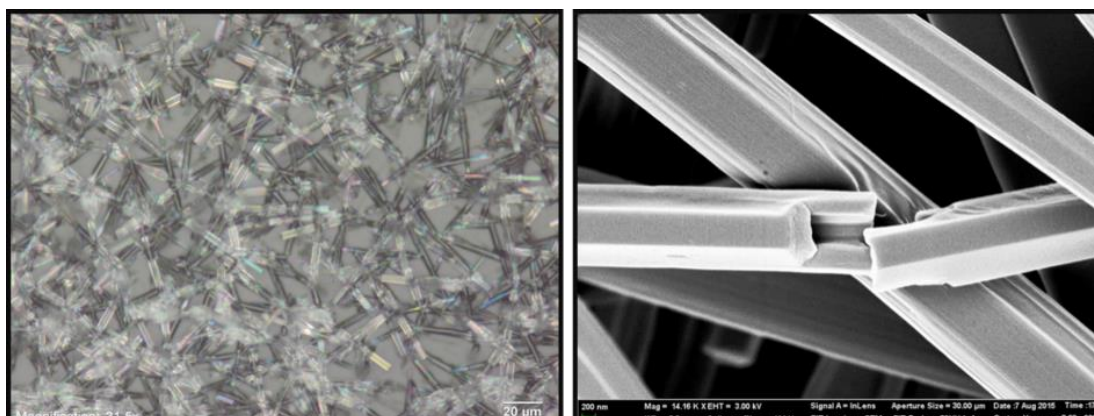
Figure 4.1 : Left side; optical microscopy of prepared samples, right side; SEM image of peptide microtubes. Well defined hexagonal structure and hollow microtubes are easily seen.

4.2 Theory of Dielectric Spectroscopy

Like many other spectroscopy methods, broadband dielectric spectroscopy is based on linear response model, where the input is electric field and the response is polarisation. Schönhals and Kremmer has a clear explanation of dielectric relaxation [105].

A small external field E(t) applied on a dielectric material will respond with a polarisation P(t) in the same direction:

$$\vec{D} = \varepsilon^* \varepsilon_0 \vec{E} \tag{4.1}$$

$\vec{D}$ is called dielectric displacement and it will cause the polarization in dielectric material with time dependent complex dielectric function ε^*, where ε_0 is the permittivity of vacuum:

$$\vec{P} = \vec{D} - \vec{D}_0 = (\varepsilon^* - 1)\varepsilon_0 \vec{D} \tag{4.2}$$

Let's think about a step function as a simple example. In this case change in applied electrical field $\Delta\vec{E}$ will be constant in time. This is the basic of DC Voltage. Thus;

$$\varepsilon(t) = \frac{P(t) - P_\infty}{\Delta E} \tag{4.3}$$

where P_∞ is the instantenous response.

In general, using linear response theory any arbitrary time-dependent applied electrical field $\vec{E}$ induce a polarisation equal to;

$$P(t) = P_\infty + \varepsilon_0 \int_{-\infty}^{t} \varepsilon(t - t') \frac{dE(t')}{dt'} dt' \tag{4.4}$$

Bearing in mind that the dielectric permittivity is a complex number, a time periodic applied electrical field for example a sinusoidal will result in a sinusoidal polarisation;

$$P(t) = P_0 sin(\omega t + \delta) \tag{4.5}$$

δ is the phase shift between applied electrical field and polarisation and ω is the angular frequency.

At last we arrived to a function which can be divided into real and imaginary parts;

$$\varepsilon^* = \varepsilon'(\omega) - i\varepsilon''(\omega) \tag{4.6}$$

Here the real part ε' is related to the energy stored during one cycle and ε'' is related to the dissipated energy per turn. Conversation of energy dictates a relationship between real and imaginary parts of the complex dielectric constant. These are called Kramers-Kronig relationships;

$$\varepsilon'(\omega) - \varepsilon_\infty = \frac{1}{\pi} \oint \frac{\varepsilon''(\xi)}{\xi - \omega} d\xi \tag{4.7}$$

$$\varepsilon''(\omega) = \frac{1}{\pi} \oint \frac{\varepsilon'(\xi) - \varepsilon_\infty}{\xi - \omega} d\xi \tag{4.8}$$

So an equipment capable of generating and then measuring responding AC Voltage between two electrode filled with a dielectric material with a computer can measure the real and imaginary parts of complex permittivity.

An idealised dielectric relaxation response for non-interacting group of dipoles in an alternating electrical field can be modelled by Debye mode [106];

$$\varepsilon^* = \varepsilon_\infty + \frac{\Delta\varepsilon}{1 - i\omega\tau} \tag{4.9}$$

where ε^* is the complex permittivity, τ is the characteristic relaxation time of the system and ω is the driving frequency of the external electrical field. Dielectric strength is given by $\Delta\varepsilon = \varepsilon_s - \varepsilon_\infty$, with ε_s gives the static permittivity and ε_∞ is the permittivity at high frequency limit.

There are some empirical models built over Debye model to analyze the obtained spectrum. The most general model is called Havriliak/Negami function [107];

$$\varepsilon^*_{HN} = \varepsilon_\infty + \frac{\Delta\varepsilon}{(1 + (i\omega\tau_{HN})^a)^b} \tag{4.10}$$

where $\Delta\varepsilon$ is the relaxation strength of succesive relaxation processes in the frequency domain, τ_{HN} is the relaxation time and a, b parameters account for the symmetric and assymetric broadening of $\varepsilon''(\omega)$ peak.

Characteristic relaxation times exhibit different temperature dependences, depending on the nature of the processes. First and most simple behaviour is modelled with Arrhenius equation [108];

$$\tau_A = \tau_0 \exp\left(\frac{E_A}{k_B T}\right) \tag{4.11}$$

where E_A is the activation energy, k_B is the Boltzmann constant and τ_0 is the high temperature attempt time. Arrhenius equation is successfully related to local relaxation phenomena, when long range interactions are absent.

Cooperativity arises when the interconnected relaxation processes occur in the system. Thermal evolution of structural relaxation processes are cooperative and obey the Vogel-Fulcher-Tamman (VFT) relation [109, 110] as stated;

$$\tau_\alpha = \tau_0 \exp\left(\frac{D T_{VFT}}{T - T_{VFT}}\right) \tag{4.12}$$

with D denoting the strength parameter and T_{VFT} is the temperature at which the configurational entropy is saturated.

For non-monotonic, saddle-like temperature dependences of relaxation times we use the following formula suggested by Ryabov and co-workers [111, 112];

$$\tau = \tau_0 \exp\left[\frac{E_A}{k_B T} + C exp(-\frac{E_d}{k_B T})\right] \tag{4.13}$$

where E_A is the energy barrier between neighbouring states similar to the activation energy in Arrhenius function, $\eta = 1/C$ is the defect concentration and E_d is the defect formation energy.

4.3 Experimental Setup

The temperature dependece of dielectric permittivity is conducted using HP 4192A Impedence analyzer with handmade cryostat using liquid nitrogen as cooling agent. Dielectric loss spectroscopy is conducted with Novocontrol Concept 80, equiped with Alpha-A Analyzer for dielectric measurements between 10^{-2} Hz -10^7 Hz (Figure 4.2). Sample is placed between two electrodes in parallel. Temperature is measured with PT100 directly from the lower electrode in contact with the sample (Figure 4.2b). The accuracy of the system is 1fF (113).
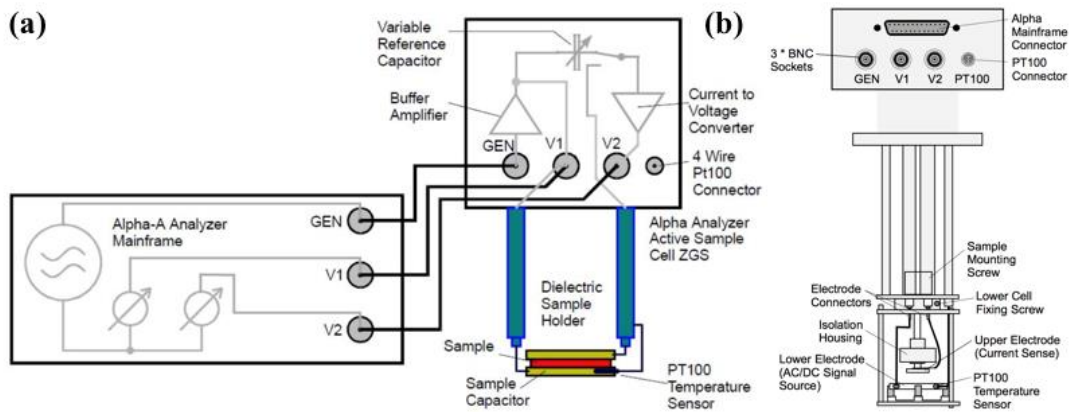
Figure 4.2 : (a) Schematical Description of Alpha-A Analyzer setup and (b) dielectric sample holder [113].

High frequency measurements are conducted using Agilent 4991A RF Analyzer for dielectric measurements between 1MHz – 3GHz. In this frequency range, a coaxial sample holder is used for better precision (Figure 4.3). Callibrations are made before each measurement to ensure no background contribitons are added because of the coaxial line. RF Analyzer has an basic impedance accuracy of +/-0.8% [113].
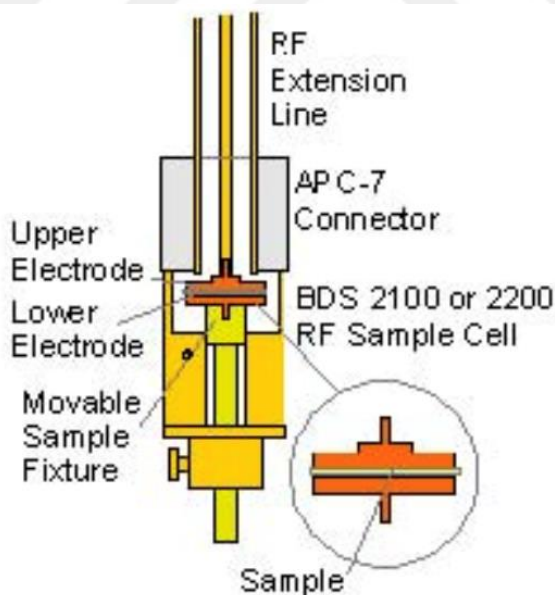
Figure 4.3 : Coaxial sample holder used in RF measuremente [113].

Quatro cooling system is purchased from Novocontrol is a nitrogen jet cooling system with a stability ±0.3 °C between 120 K and 450 K.

4.4 Fitting Procedure

Relaxation and dielectric parameters were obtained by the fitting of formula 2.10 using WINFIT program provided by NOVOCONTROL. Spectra at each temperature is fitted by maximum three relaxation processes and the parameters are transfered to the next temperature to obtain a continuous fitting procedure.

Once the relaxation times are obtained as Havriliak-Negami parameters, temperature dependences of relaxation times are fitted using one models in equations 4.11, 4.12 and 4.13. Goodness of fitting is ensured by the low RMS values seen in the Table A.1 in Appendix A. Fitting procedure of relaxation times are performed on home built Levenberg-Marquardt procedure on MATLAB$^{®}$. Fitting parameters obtained through this procedure is given in Table 4.1 and Table 4.2. R^2 values are close to unity which guarantees the goodness of the fit.

4.5 Results and Discussions

4.5.1   Temperature dependence of dielectric permittivity of FF NT/MT

Due to microtubular cavities dielectric constant shouldn't be understood as real value, but the effective dielectric contsant measured across random orientations of FF NT/MT with hay stacking between electrodes as seen from Figure 4.4.

Temperature evolution of $\varepsilon(\omega,T)$ demonstrates anomalies at 170K, , 195K and 230K (Figure 4.4). There is a dispersion onset between 130 K and 140 K, which coincides with T_g=136 K of glassy water[114]. This temperature is similar with many other supercooled system in different confinements [115]. The anomaly shown in the inset around 420K is related to the loss of water molecules from the peptide nanotubes causing the observed irreversible transition by other authors [35].
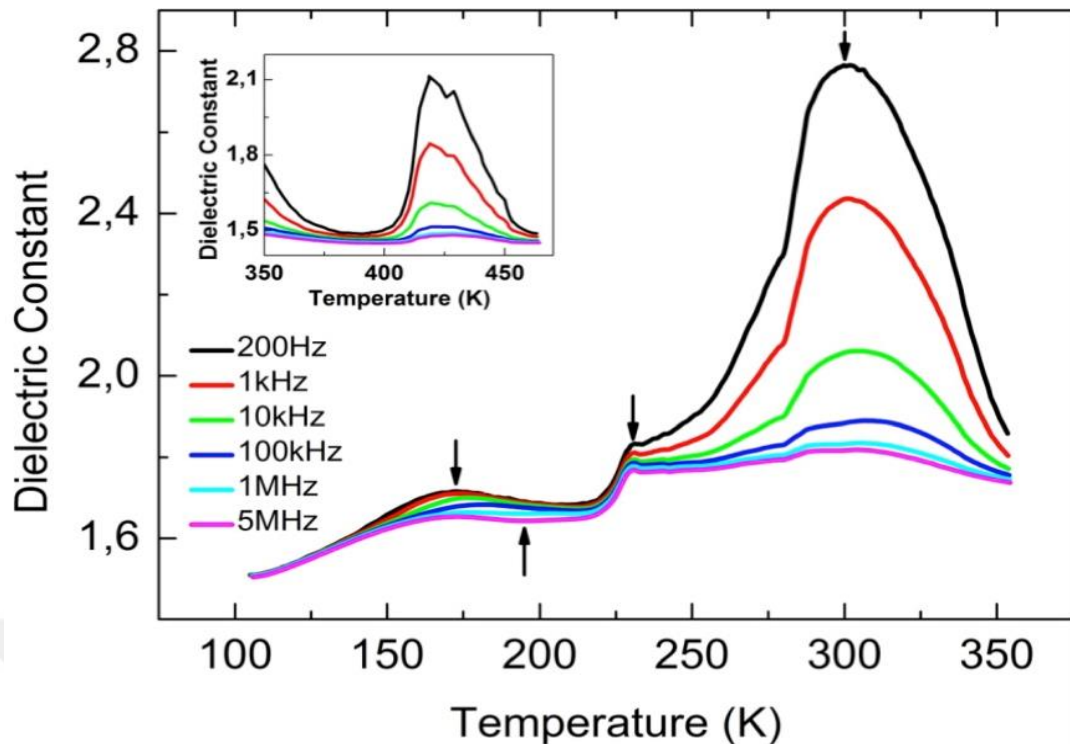
Figure 4.4 : Dielectric constant versus temperature at several frequencies. The inset presents the irreversible transition around T= 420K. Black arrows indicate the dielectric anomalies.

To understand dynamics in 170K and 195K, a closer look is needed (Figure 4.5). Somehow complicated relaxation dynamics in this region is a sign of different dipole contributions inside peptide nanotube. $\varepsilon'(\omega,T)$ peak at 195 K is a conventional dynamic showing the softening of frozen substance as a result of warming up. Dielectric peak moves to higher frequencies as the substance is softened with increasing temperatures. Relaxation of dielectric peak in the region of 170 K up to 300 kHz has similar nature. On the other hand, dielectric peak between 300 kHz-8MHz is shifting to higher temperature with decreasing frequencies, which can be attributed to growing of dipole moment of water clusters due to ordering of H-Bonds. Increasing of the dielectric constant is limited by 300 kHz probably due to finite size effect in FF nanocavity confinement. This observation indicates a dipole heterogenity of water molecules confined in different locations in FF nanocavity.

Briefly, in this temperature range 160K – 195K, hydrogen bonded network between two groups of water is built and dipolar order sets in. At 170 K weakly bounded water molecules to hydrophilic groups in nanochannel take their part in relaxation process, then the relaxation of tightly bonded water groups around 195 K is triggered. Consequently, tetrahedral network is built between water clusters in different

confinement distributed in the self-assembled diphenylalanine nanostructures. Regarding the maximum 1nm diameter of confining regions, hydrogen bonds following Bernal-Pauling-Fowler rule should be expanding along the c-axis of nanotubes. A phase transition about 200 K has been detected using Raman spectroscopy[116]. The authors interpreted this phenomenon as an indication of fragile-to-strong transition exhibited by the phonon relaxation rates related to water vibrations. We have strong evidence to belive otherwise as will be explained later chapters.
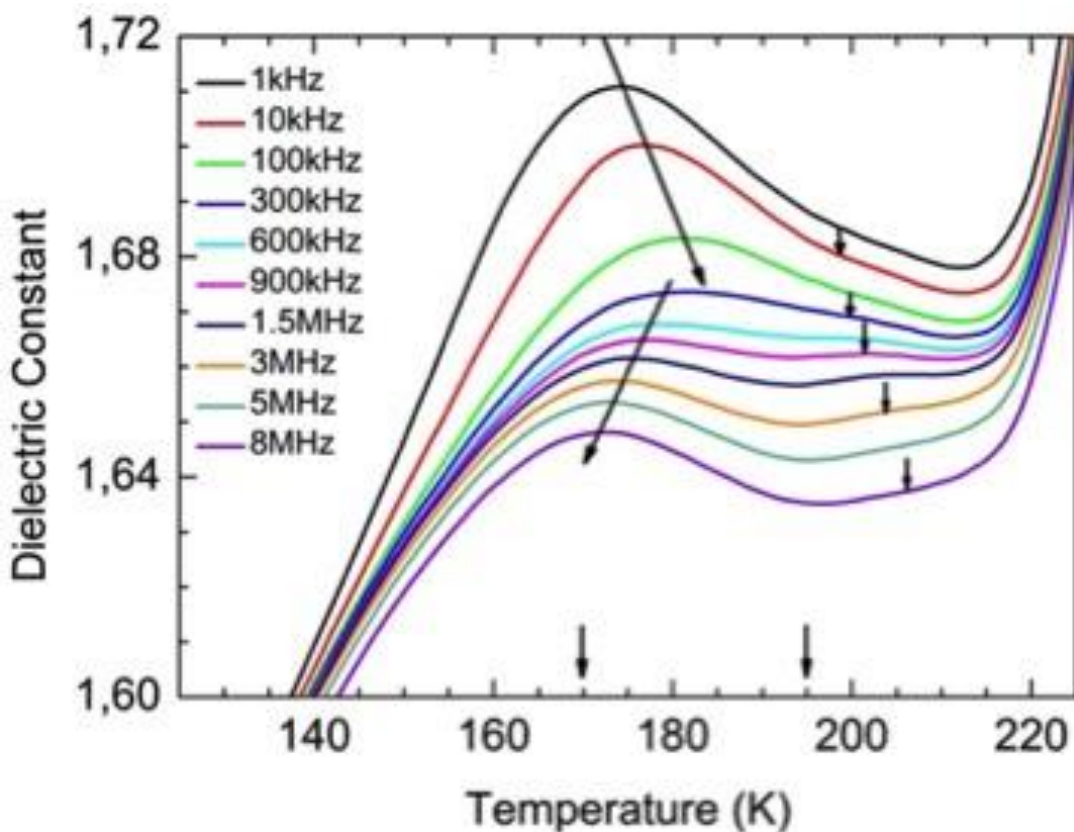
Figure 4.5 : Zoom in to dielectric constant between 130K and 220K. Two relaxation process with small temperature distance is shown. Arrows depict the shift of $\varepsilon'(\omega,T)$ peaks with increasing frequency.

The abrubdt increase of $\varepsilon'(\omega,T)$ above 195 K towards 230K denotes reordering of water molecules through H-Bonds along c-axis of nanotube to build up dipole moment. Increase of dielectric constant ends with a small dielectric constant peak with apparent dispersion about 230 K. This phenomenon can be attributed to the enhancement of orientational motions as a result of the loss of long-range tetrahedral network. This temperature is consistent with temperature of the thermodynamic singularity observed of bulk water at 228 K [56, 57].

A closer examination (Figure 4.4) of temperature range T>230K shows that there is a frequency seperation of dispersion. At $\omega \leq 10$ kHz a strong dispersion occurs without relaxation shift probably related to interfacial motions mobile water between FF rings[20]. Whereas in higher frequency region, $\omega \geq 10$ kHz, relatively weak dispersion with notable relaxation shift of dielectric peak to higher temperatures is observed. The later phenomenon is an indications of bound water molecules to functional groups in pore wall. In the high temperature range at T=300K dipole order breaks down by warming up and long range interactions are lost. As a consequence dielectric constant gets smaller.

Temperature dependence of real dielectric permittivity spectrum points out two distinct locations of water dipoles in FF NT/MT nanocavities. Severe confined with salt bridges to carboxyl and amino groups at the surface and less confined water clusters away from the surface, elongated through the nanocavity.

4.5.2 Differential scanning calorimetry of FF NT/MT

Calorimetric investigations are conducted on self-assembled diphenylalanine nanostrucructure accompany the results obtained by dielectric spectroscopy measurements. DSC measurements are conducted by Prof. Dr. Svetlana Kopyl as a co-worker in our scientific collobration. A brief summary of measurements are as follows, which is depicted in Figure 4.6.
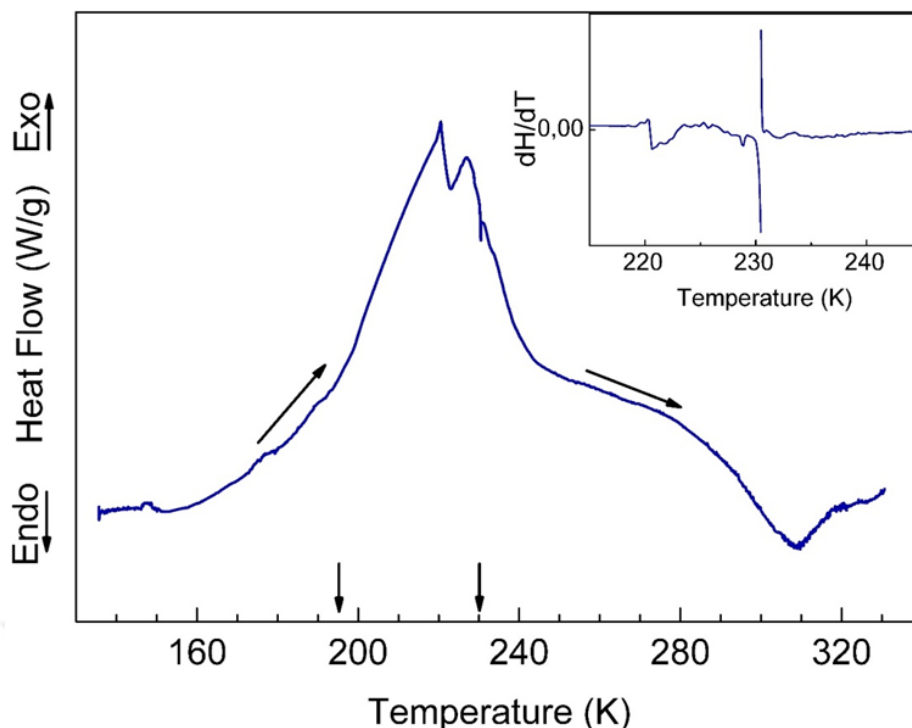
Figure 4.6 : The DSC heating thermograms of FF NT/MT. The average rate of temperature is 5 Kmin[-1]. The arrow denotes phase transitions at 195K and 230K. In the inset the temperature derivative of DSC signal have been shown.

The low temperature structural arrest of water molecules in FF NT/MTs is achieved through a hierarchical slowing down of water motions in FF rings together with the freezing of the relativle free water molecules in large cages, around 133 K. Nevertheless, this Tg value resides in the limit of present experiments. Although there is no indication of glass transition in the obtained DSC results, further inspections might reveal the expected phenomenon (Figure 4.6).

The low temperature plateau of DSC signal transforms into an exothermic response on heating in the vicinity of 160 K, implying the increasing order through the water molecules [117]. The present increament is accelerated furher starting from 195 K. These two temperatures, 160 K and 195K, are also characteristics of dielectric measurement conducted on FF NT/MT, which will be discussed in details in following chapters. At the end of the slope, there are two closely lying peaks, probably related to pre-translational phase seperation due to water molecules residing in different confinements in FF NT/MT, possesing dissimalar free energies. The derivative of the heat flow with respect to temperature reveales a singularity at 230 K, consistent with the well-known structural transition temperature of bulk water [116,56] (inset to Figure

4.6). Present results do not reflect previously found behaviors of water confining materials; neither soft [93,97,84], nor hard [91, 94, 95, 96]. Discontinuity of the heat flow is in agreement dielectric peak at 230 K. The combined results of dielectric and DSC measurements show that the transition at 230 K has a structural character. Namely, a transition of loss of long-range order of tetrahedral water. The heat flow transforms into an endothermic regime at temperatures above 230 K confirming the frustration long-range dipole order in FF peptides. It has to be noted that, the minimum of the heat flow in the endothermic regime is approximately at the same temperature as the $\varepsilon'(T)$ main peak.

4.5.3 Dielectric loss spectroscopy of FF NT/MT

Comparison of dielectric loss spectra of sealed and dehydrated samples clearly shows that observed dielectric relaxation processes are related only to confined water. From Figure 4.7, it is clear that dehydration of FF NT/MT samples in vacuum 10^{-3} mbar at room temperature lead to dissapearing of dielectric loss peaks in wide temperature range. For example, flat of dielectric loss at low temperature and remarkable difference in the dielectric loss peak value at high temperatures allow us to conclude that the dielectric loss peaks (black points) on Figure 4.7 are related to confined water.
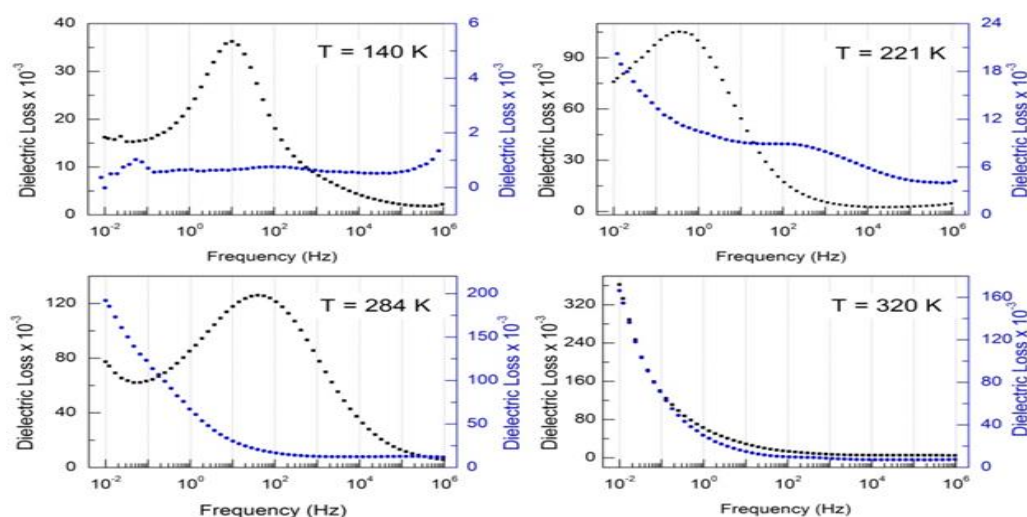
Figure 4.7 : Dielectric loss of FF NT/MT of sealed and dehydrated samples at several temperatures. Black dotes belong to sealed sample, whereas blue dots belong to non-sealed samples.

We would like to underline that the evidence of easy dehydration suggests that FF nanochannel are shouldn't be considered as continious tubes with rigid walls, rather as porous structure.
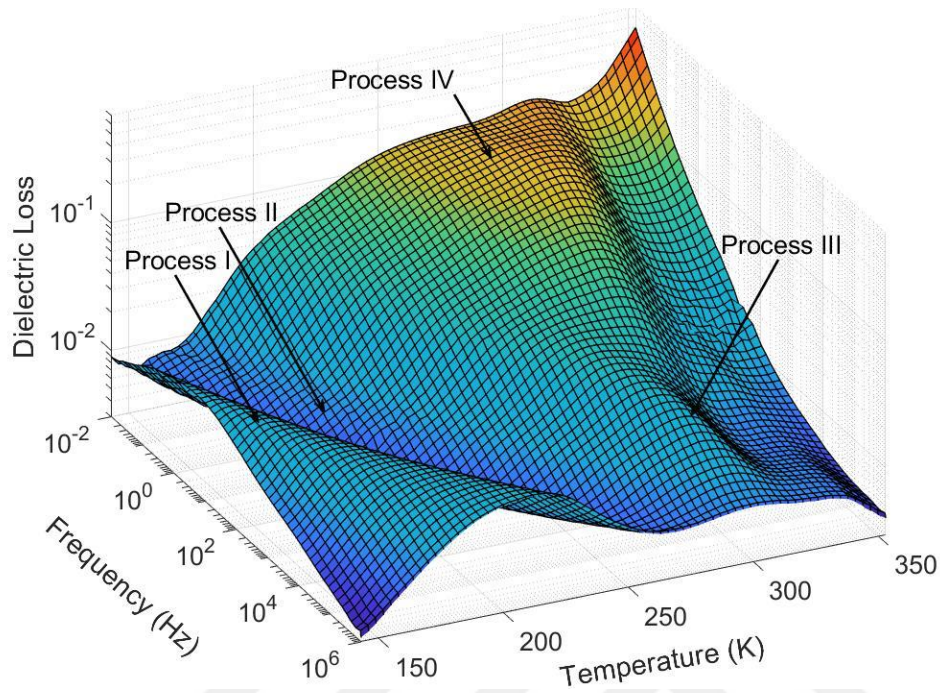
Figure 4.8 : 3D plot of dielectric loss spectra of sealed FF NT/MT sample.

Four relaxation processes, Processes I, II, III and IV, are revealed in dielectric loss spectroscopy conducted between 150 K and 350 K (Figure 4.8). Enumaration is made by the order of appearance in the frequency window from low to high temperatures. All observed relaxational processes demonstrate different mechanisms. On the crown of 3D plot, process IV exhibit saddle-like evolution first observed for water in different confined medium [118, 111, 119] and theoretically described [112].
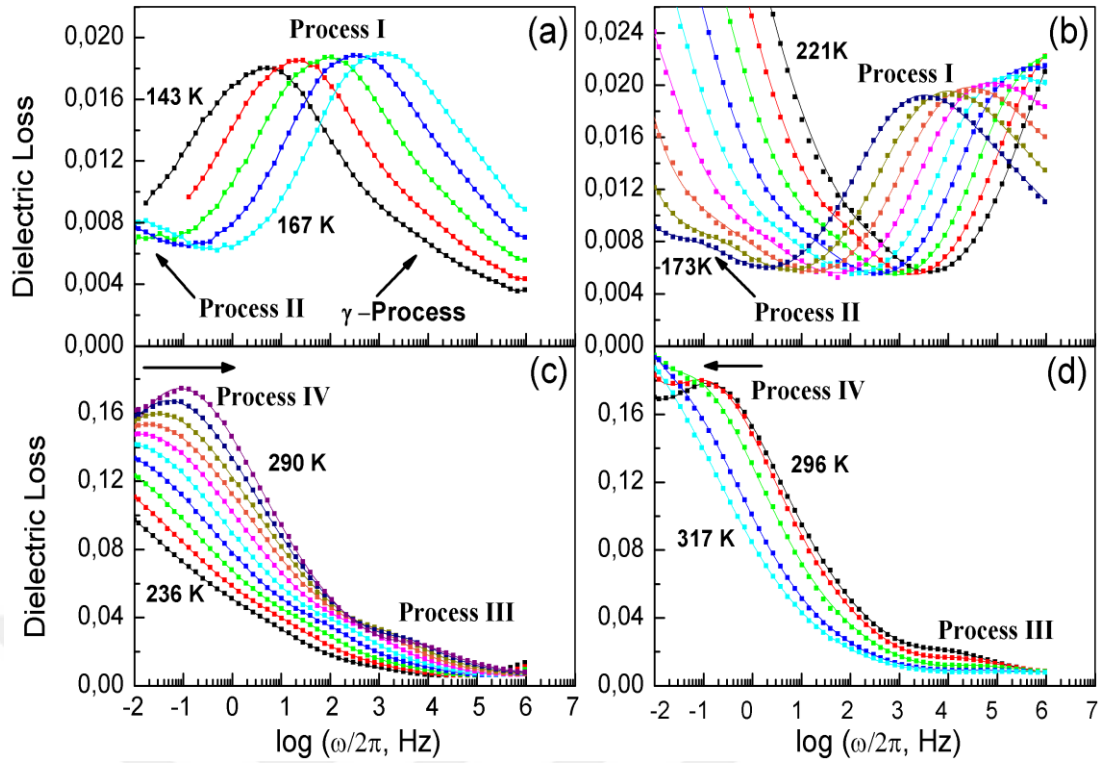
Figure 4.9 : Evolution of loss spectra of FF NT/MT with Temperature. Spectra are drawn with 6 K intervals. Four distinct relaxation process is shown. Solid lines are fitting lines with. Black arrows in (c) and (d) shows the direction of shift in dielectric loss peak with rising temperature.

Dielectric loss spectra in succesive temperatures is given in Figure 4.9, where the hierarchichal order of processes are appears. Low temperature γ-Process indicates the existence of localised motions attributed to side groups or shorter segments (Figure 4.9a). In Figure 4.9a and 4.9b, evolution of Process I from symmetrical into assymetrical relaxation dynamics can be observed. The same process reaches to high limit of frequency window, 10^6 Hz, without fading. To be able to track this process in higher frequencies we conducted an RF dielectric spectroscopy measurement (Figure 4.10). Only by visual inspection, relatively low dielectric strength of processes III and IV is obvious. To obtain the quantitative values, we applied curve fitting with Havriliak-Negami model as explained in chapter 4.2. Applying the fitting procedure on results of the both experiments we draw the Arrhenius plot in Figure 3.7. Fitting parameters of relaxation times, τ^I, τ^{II} and τ^{III} are given in Table 4.1, whereas fitting parameters of the non-monotonic τ^{IV} are given in Table 4.2.
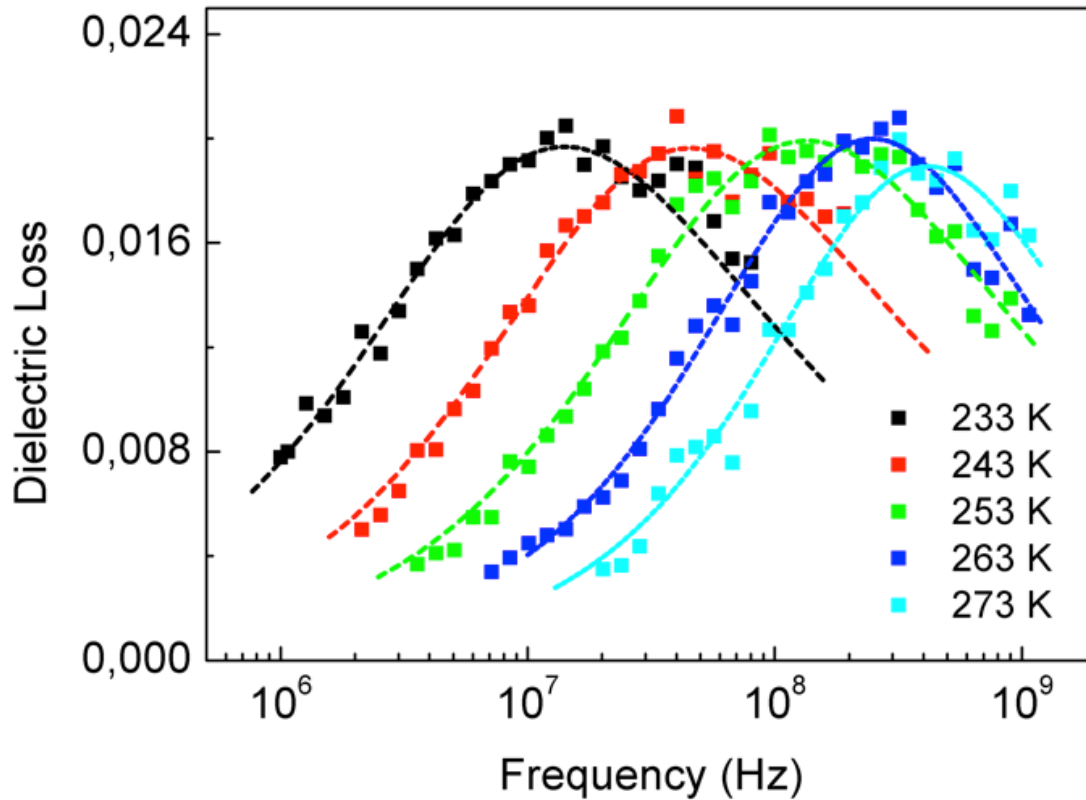
Figure 4.10 : Dielectric loss spectra of FF NT/MT from 10^6 Hz to 10^9 Hz

Fitting procedures as explained in chapter 4.2 is used to obtain temperature dependences of relaxation times, τ. Low frequency side of τ^I has an Arrhenius type evolution modelled with formula (4.10) with temperature but after the crossover around 165 K τ_I behaves as α-relaxation, defined by Vogel-Fulcher-Tamman (VFT) relation (4.11). The same process has another crossover into a second α-relaxation around 195 K. Relaxation time τ^{II} demonstrates succesive α-relaxation behaviors with a crossover in the vicinity of 195 K. All these temperatures are in line with the dielectric anomalies explained in Chapter 3.1. Observed crossovers and anomalies are also consistent with the differential scanning calorimetry (DSC) on FF NT/MT (Figure 4.6).
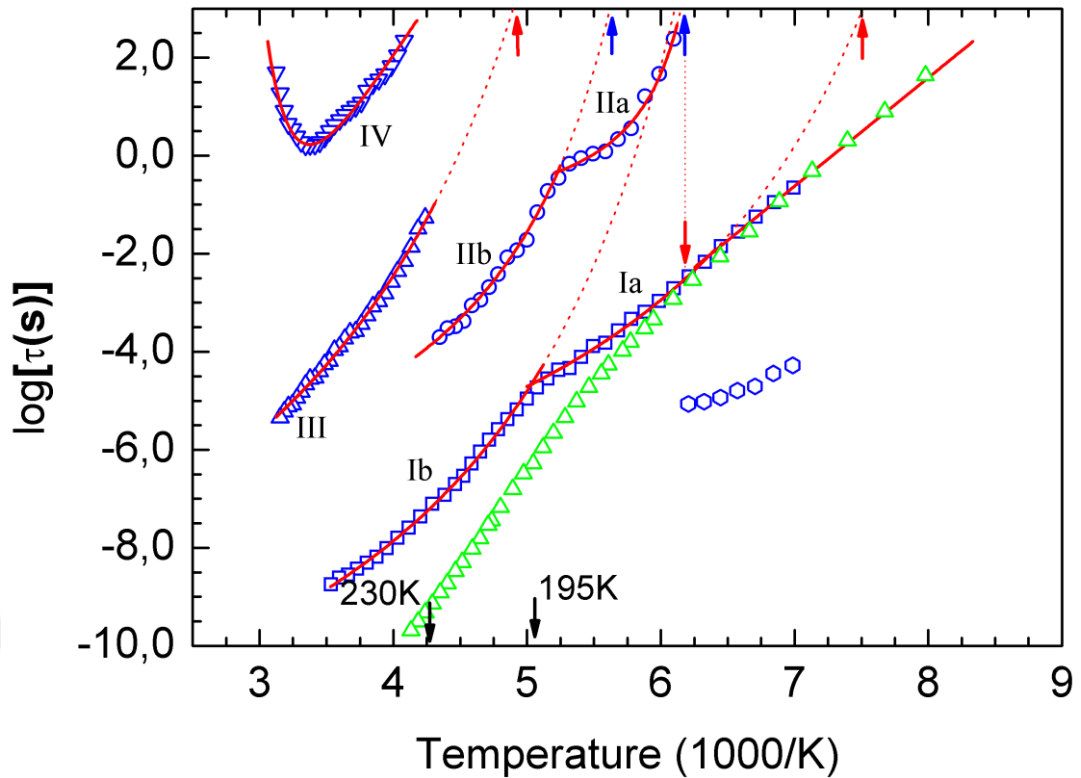
Figure 4.11 : Activation plot of relaxation times of observed processes in FF NT/MT. Solid lines are fitting curves by Arrhenius and Vogel-Fulcher-Tammann relation. The dash red lines ends with red arrows at 10^3 second defines successive dielectric T_g values at 202K, 136K and and blue arrows, T_f values at 179K, 162K. Downward red arrow indicate the temperature of αβ-crossover of process I. Black arrows indicate phase transition temperature observed in permittivity spectra. Empty hexagons represent γ-process. Green triangles denote relaxation times of water confined in MCM-41 C10, shown for comparison, data taken from [20].

Above the phase transition in the vicinity of 230 K, τ^{II} is terminated. Two new processes emerged in this temperature region; τ^{III} evolves into VFT relation in temperature and τ^{IV} demonstrates a non-monotonic temperature dependence as explained by Ryabov *et al* as surface behavior of water dipoles [112].

Table 4.1 : Fitting parameters of VFT and Arrhenius relations for processes in FF peptide. T_g (K) and T_f (K) are glass transition temperature and freezing temperatures, respectively, obtained by extrapolation of VFT curves to $\tau = 10^3$ s. Freezing temperature T_f indicates the onset of dipole contributions of related processes.

Parameters	Process Ia Arrhenius	Process Ia non-Arrhenius	Process Ib non-Arrhenius	Process IIa non-Arrhenius	Process IIb non-Arrhenius	Process III non-Arrhenius
τ_0 (s)	$1.6 \cdot 10^{-17}$	$1.1 \cdot 10^{-8}$	10^{-12}	$3.7 \cdot 10^{-2}$	$1.1 \cdot 10^{-7}$	10^{-10}
E_a (kJ/mol)	44.3	-	-	-	-	-
D	-	2.95	4.00	0.27	1.57	5.29
T_{VFT} (K)	-	105	129.6	153	155	146
R^2	0.9866	0.9917	0.9873	0.9860	0.9941	0.9963
T_g (K)	-	133	-	-	-	205
T_f (K)	-	-	163.8	162	179	-

4.5.3.1 Processes I and II

Process I is approximately four orders faster than process II as seen in Figure 4.7. Such a heterogenity of dipole moments is expected only if different constraints are imposed on different groups of water molecules. As outlined in Chapter 2, structure of FF NT/MT nanocavities posses periodically spaced hydrophilic amino and carboxyl functional group which is cause higher constraint on water molecules leading to a severe confinement. The fact that lattice parameter c = 5.456 Å is two fold of the lattice size of tetrahedral water which is 2.56 Å hints a tetrahedral water network between neighboring FF rings in c-axis. Furthermore, porosities between neighboring 1nm channels provide cages a larger free volume which help replenish the hydrogen bonds required for building tetrahedral water. Cerveny et.al. argued that in chemically active silica pores, structural relaxation of water dipoles will be several orders slower near the pore walls than away from the liquid-solid interface [90]. Near the liquid-solid interface, the water molecules are called solvation shell. Previous studies have shown that there are two main solvation shells in FF rings since both amino and carboxyl

groups provide possible hydrogen bond locations [5]. We expect that this less confined water in expanded molecular free volume will have faster relaxation dynamics, called Process I, than severely confined water molecules, Process II, at nanocavity surface.

At low temperatures, process Ia is broad and symmetrical which is typical for β-relaxation of supercooled confined water (Figure 4.9a and Figure 4.11). Activation energy, $E_a = 44.3$ kJ/mol is approximately similar with previously published data [120, 121, 20]. Accordingly, low temperature β-relaxation related to the low temperature activated process of supercooled water.

By warming up, β-relaxation behavior of process Ia changes into an α-relaxation with an $\alpha\beta$-crossover at T=162 K. This temperature overlaps with freezing temperature T_f = 162 K of process IIa (Table 4.1), signaling a correlation between two processes. Subsequent thawing of water confined in large cages between FF rings initiate hydrogen bond formation resulting a cooperative motion of water molecules located in solvation shell in FF rings. Softening of first solvation shell's vitrified state by increasing temperature is responsible of for the α-relaxation behavior of process IIa. A similar dynamic occurs by salol, a low molecular weight glass-forming liquid, confined in anodic aliminium membran of different pore sizes [122]. This observation is in line with the onset of exothermic heat flow in DSC data around T=160 K, shown in Figure 4.6.

Cooperativity of water molecules in large cages with solvation shell in FF rings provides an insight to complex behavior of real dielectric constant around 170 K (Figure 4.5). $\varepsilon'(\omega, T)$ peak shifts to high temperature by decreasing frequency signifying the growing cooperativity length, thus growth of water clusters in FF nanochannels. This argument is supported by the increase in relaxation strengths of procces I and II towards 195 K by warming up as seen in Figure 4.12. By the formation of hydrogen bonds between nanoregions, average orientational contribution to dipole moment grows, as a consequence dielectric response gets bigger. Thus, $\varepsilon'(\omega, T)$ peak around 170 K should not be considered as a sign of an exact phase transition.

In higher temperatures, a crossover into another α-relaxation occurs at 195 K in both processes I and II. We called these α-relaxations as process Ib and IIb. Higher strength parameter D qualifies an increase in fragility in hydrogen bonds [84]. It is remakable that, freezing temperature $T_f = 163.8$K of process Ib (Table 4.1) overlaps with the onset

temperature of process IIa as seen in Figure 4.11 and also with the onset of exothermic heat flow (Figure 4.6) within fitting error. We believe that the thawing of water molecules in the second solvation shell is the reason for process IIb. This dynamic crossover is provided by the increase in number of hydrogen bonds. As a consequence, the softening of vitrified state of water confined in FF rings is achieved and through interchange of hydrogen bonds between solvation shells and water in large cages between FF rings, leading to formation of tetrahedral order along z-axis in temperature range between 195 K and 230 K. It should be noted that $\Delta\varepsilon^{I}$ increases greatly, whereas $\Delta\varepsilon^{II}$ dimnishes as temperature approaches to 230 K (Figure 4.12). Due to sufficient free volume, significant stretch of hydrogen bonds related to process I defines the dipole contribution to the dielectric peak at 230 K (Figure 4.1).
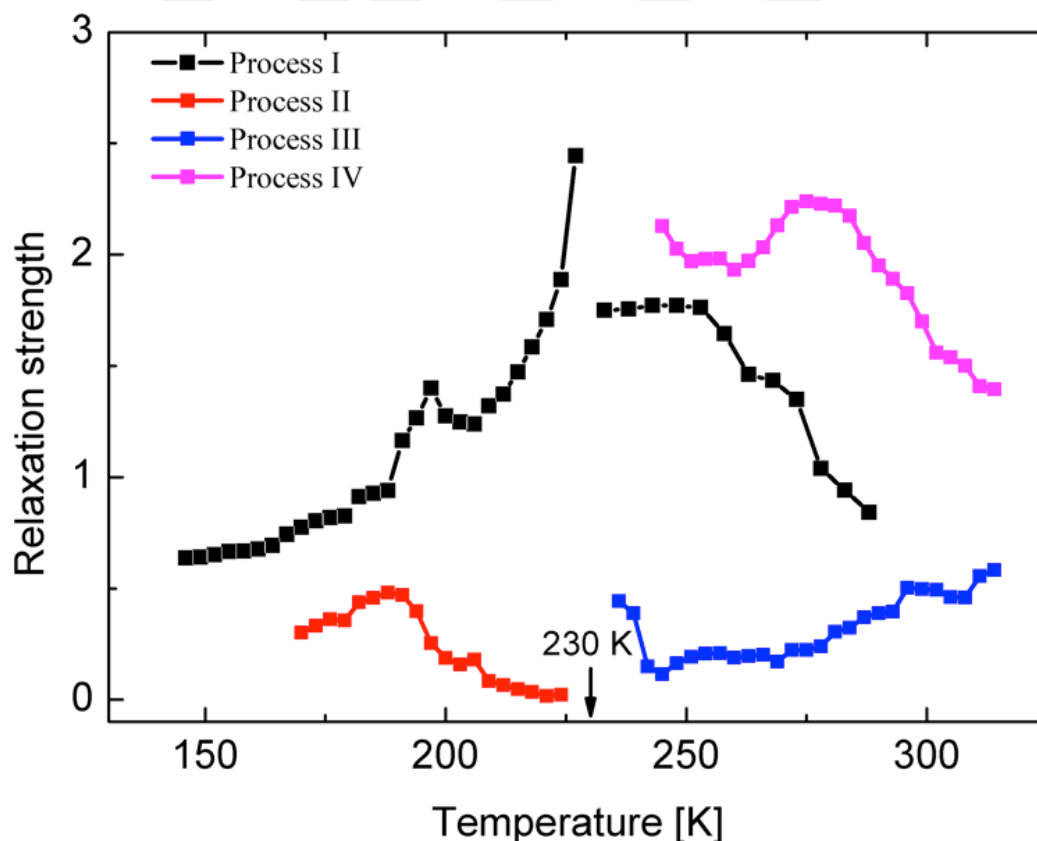
Figure 4.12 : Temperature dependence of dielectric relaxation strengths $\Delta\varepsilon$ of water dipoles located in different confined in FF NT/MT. The black arrow indicates phase transition temperature according to dielectric constant on Figure 1.

Multiple α-like structural relaxations are found. Different confinements of water molecules are responsible for two coexisting relaxation processes between

temperatures 150 K and 230 K. An overall gap of 10^4s in relaxation times, τ, indicates a difference in the nature of confinement. Process I is related to the water molecules in large cages between FF rings, having propably liquid-like state. On the other hand, process II is related to the solvation shells which is in contact with NH_3^+ and COO^- functional groups located in the nanocavity walls. Previous calculations have shown that $O - H$ length near amino groups are tend to be shorter than hydrogen bonds between carboxyl groups [123]. Thus, we can conclude that process IIa and IIb are related both to thawing of water molecules bound to carboxyl groups and protonated amino groups, consequently.

The VFT fitting applied on the relaxation times of α-relaxation process Ia defines glass transition $T_g = 133$ K (Table 4.1), which is close to calorimetric $T_g = 136$ K found by Johari for bulk water [114, 115]. Considering previous researches for confined water [93] and other glass-forming liquids [124, 125] a glass transition is not expected in 1 nm confinement which FF nanotubes provides. Thus, we propose that cooperative regions are not limited by single nanochannels but can elongate between neighboring nanochannels by proton dynamics.

4.5.3.2 Process III and IV

Exothermic trend in DSC signal has two peaks when temperature approaches to 230K (Figure 4.6) just before the endothermic signal starts with a discontinuity at 230 K (inset Figure 4.6). Closely lying peaks probably reflect the pre-transitional phase separation related to water molecules in different confinement in peptide nanocavity. Termination of heat release signifies the frustration of low-temperature long-range dipole order of water molecules in FF NT/MT. Note that the discontinuity temperature in DSC coincides with real dielectric peak at 230 K (Figure 4.4). A characteristic glass transition in calorimetric signal is absent as was found in Ref.[21] on the examples of confined water in MCM-41 matrices. In FF NT/MT, this temperature can be identified as transition from low temperature long-range order of tetrahedral water to the phase of frustrated long-range order at T>230 K.

Two distinct relaxation dynamics are found between 230 K and 330 K. This is in line with the heterogeneity observed for two different dispersion dynamics in real dielectric constant (Figure 4.4) at T>230K. The strongly dispersive low frequency behavior in $\varepsilon'(\omega, T)$ at ω<10 kHz is attributed to the saddle-like process IV related to interfacial

water [20, 128, 111, 112]. However, process III mimics the behavior of fragile liquids [84] related to tetrahedral water with strength parameter D=5.29 (Table 4.1).

In one diphenylalanine hexamer, there exist six COO^- and six NH_3^+ providing in total 12 water bonding sites. These bonding sites repeats themselves periodically along the peptide backbone. Above 230 K, short range dipole orders maintain themselves in fixed positions around hydrophilic amino and carboxyl groups in hexagonal FF rings even in high temperature phase. These local ordered water dipoles give rise to broad real dielectric peak that shifts to higher temperatures at $\omega > 10$ kHz. An inspection of TVFT values of process II and process III indicates that saturation of configuration entropy of both processes comes up to same temperature region (Table 4.1). This observation is an evidence to argue that both α-relaxations II and III belong to the same tetrahedral confined water configuration in FF rings even though they belong to different phases. Process III, is the α-relaxation belongs to water molecules which maintain tetrahedral structure by short range order throughout the nanocavity by prolate clusters.

The loss of long-range H-bond network, weakens dynamical constraints in FF rings. Low value of dielectric strength $\Delta\varepsilon^{III}$ confirms this observation (Figure 4.12). Besides, high temperature imposes high entropy leading to an increase in defect density in tetrahedral water (Table 4.1). Thus, the glass transition temperature $T_g = 205K$ becomes higher compared with bulk water [57]. Chonde and co-workers argued that T_g of amorphous solid water may vary between 120 to 220 K [126]

In the high temperature range, T>230 K, a second relaxation is identified as Process IV, whose relaxation times demonstrate non-monotonic temperature dependence (Figure 4.11). We used an model developed by Ryabov et al to define this saddle-like relaxation behavior of τ_{IV} The fit parameters obtained by the formula (4.13) is identified is given in Table 4.2.

Table 4.2 : Fitting parameters of non-monotonic process IV.

Parameters	Process IV
τ_0 (s)	$5.01 \cdot 10^{-15}$
E_a (kJ/mol)	34
E_d (kJ/mol)	44.7
$\eta = 1/C$	$1.6 \cdot 10^8$
R^2	0.9838

We would like to underline that the definition of surface depends on the phase and mobility of confined water molecules. Relaxation times of saddle-like relaxation Process IV are about 4 orders slower than short-range order tetrahedral α-relaxation Process III. Thus, we argue that, significant dynamical constraints acting on this cluster are more severely confining than water molecules bound to the ordered NH_3^+ and COO^- groups in FF NT/MT nanocavity. Dehydration of FF nanotubes at 10^{-3} mbar in room temperature has shown that nanocavities have porous morphology between neighboring nanocavities (Figure 4.7). Rather long relaxation times of process IV points out the probability that in high temperatures, water molecules are confined in pores between nanotubes.

Dynamics of water molecules confined in pores start with a rotational motion, Arrhenius-like behavior, just above 230K, which is fitted by the first exponential term in equation (4.13). The temperature of τ^{IV} minimum (Figure 4.11) coincides with the temperature of maximum real dielectric constant shown in Figure 4.4. Maximum contribution of water dipole reorientations is responsible for the dielectric peak. On the other hand, τ^{IV} minimum might be a mobility threshold that limits transfer rate of water molecules. Pinning of water molecules on the surface of pores leads to slowing down of the relaxation times in process IV. Above the peak temperature 300 K, second term in equation (4.13) becomes dominant

A similar phenomenon, where the relaxation rate slows down is attributed to the loss of water in previous literature [20]. In case of a loss of polar molecules, the indication should be obvious in conductivity spectrum of sample. The conductivity of our FF peptide samples in the range of 230 K and 320 K remains in the vicinity of 10^{-15} Sm/cm, so we argue that there is no loss of decoupled 'free water' from the FF NT/MT system in this temperature range (Figure 4.13). Nevertheles, the power-law of σ(T) at

high temperatures, blue line, is attributed to hopping conductivity [127] since s ≈ 0.6 in the $\varepsilon'' \sim \sigma\omega^{-s}$ dependence FF NT/MT samples.
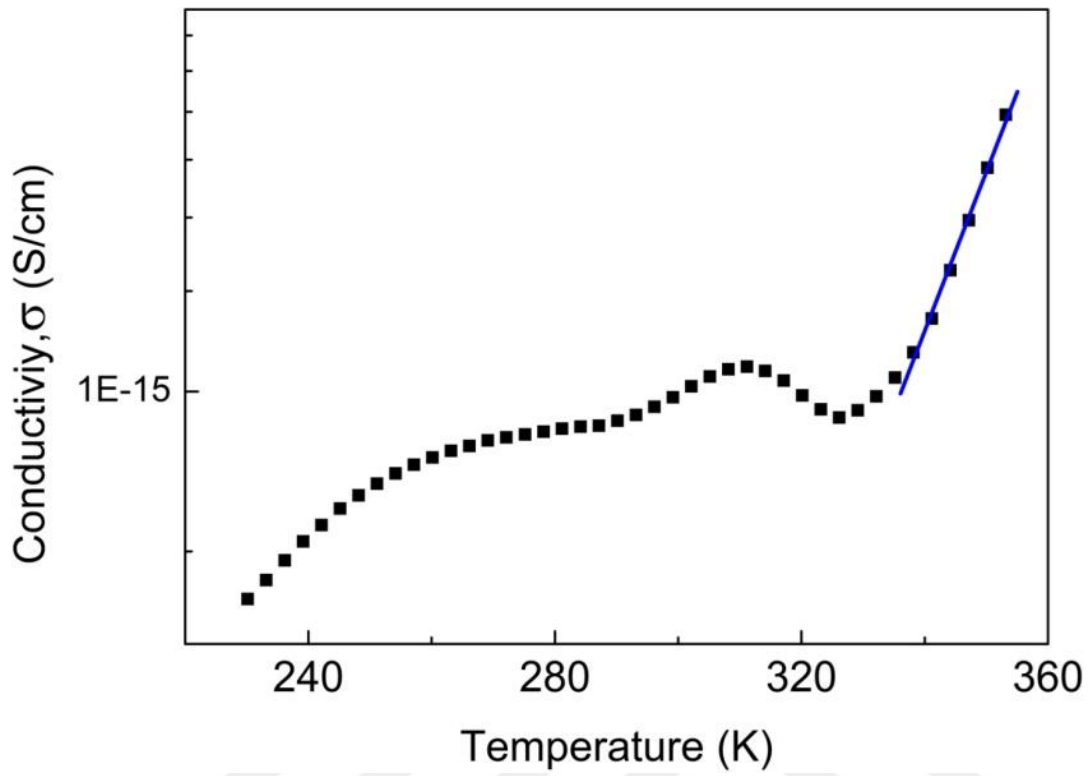
Figure 4.13 : Temperature dependence of conductivity of FF peptide samples measured at 10^{-2} Hz.

5. FOURIER TRANSFORM INFRARED SPECTROSCOPY OF WATER CONFINED IN FF NT/MT

5.1 Theory of Molecular Vibrations In Infrared Spectra

Transitions in electronic energy levels demonstrate themselves in UV and visible spectrum of electromagnetic radiation. At lower energies than the electronic energy levels transitions occur as molecular vibrations. These vibrational energies correspond to infrared region of the light spectrum. Both infrared absorbtion and Raman scattering spectroscopy are utilized as complementary methods to investigate molecular vibrations.

Transitions in infrared spectrum have different nature than electronic transitions. Infrared absorbtion spectrums provide valuable informations about the structural properties of molecules. Vibrational spectra can be explained both by classical and quantum mechanical theory.

5.1.1. Classical theory of infrared absorption spectra

According to electromagnetic theory of light, emission and absorption of electromagnetic energy depends on the existence of charges. Change in dipole moments determines the intensity of emitted or absorbed energy.

Let's consider a diatomic molecule. In unit time, intensity of absorbed energy is proportional to the square of the dipole moment's amplitude:

$$W_{absorbed} \sim |\mu|^2 \tag{5.1}$$

Amplitude of the dipole moment is a function of the distance, $P(r)$, between atoms in a diatomic molecule, which can be expanded about the equilibrium distance r_0:

$$\mu(r) = \mu(r_0) + \left(\frac{\partial \mu}{\partial r}\right)_{r=r_0} (r - r_0) + \sum_{n=2}^{\infty} \frac{1}{n!} \left(\frac{\partial^n \mu}{\partial r^n}\right)_{r=r_0} (r - r_0)^n \tag{5.2}$$

If the vibration is assumed to be quasiharmonic:

$$r - r_0 = a_0 \cos(2\pi v_{vib} t) \tag{5.3}$$

where a_0 denotes the amplitude and v_{vib} denotes the frequency of the vibration. Then the interatomic distance can be written as:

$$r = a_0 + a_0 \cos(2\pi v_{vib} t + \delta) + \sum_{k=2}^{\infty} a_k \cos(2k\pi v_{vib} t + \delta_k) \qquad (5.4)$$

where a_0 is the amplitude of the fundamental oscillation, a_k is the amplitude of k th oscillation, δ and δ_k denote the initial oscillation phases.

When 5.2 and 5.4 is combined, dipole moment appears to be equal to a sum. The first term of this sum is time independent whereas others are time dependent with different frequencies. First term of 5.2 is the fundamental mode in the IR spectrum. Terms of the sum denote the nonlinear dipole moment which depend on interatomic distances. These terms are called overtones.

By harmonic assumption higher terms in the sum of 5.2 and 5.4 can be neglected, thus:

$$\mu(r) = \mu(r_0) + \left(\frac{\partial \mu}{\partial r}\right)_{r=r_0} a_0 \cos(2\pi v_{vib} t + \delta) \qquad (5.5)$$

It is clear from 5.5 that change in dipole moment causes only one fundamental oscillation mode in IR spectrum of the molecule. The phase of the molecular vibration is same with the incident electromagnetic wave. Intensity of the fundamental mode is given as:

$$I \sim \left[\left(\frac{\partial \mu}{\partial r}\right)_{r=r_0} a_0\right]^2 \qquad (5.6)$$

The value of $\left(\frac{\partial \mu}{\partial r}\right)_{r=r_0}$ is equal to the value of the effective molecular charge.

From the deduction above, it is clear that a diatomic molecule can posses an vibrational mode in infrared spectra if there is a change in the dipole moment. Thus, a selection rule $\left(\frac{\partial \mu}{\partial r}\right)_{r=r_0} \neq 0$ can be given for a vibrational transition to be active in IR spectrum.

Similar approach can be obtained for polyatomic molecules. In that case, interatomic distance r must be replace by normal coordinates Q. Q and r are related with the formula given:

$$Q_i = \sum_{\lambda=1}^{\rho} C_{i\rho} r_\rho \qquad (5.7)$$

where ρ denotes the degree of freedom and $C_{i\rho}$ are the coefficients.

If the $C_{i\rho}$ are defined, kinetic (E_k) and potential (E_p) energies can be calculated by using normal coordinates:

$$E_k = \frac{1}{2}\sum_i M_i \dot{Q_i}^2 \tag{5.8}$$

$$E_p = \frac{1}{2}\sum_i k_i Q_i^2 \tag{5.9}$$

where M_i and k_i are the effective mass and elasticity constant of molecules.

So, all possible molecular vibrations can be obtained. For polyatomic molecules, a molecular vibration can occur in infrared spectrum only if it has a derivative of dipole moment with respect to its normal coordinates $\left(\frac{\partial \mu}{\partial Q_i}\right) \neq 0$. On the other hand, Raman spectrum has a similar selection rule but related to polarizability $\left(\frac{\partial \alpha}{\partial Q_i}\right) \neq 0$. Both spectra are needed to fully investigate oscillations of a vibrational transitions of a polyatomic molecule.

5.1.2. Quantum mechanical theory of infrared spectra

When a molecule irradiated by an infrared light, the molecule absorbs exact amount of energy which is needed for the transition of vibrational energy from level to higher level:

$$hv = E_n - E_m \tag{5.10}$$

where h is the Planck's constant, v is the frequency of absorbed electromagnetic wave, E_n and E_m denote the nth and mth vibrational energy levels.

Satisfying this simple condition, 5.10, alone does not always cause infrared absorption. Just like in the classical theory there are selection rules derived from quantum mechanics, which determine active and inactive vibrational energies in IR and Raman spectra.

According to the quantum mechanics intensity of absorbed electromagnetic energy is determined by transition moment, μ_{mn} between two states characterised by wave functions ψ_m and ψ_n:

$$I_i = (\mu_i)_{mn} = \int \psi_m \, \mu_i \psi_n dQ_i \tag{5.11}$$

where Q_i is the ith normal coordinate, μ_i is the dipole moment in ith direction and I_i is the intensity of absorbed energy in ith direction.

As in the classical mechanics theory, 5.11 relates the intensity of absorbed infrared energy to square of dipole moment μ_i, more clearly; $I = \sum_{i=1}^{d}(\mu_i)_{mn}$, where d denotes the number normal coordinates. This relation alone give a trivial selection rule that there is no absorption for $\sum_{i=1}^{d}(\mu_i)_{mn}= 0$, but it is indeed too general.

Distribution of charges in ground state changes with a change in coordinate defining the vibration, therefore dipole moment μ_i is a function of normal coordinate. Furthermore, it can be expanded as follows:

$$\mu_i = (\mu_i)_0 + \left(\frac{\partial \mu_i}{\partial Q_i}\right)_0 Q_i + \frac{1}{2}\left(\frac{\partial^2 \mu_i}{\partial Q_i^2}\right)_0 Q^2 + \cdots \tag{5.12}$$

Using this equation in the eq. 3.11 and keeping in mind that the normal coordinates of a molecule will be quite small. In that case, higher order terms of Q can be disregarded with no error. Thus, we obtain:

$$(\mu_i)_{mn} = (\mu_i)_0 \int \psi_m \, \psi_n dQ_i + \left(\frac{\partial \mu_i}{\partial Q_i}\right)_0 \int \psi_m \, Q_i \psi_n dQ_i \tag{5.13}$$

where state functions ψ_m and ψ_n are orthogonal. Due to orthogonality, the first term vanishes except for m=n, which is the permanent dipol moment of the molecule in ith normal coordinate. The second term provides two condition for non-negative transition moment; $\left(\frac{\partial \mu_i}{\partial Q_i}\right)_0 \neq 0$ which is the same as deducted from the classical theory in section 3.1.1 and $\int \psi_m \, Q_i \psi_n dQ_i \neq 0$. The later condition is known to have solutions using the nature of eigenfunction only for $n = m \pm 1$. At least we have found two particular selection rules for vibrations in infrared spectra; (i) the derivative of the dipole moment with respect to normal coordinates must be nonzero at least in one direction, (ii) regarding that molecules are in the ground state when unperturbed, only the transitions from ψ_0 to ψ_1 is possible which is called the *fundamental. Overtones* are not allowed thus the bands belong to them are very weak.

5.2 Experimental Setup

Mid infrared spectra of FF NT/MT samples are obtained using VERTEX 70 FTIR Spectrometer in transmission mode. The spectrometer is equiped with globar (MIR) source. Infrared laser is directed to the michelson interferometer and to sample with help of a KBr beamsplitter. The light transmitted from the sample is collected with DLaTGS (Deuterated lanthanum alpha alanine doped triglycine sulphate). With the current setup we are able to collect reliable absorbance data in wavenumber range (1000 cm^{-1} – 6000 cm^{-1}) with good signal-to-noise ratio. A schematical description of VERTEX 70 FTIR spectrometer is given in Figure (5.1). The equipement is controlled with OPUS program provided by BRUKER.

Samples are prepared similar to the method desribed in Chapter 3.1. Peptide nanotubes are synthesised on a BaF$_2$ window of 13 mm diameter and 2 mm width. With another BaF$_2$ the sample is sandwiched and isolated by silicone glue attaching two BaF$_2$ windows tightly togeter. Each spectra is obtained in 2 cm^{-1} resolution and as an average of 64 repeated scans. The apperture is chosen to be 3 mm regarding the sample size. Two paralel BaF$_2$ windows are measured as reference before each sample measured. This reference is subtracted from the obtained spectra. Wavenumber accuracy is 0.005 cm^{-1}.
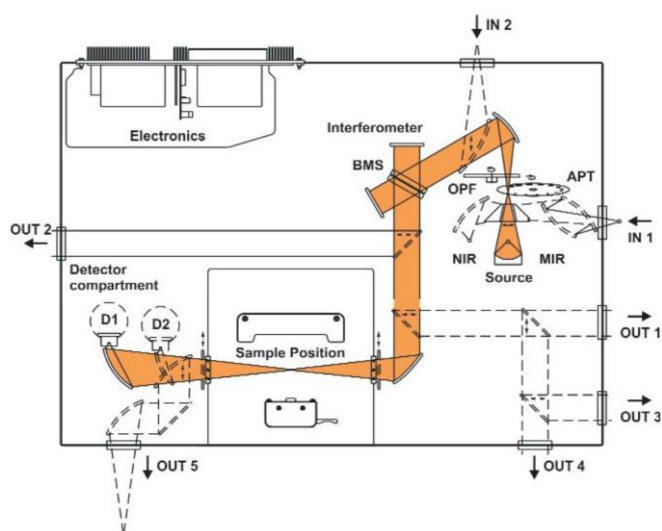
Figure 5.1 : VERTEX 70 setup depicting the optic path.

5.3 Gaussian Fitting and Deconvolution Process of Infrared Spectra

All individual spectra are collected by two succesive measurement each containing the average of 32 runs. These two sets are used to check the 100% line to ensure the stability of each measurements. No deviation greater than 5% is observed from 100% line.

At first, an athmospheric compensation algorihm is applied on FTIR spectra between wavenumbers 1000 cm^{-1} and 6000 cm^{-1} clear the contributions of water vapor and CO_2 gas. Then the baseline of background is calculated and substracted from spectra, in this way the data became ready for Gaussian deconvolution analysis. No smoothing was implemented thus the native features of spectra are conserved.

Wavenumbers of local maxima were appointed by second derivative analysis. Symmetrical mods centered in these wavenumbers are calculated by formula (5.14) and the spectra are fitted by local least square analysis.

$$G(k, w, I) = \frac{I}{\frac{W}{2.355^2}\sqrt{\pi/2}} e^{\left(-2\frac{(k'-k)}{\frac{W}{2.355^2}}\right)} \tag{5.14}$$

Here, k denotes the wavenumber of absorbance maximum, I denotes the amplitude of absorbance mode w denotes the halfwidth of the Gaussian mode. Since in OPUS program the Gaussian function is defined with full width half maximum parameter (FWHM) the standard deviaton is changed with $\sigma = \frac{W}{2.355^2}$.

Whole deconvolution and fitting procedure is started from the lowest temperature, 88 K assuming that the perturbation effects are minimum. RMS values of Gaussian mode fitting procedures in each temperature and spectral range is listed in Table A.1 in Appendix A. Low RMS values ensure the goodness of the fit.

5.4 Results and Discussions

According to literature, at room temperature there four main absorbance bands of bulk water related to following behavior of water molecules (Figure 5.2). They are: connectivity band (100 cm^{-1} – 350 cm^{-1}), libration band (350 cm^{-1} – 1000 cm^{-1}),

bending band (1600 cm^{-1} – 1750 cm^{-1}) and stretching band (3000 cm^{-1} – 3550 cm^{-1}) [104].
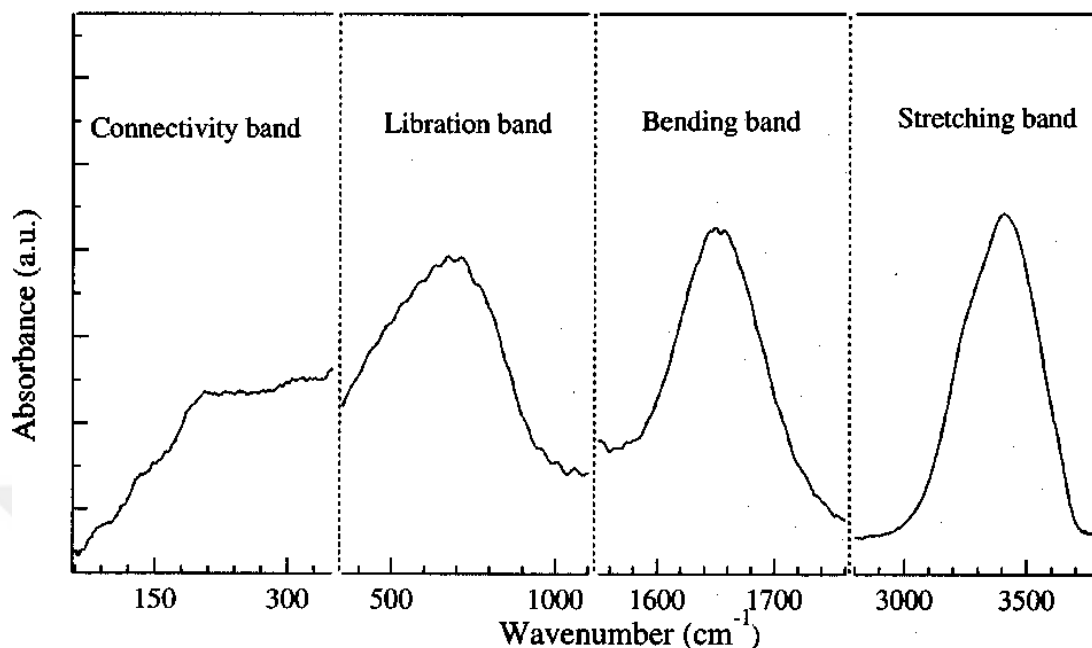
Figure 5.2 : Infrared absorbance bands of bulk water at 298 K [104].

FTIR investigation of self-assembled FF peptides was carried out in frequency range from 1000 cm^{-1} to 6000 cm^{-1} and temperature range 90 K to 330 K. In our spectral window we focused on the bending band and the stretching band of confined water in FF self-assembly.

We explored OH-Stretching (3000 cm^{-1} – 3550 cm^{-1}) and $\widehat{HOH}$ (1450 cm^{-1} – 1700 cm^{-1}) bending bands of confined water in self-assembly FF. OH-stretching band is composed of modes belong to intramolecular interaction of covalently bonded hydrogen and oxygen atoms in water molecules. $\widehat{HOH}$ bending mode is oscilation of angle between two hydrogen in water molecule. Both of these mode will be revealed in appropiated wavenumber region as will be shown below.

5.4.1. OH-Stretching spectra of FF peptide nanostructure

OH-Stretching region of bulk water molecules has a broad absorbance band between 3000cm^{-1} and 3650 cm^{-1} [103]. Researchers used three to four Gaussian component deconvolution to describe the features of bulk water. The central wavenumbers of the Gaussian components are as follows; ω=3295 cm^{-1}, ω=3460 cm^{-1} and ω=3590 cm^{-1}. In

bulk water H-Bond coordination numbers range from 0 to 4. In general, more hydrogen bond on a water molecule will reduce its OH oscillation strength. Thus it is expected to have lower value of characteristic wavenumber peak with increasing coordination number. With this argument, low wavenumber Gaussian component (ω=3295 cm^{-1}) is defined as 'network water' which is bounded with four other water molecules in a completed tetrahedral order [104]. The highest wavenumber Gaussian component (ω=3590 cm^{-1}) is attributed to 'multimer water' molecules whose coordination numbers are less than two. The remaining Gaussian component in the middle (ω=3460 cm^{-1}) is called 'intermediate water' with coordination numbers two and three [103]. These water molecules are continuosly breaking and forming the transient hexagonal water. Relative area under Gaussian curves of each component gives the population of related water dipoles.

We have obtained the OH-stretching band of confined water in FF NT/MT in frequency range from 3000 cm^{-1} and 3550 cm^{-1}. At room temperature the envelope of the experimental data has two independent regions. The first region is centered around 3200 cm^{-1} is attributed to tetrahedral water with coordination number equal to 4 [97]. The second region is centered around 3400 cm^{-1} and it is related with water molecules poorly connected with peptide nanochannels.
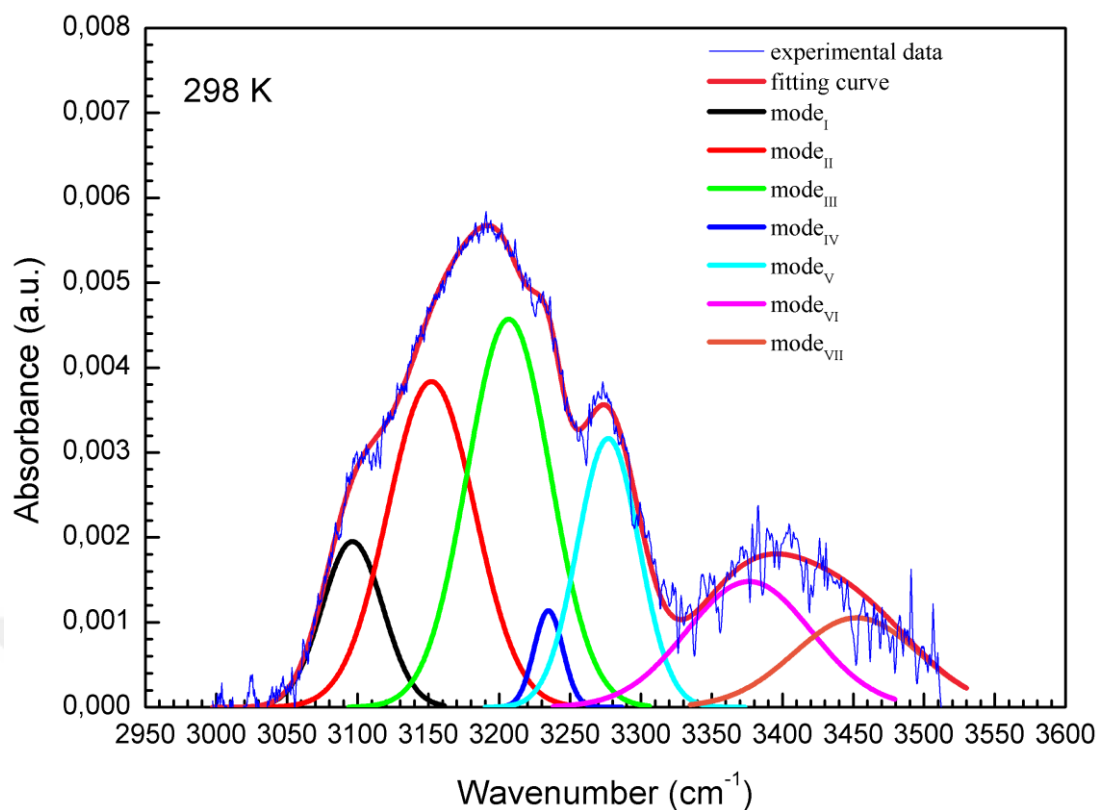
Figure 5.3 : OH-stetching band of confined water in FF peptide at 298 K.

The main envelope is related to water molecules confined in diphenlyalanine hexagonal ring. From Figure 5.3, it is seen that room temperature envelope related to confined water is formed by 6 Gaussian components. The components with high intensity belong to stretching oscillations of water molecules located in th FF ring. According to literature [128], in peptide structures it is known that non-hydrogen bonded NH-Stretching mode is located around 3240 cm^{-1}. Mode IV is the NH-stretching mode.

There are variety of H-bonds structured in FF NT/MT filled with water molecules. First of all two diphenylalanine molecules are bound together with N-H…O-C forming the FF hexamer [129, 5]. Then there are H-Bonds between moieties on the peptide backbone and water molecules confined in the FF hexamers. Namely, C-H…O-H at carboxyl group (-COO$^-$) and N-H…O-H at   and between water molecules which are tetrahedrally order by O-H…O-H motif [129, 5]. Each OH-stretching mode observed in FTIR spectra corresponds to motives in different location. Mode I with wavenumber k_1=3100 cm^{-1} can be assigned OH-stretching in most severe confinement probably bonded between two diphenylalanine in hexamers. Mode II, with k_2= 3155 cm^{-1} is an OH-stretching absorbance mode which arrises N-H…O-H motif between NH$_3^+$

molecules. Relatively low values of these two oscillation frequencies arise from the severe confinement on the peptide surface. Mode III with k_3 = 3205cm^{-1} belongs to water molecules beyond two solvation shells and forms tetrahedral water which are loosely bonded to carboxyl groups. Similar conclusion was obtained by Mallamace *et al* for water confined in MCM-41 with pore diameters of 1.4 nm [97]. Furthermore, k_5 = 3275 cm^{-1} can be described as loosely bonded tetrahedral water probably located between hexagonal FF rings. High frequency flank of OH spectra, consist of two modes; mode VI with k_6 = 3375 cm^{-1} and mode VII with k_7 = 3460 cm^{-1} forms a separate envelope with lower intensity than the envelope related to tetrahedral water configuration. This means that the density of water molecules with incompleted (i.e. less than 4) H-Bond number, is significantly lower than the density of tetrahedral water clusters. We would stress that mode VI and VII represent the movable water molecule in FF peptide nanostructre.

5.4.1.1 Temperature dependence of OH-Stretching Spectra

OH-Stretching spectra of H_2O molecules confined in peptide nanotube are shown in Figure 5.4 ranging from 88 K to 298 K with 5 K temperature steps. Hierarchical phase transitions obtaied by BDS at 195 K and 230 K are clearly revealed also in temperature FTIR spectroscopy as can be seen from the discontinuities in absorbtioa spectra in Figure 5.4a and Figure 5.4b, respectively. These correspondances between different techniques inhering distinct frequency ranges are strong evidences for our findings.
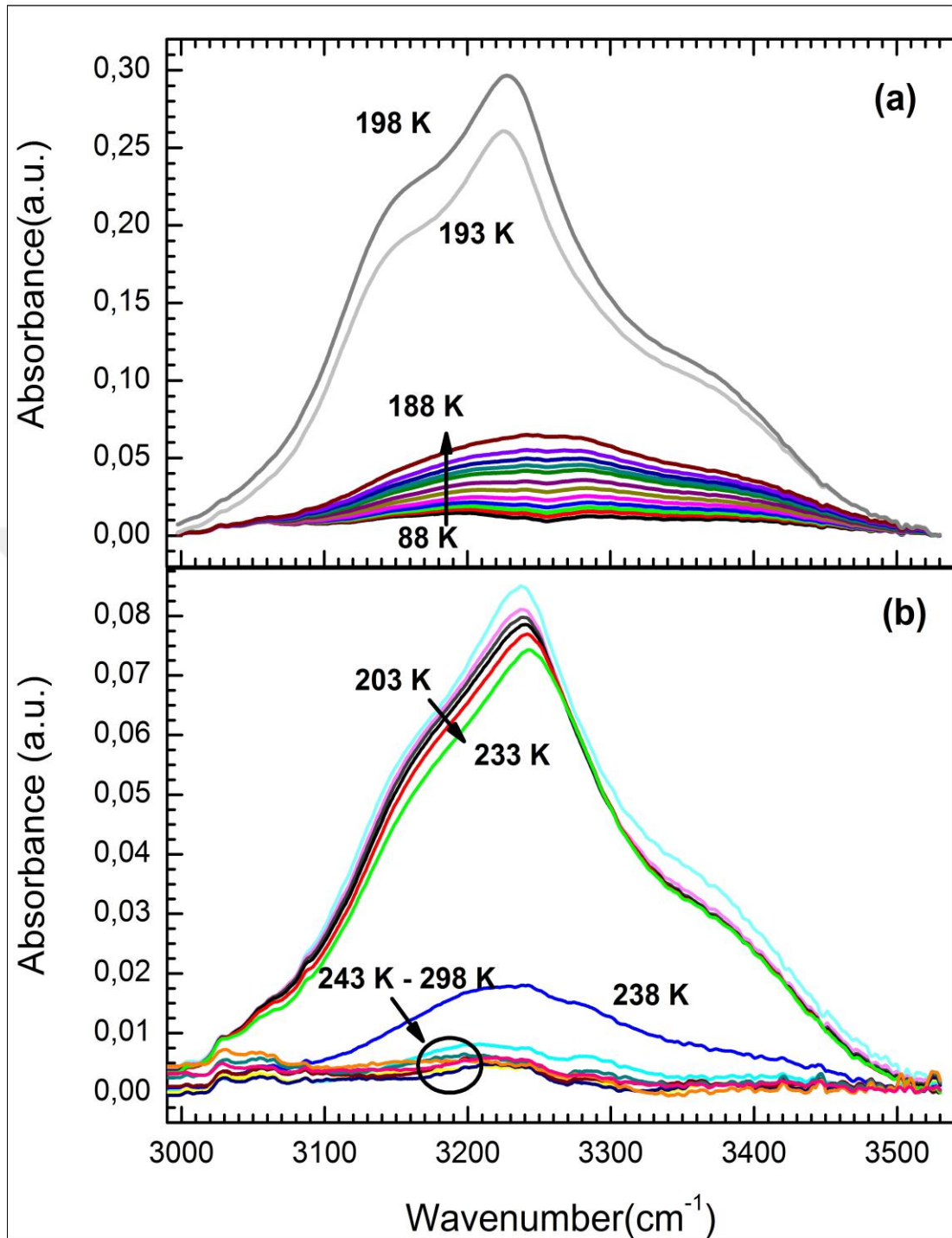
Figure 5.4 : FTIR spectra of OH-Stretching modes of water confined in FF nanotube measured at different temperature. Spectra below(a) and (b) above(b) the phase transition in the vicinity of 195K are seperated. Direction of arrows show the absorbance intensity change with increasing temperature.

Spectral range of observed confined OH-Stretching band observed in smaller wavelengths when compared with bulk water spectra obtained in works of other researchers [104, 130]. This is a consequence of different confromations adopted by nanoconfined water molecules. It has to be noted that the phase transition in 1nm

confined water molecules FTIR spectra around 195 K is first compared with other works on nanoconfined water [97, 131, 132].

To gather information about contributions of individual OH-Stetching modes, a deconvolution of gaussian modes is applied on spectra in Figure 5.3.

5.4.1.2 Deconvolution of OH-stretching band into Gaussian modes

The broad OH-Stretching band of confined water in FF peptide nanostructures consists of seven distinct vibrational modes which we have described in section 5.4.1.1. Every mode is defined by a Gaussian distribution to investigate their physical properties which are dynamically changing with temperature.

Mode IV which is located about 3240 cm^{-1} (Figure 5.3), doesn't exhibit temperature dependence throught out the range, thus it is related with peptide backbone. We define it as NH stretching mode which is obviously exists in the diphenylalanine nanostructure.

Starting from the lowest temperature, 88 K (Figure 5.5), a sharp local minimum splits the spectrum into two distinct envelops. This observation is in line with Skinner's calculation for water molecules in strong coupling environment, where low energy flank absorbance increases and a split about 3250 cm^{-1} occurs [2010]. The low energy envelope consists of three modes; I, II and III which possess coordination numbers equal or close to 4. In other words, these vibrational modes belong to completed tetrahedral water clusters confide inside FF peptide hexamers. The high energy envelope consists of two remaining modes; V and VI which are relatively movable than the modes in the first envelope. Mode V corresponds two 'intermediate' water whose coordination numbers are two and three. Mode VI, which possesses the highest energy is related to the water molecules located inside the larger volume between neighbouring peptide hexamers. Thus, their dynamical constraints are similar closer to free water. Between this two envelops a phase different is obvious.
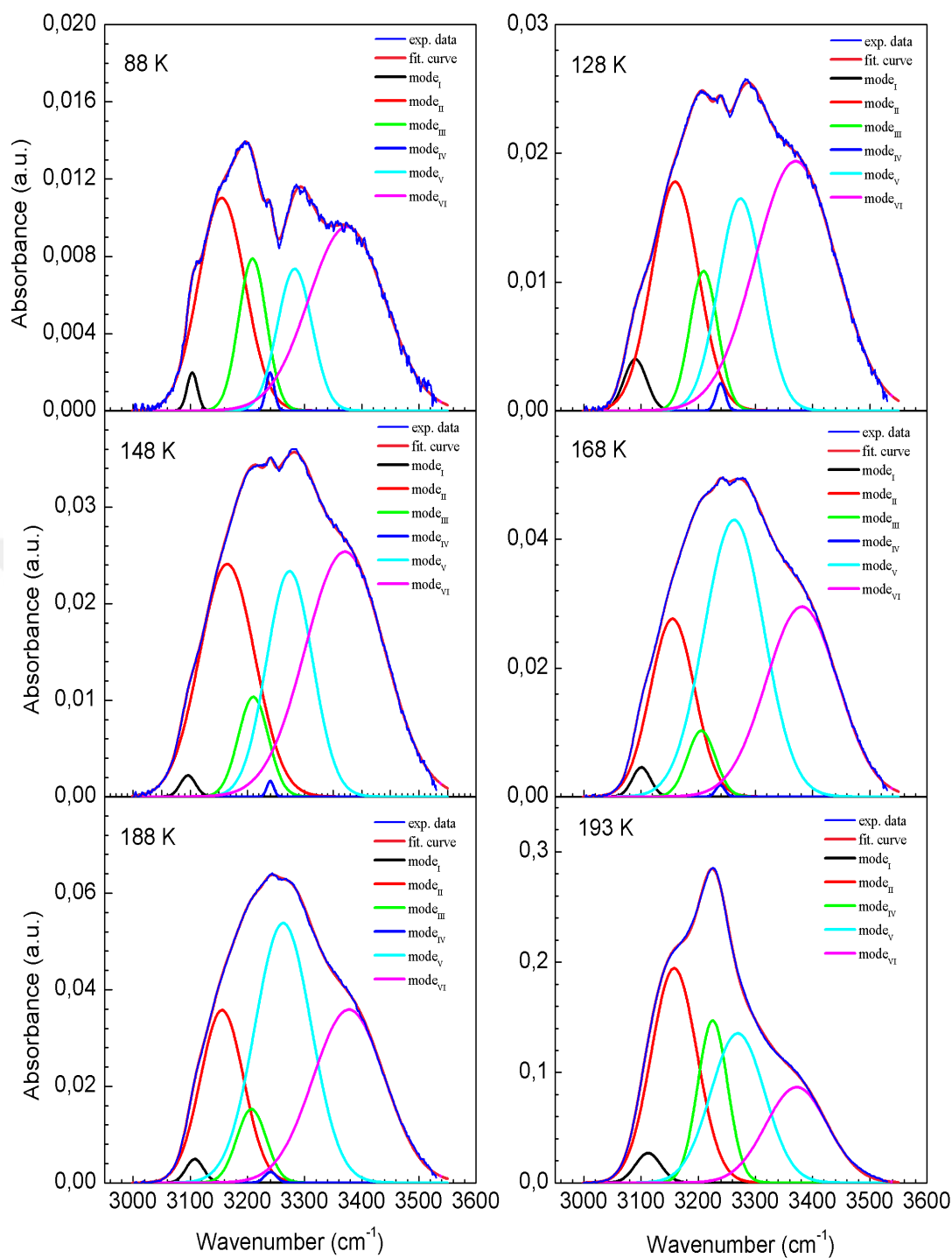
Figure 5.5 : Deconvolution of OH-Stretching band in selected temperatures between 88K to 193 K.

With increasing temperature, starting from 128K the split in the spectrum disappears in the vicinity of 168K. It is notable that the increase faster in mode V's intensity is responsible this dynamic. This temperature also coincides with the dielectric measurements which is the onset of thawing of water molecules as described in

Chapter 4. Interchange of H-Bonds between water clusters in different confinements gives rise to establishment of long range interactions.

Above described dynamic continues until 193 K when the dramatic rise in the intensity of peak of the infrared spectrum occurs, from about 0.06 a.u. to 0.3 a.u. This is a clear phase transition, which corresponds to the peak at dielectric spectrum at the same temperature. This mutual phenomenon is a direct evidence of change in dipol moment of water confined in peptide nanostructure.

After the phase transition, T > 193 K, the unified envelope is dominated by tetrahedral water network. Furthermore, the location of the peak, 3250 cm^{-1} coincides with tetrahedral water's peak in infrared spectrum [133].

In Figure 5.6, FTIR spectra of selected temperatures in range 233 K – 298 K are shown. When the OH-Spectrum at 233 K is compared with the spectrum at 193 K from Figure 5.5, tetrahedral network maintains itself since we notice that band featured are mostly preserved with the peak position around 3250 cm^{-1}, but there is a decrease in intensity from 0.3 a.u. to 0.08 a.u.
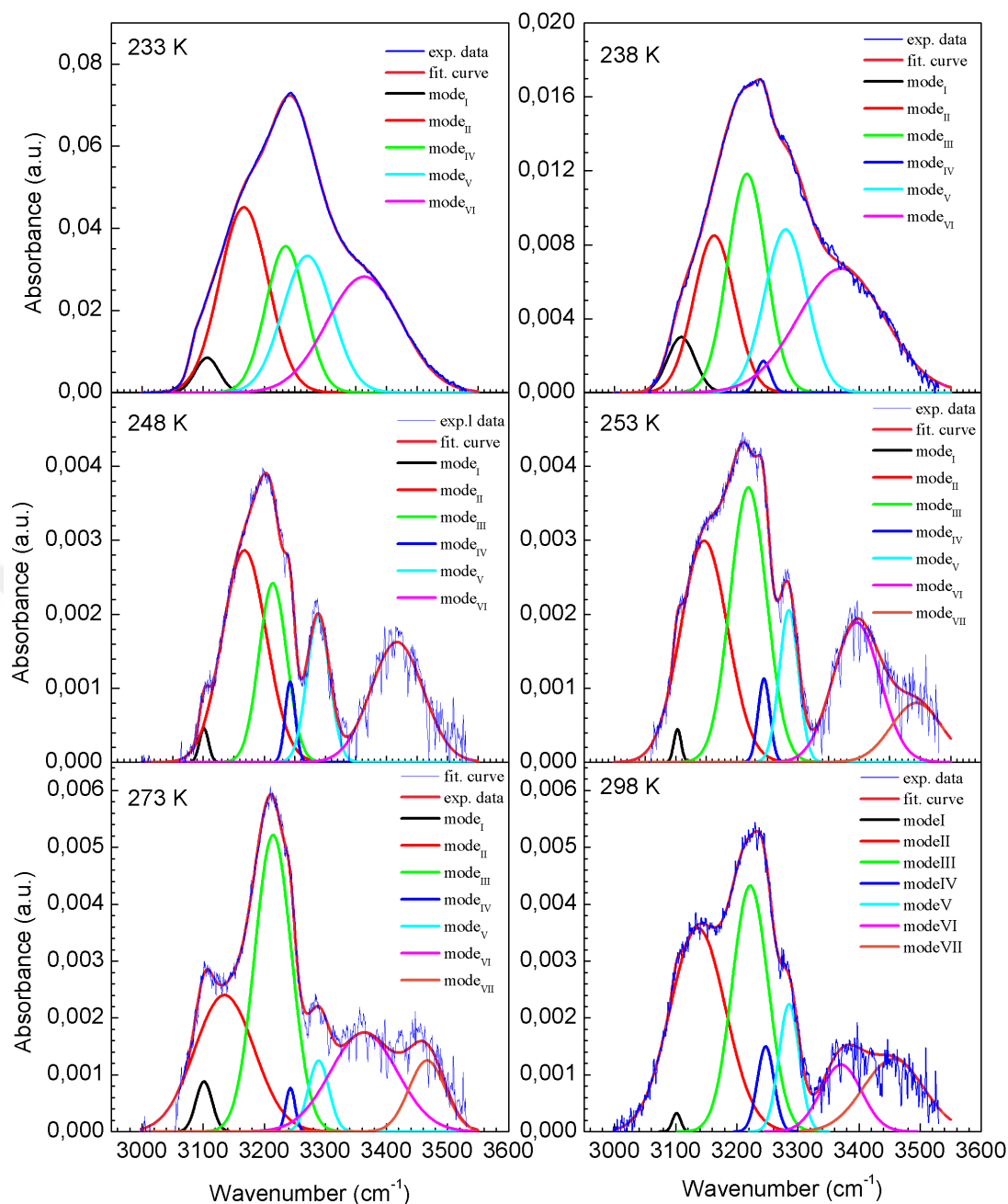
Figure 5.6 : Figure 5.5 Deconvolution of OH-Stretching band in selected temperatures between 233K to 298 K.

In th next spectrum at 238 K, intensity decreases dramatically (Figure 5.6). The OH-stretching band features are starting to be distorted. Decrease in intensity and visible band shape distortion continues until in spectrum at 248K, the envelop is seperated again into two distinct regions. Furthermore, at 253K a high frequency Gaussian mode VII appears around 3500 cm^{-1}. Mode VII resembles the non hydrogen-bonded water molecules following the Brubach's classification [103]. This phenomenon can easily be explained by exhaustion of H-Bonded water molecule network. In this temperature

range between 248 K and 298 K, the long range interaction interactions are lost and short range interactions governs the nanoconfined water dynamics. Fluctuations in the absorbance and OH-stretching band shape can be attributed to the loss of order of water molecules confined water FF NT/MT.

5.4.1.3 Temperature Dependence of Fundamental Characteristics of FTIR spectra

From section 5.1 one can notice that the intensity of the infrared absorbance; $I \sim (\frac{\partial \mu}{\partial Q})^2$. Consequently, dynamics of dipole moments in the system can be obtained from the temperature dependence of intensity of individual Gaussian modes. Since each Gaussian modes are related to a specific confinement in peptide nanotube, FTIR spectra allow to analyze evalution of dipole moments with temperature of confined water molecules.
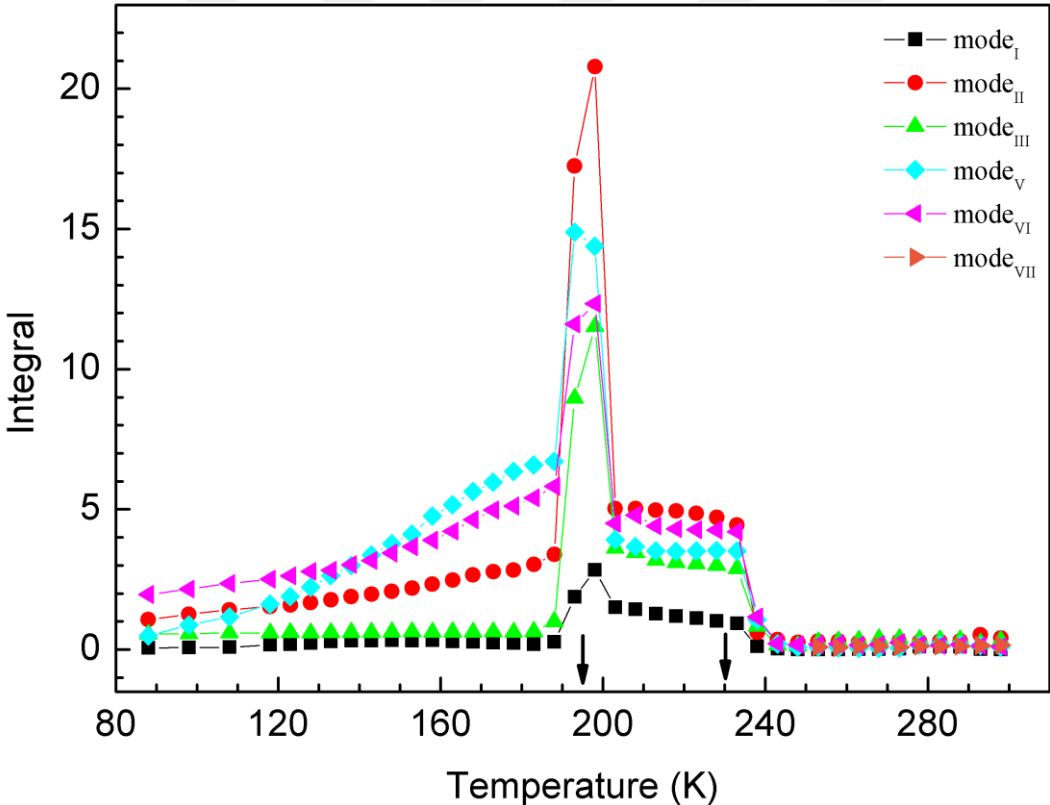
Figure 5.7 : Temperature dependence of characteristic integrals of each Gaussian mode of OH-Spectra of FF peptide nanotubes. Black arrows indicate the phase transition of confined water according to dielectric permittivity data.

From the Figure 5.5 and 5.6, one can notice that the observed absorbance bands have different halfwidth values. It means that oscillator distributions in each band cover an appropriate frequency range which gives contributions resultant absorbance. Integral

of each bands cover the total number of oscillators in appropriated absorption mode, consequently number of population of related absorption mode (Figure 5.7).

At low temperatures, beginning approximately from 90 K, population of modes II, V and VI are monotonically increasing, signifying the establishment of H-Bonds between the water molecules between and beyond the hexagonal ring but modes I and III show no temperature dependence until T=190K (Figure 5.7).. At T=190 K, all OH-Stretching modes demonstrate a jump in absorbance spectra. It has to be noted that mode IV, has no temperature dependance at all, thus it is accepted to be a structural mode related with the peptide backbone, namely NH Stretching bond which remains unaffected by the phase transition. After the jump, OH-Stretching modes proceed on a plateau, until the obvious decline around 230 K.

By the dielectric spectroscopy measurement, it was shown that in the vicinity of 195 K, thawing of water molecules confined in FF ring takes place. It means that in FTIR spectra, it is expected that population of OH-stretching modes increase due to dipole orientation along c-axis of FF peptide nanocavity. It is known that, inside hexagonal FF ring water molecules are connected with NH_3^+ and COO^- charged groups located at FF nanocavity surface. Mod II is related to water molecules connected to amino group, whereas mod III is related to water molecule connected to COO^-. It is neccesary to notice that mod III, which is related to completed tetrahedral configuration. This mod preserves its population level from the lowest temperature until the phase transition about 195 K. Whereas, mod II monotonically increases towards the phase transition at 195 K. Mods V an VI also exhibit an increase with temperature towards 195K. It means that H-Bond network evolves between movable water molecules and water confined in FF rings. Above the phase transition at 195 K, intensities of mods II, III, V and VI proceed on the same level until drastical drop at 235 K. This temperature is same with temperature related to dielectric peak which previously observed at 230 K (see Chapter 4). Reminding the observation that OH-stretching band envelope is similar to tetrahedral water between 193 K to 238 K (Figure 5.5, 5.6), this phenomenon is a result of persistent long-ranged tetrahedral water network in entire FF NT/MT system between these temperatures. From deconvolution in Figure 5.5, it is clearly seen that level of stretching is minimized after 235 K, but characteristic OH-stretching mods remain.
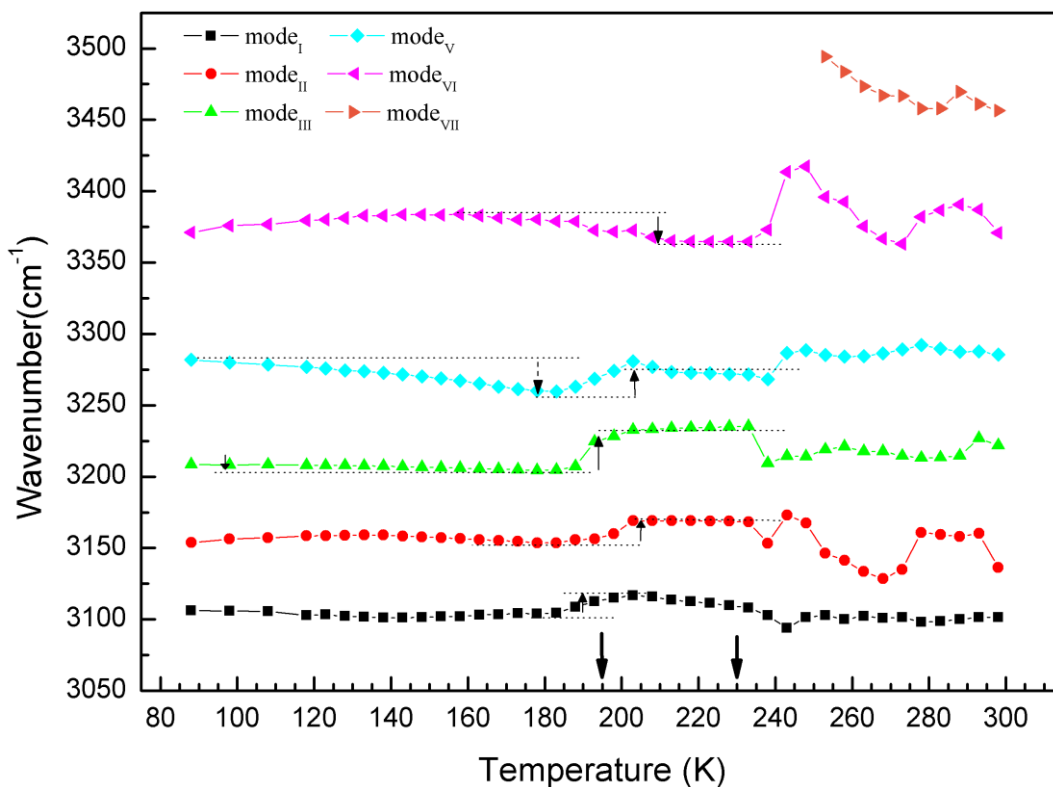
Figure 5.8 : Temperature dependent wavenumbers of deconvoluted OH-stretching modes. Fat, black arrows indicates phase transitions obtained by dielectric measurements. Thin-black arrows indicate redshift, facing upwards and blueshift facing downwards.

Beginning from 88 K, redshifts in different value in wavenumbers of all OH-Stretching modes are observed, besides mode VI. At first, mode VI exhibits blueshift and then redshift as temperature approaches to 195 K. The crossover from blueshift to redshift occurs in the temperature region 130 K - 140 K. This crossover exhibits slow kinetics with temperature due to diffusivity of H-bonding processes in this group water molecules. Whereas in the mode V, H-Bond connectivity demonstrates a faster processes starting from lowest temperature. From Figure 5.8, one can notice that the redshift towards the phase transition at 195 K is pronounced as $\Delta k = 20$ cm^{-1}. The mods II and I undergo comperatevely weaker redshifts, approximately $\Delta k = 4$ cm^{-1}, since these group of molecules are located in severe confinements in the hexagonal FF ring. The mode III, is related to completed tetrahedral configuration with coordination number equal to 4, consequently it demonstrates the lowest value of redshift until the phase transition at 195 K.

At the phase transition in the vicinity of 195 K, modes I, II, III and V exhibit a collective blueshift. Maximum of blueshift, approximately $\Delta k = 30$ cm^{-1}, was found

72

for tetrahedrally configurated water molecules, namely mode III. Collective blueshifts of these modes coincide with infrared absorption peak of appropriated water configurations (Figure 5.9). Increasing in OH-stretching vibration energies indicates that water molecules are alligned in the confinement dictated by peptide hexagonal rings. Only mode VI continues redshift in the region of 195 K to 230 K as noted above, that these mode is related to water molecules with coordination number less than 4. Continuous redshift indicates ongoing H-Bond connectivity process in water molecules located between the peptide hexamers during this phase.

At temperatures above water structural phase transition at 230 K, fluctuation of wavenumbers in all OH-stretching modes have been observed in Figure 5.8. However mode III and V exhibit stable tetrahedral water character. Different values of wavenumbers of mode III and V indicate the existence of two group of tetrahedral water molecules. These are water moleuces with complete tetrahedral configuration with coordination number equal to four (mode III) and non completed tetrahedral configuration in less severe confinement (mode IV). Wavenumber of mode VI exhibits a relatively high but fluctuated value at temperatures above 230 K. This strong fluctuation is due to occurrence of an additional mode VII, above 260 K,with the lowest coordination number in the FF NT/MT system. This observation is in line with dielectric data, where strong reorientation of water dipoles giving contribution to real dielectric constant at T>230 K.
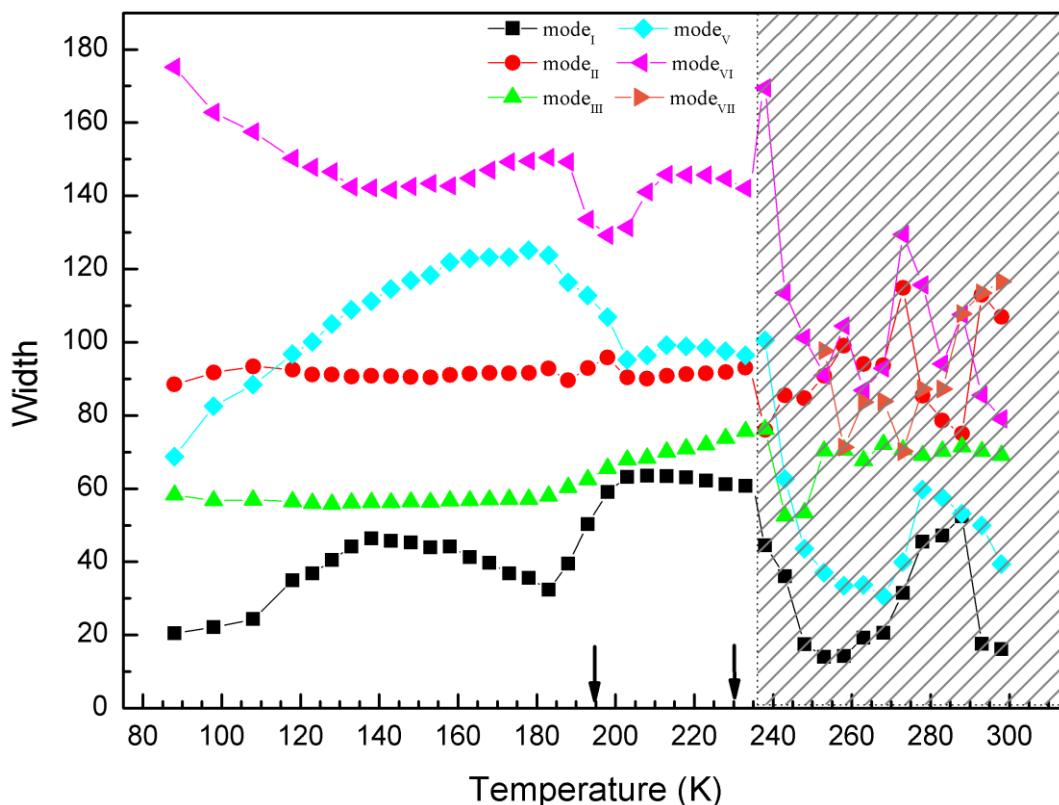
Figure 5.9 : Temperature dependence of halfwidths of OH-stretching Gaussian modes related to confined water in FF NT/MT. Black arrows indicate phase transitiion temperatures obtained by dielectric measurements.

In the low temperature range (88 K -199 K), mode III related to tetrahedral water and mode II, connected with confined in the ring exhibit stable exhibit stable halfwidth (HW) as seen in Figure 5.9. Evolution of these modes evoluate without any mimic of interactions with neighbouring modes. Already defined interactions with charged groups in FF rings is the reason of the stability in their HW values. Whereas, mode I and V gradually increase their HW beginning from low temperatures. Increasing HW values of modes I and V reflect delocalisation of OH-Stretching modes as a result of increasing dipole-dipole interactions. In the low temperature range (88 K -199 K), mode VI, first decrease and then increase its HW value. Peak of HW values belonging to mode V and VI coincides, which indicates interactions of water molecules with complete and noncompleted H-Bond.

In the phase of long-ranged dipole order between temperatures, 190 K to 230 K, HW's of modes are mostly stable. However, above 230 K, when long-range order is frustrated, strong fluctuations of halfwidths are observed, except mode III. Strong fluctuations are caused by the liquid phase with short-range order of water molecules, which permits rotational and translational motions. On the other hand, at room temperature, there are multiple positions in which mobile water molecules can be confined. Occurrence of a new absorption mode related to mobile water (mode VII) indicate that in FF NT/MT with temperature water molecules with low coordination number appears. This group of water is mobile water. Consequently, number of oscillators covered by each Gaussian mode will not be constant and changes with activation temperature. The same phenomenon is observed in all samples measured. Observation of endothermic regime in these temperatures confirms the shortening of water molecule chains.

5.4.2. Influence of phase transitions on the diphenylalanine deptide lattice

In the FTIR spectra of FF NT/MT, infrared active absorbtion band between 2820 cm^{-1} and 2980 cm^{-1} is observed (Figure 5.10). This absorbtion band belongs to CH-Stretching modes according to literature [134]. Diphenylalanine molecules contain covalent CH bonds forming self-assembled FF peptide backbone as seen from inset in Figure 5.11.
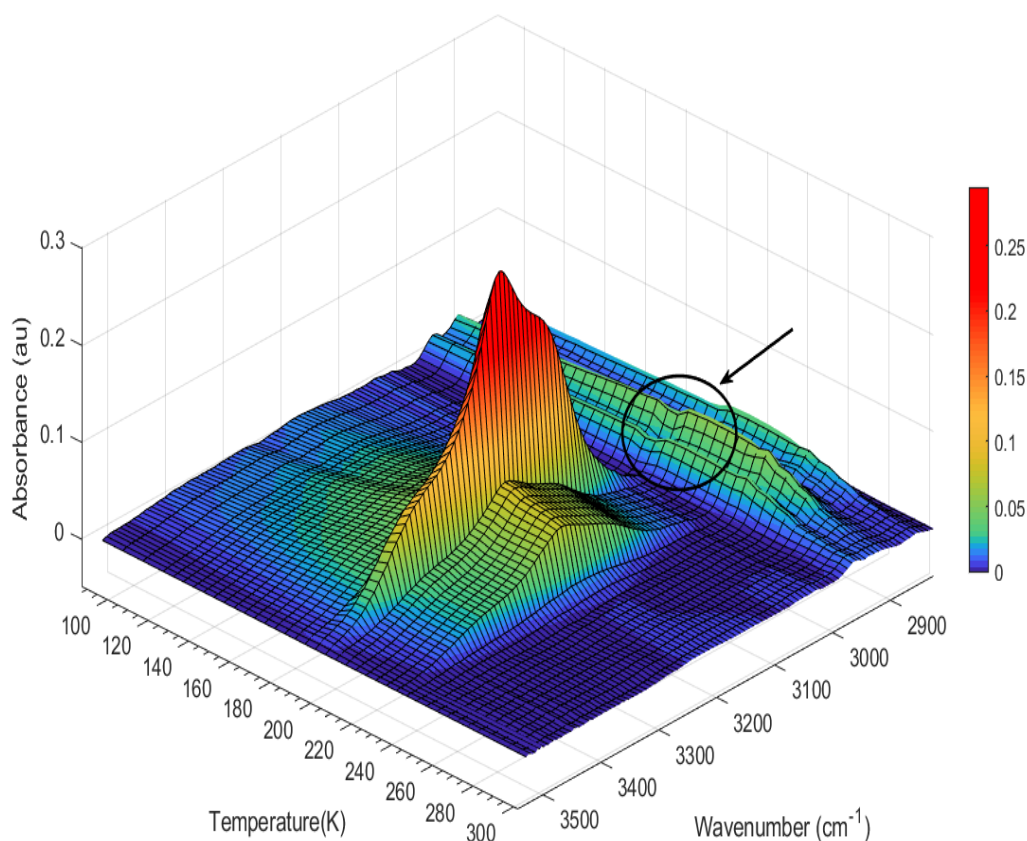
Figure 5.10 : 3D plot of OH-Stretching band shown with CH-Stretching band.

From Figur 5.10, one can notice the phase transition at 195 K related to dipole order as a result of thawing of confined water in FF NT/MT. Also, one can notice, that absorbance of CH-Stretching band undergo an anomaly strictly at this temperature range. From this observation, we can clearly argue, that conformational change of water dipole affects the peptide lattice. Also, one can notice that anomaly on CH-stretching band at 195 K is remarkably weaker than the anomaly of OH-stretching band. While no change was observed in wavenumbers in wide temperatures range even at phase transitions, integral area of CH-modes exhibit an apperant anomaly at 195 K as clearly seen from Figure 5.11. Populations of all CH-stretching modes monotically increase from 88 K to 195 K. This behavior is probably connected with thermal expansion of peptide lattice. Similar phenomenon was observed in Ref [135]. At phase transition around 195 K, there is no peak but a downwards kink in CH-stretching band. At T>195, CH-stretching with wavenumber 2920 cm^{-1} further increases its population, whereas other two CH-stretching modes with wavenumber 2850 cm^{-1} and 2955 cm^{-1} displays equal population levels.
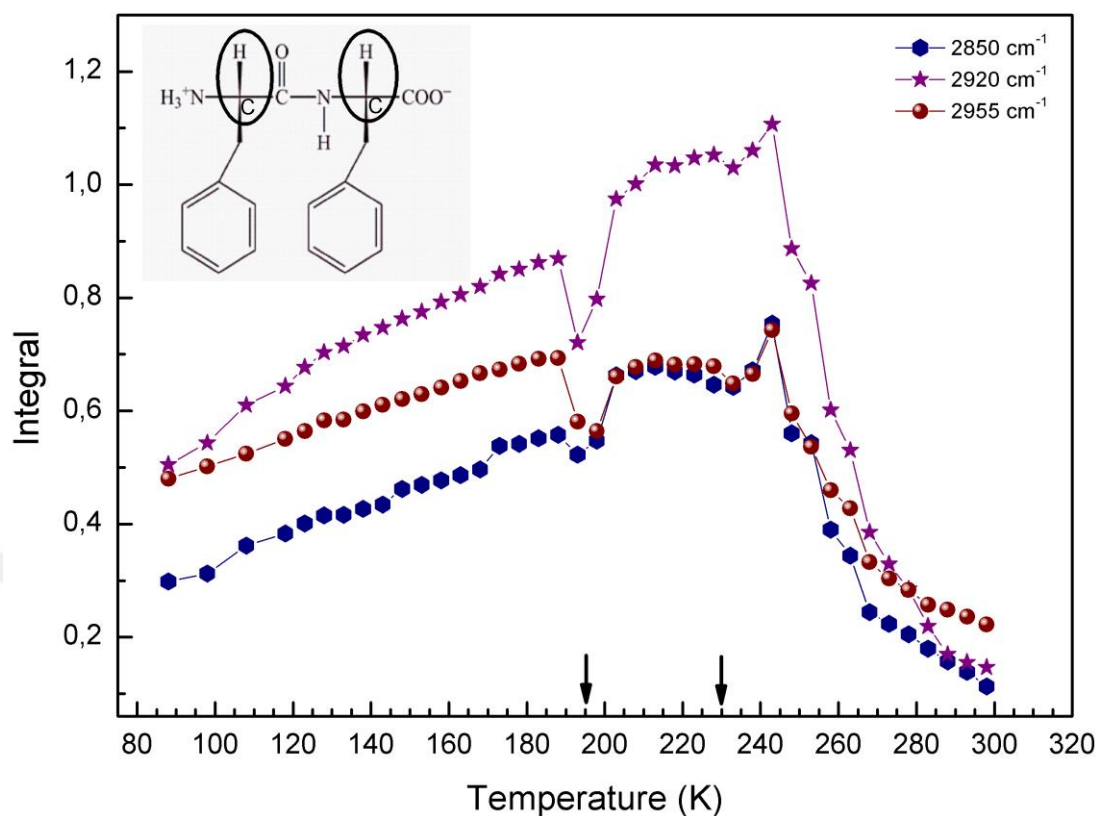
Figure 5.11 : Temperature dependent populations of CH-Stretching modes in FF NT/MT. Inset shows shematical representation of diphenyalanine molecule. Black circles indicate covalent CH bonds [5]. Black arrows indicate phase transitions according to dielectric measurement.

Observed peak is approximately 15 K higher than the structural transition temperature of water molecules at 230 K. From this result we can conclude that loss of dipole ordering just slightly influences CH-stretching modes. Temperature of the observed peak around 245 K coincides with the maximum of isothermal compressiblity [136] obtained for water. However, our result shows that decreasing CH-stretching population with melting of water molecules in FF NT/MT matrix.

5.4.3. FTIR spectroscopy of OH-Bending modes of confined water in FF NT/MT

In FF NT/MT system, beside OH-stretching vibrations nanoconfined water molecules feature also OH-Bending vibrations. OH-Bending vibrations emerge when the angle between O and H atoms oscillate
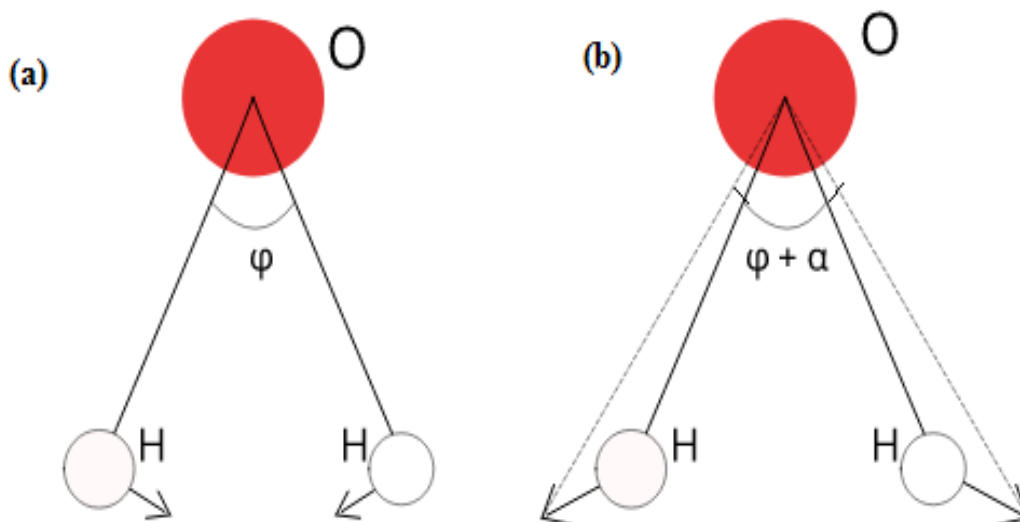
Figure 5.12 : (a) OH-Bending vibrations in H_2O; (b) OH-Bending modes superposed with the OH-Stretching vibrations in H_2O molecule

Only bending modes are shown in Figure 5.12a and superposition of stretching and bending modes are shown in Figure 5.12b. Depending on the different confinements OH-Bending modes are expected in peptide nanotubes. OH-bending modes of confined water molecules are measured between 1460 cm^{-1} and 1700 cm^{-1} as shown in Figure 5.13. Deconvolutions of refered vibration band in FTIR spectrum is given for 93 K and 298 K. Modes are divided in to main groups of Gaussians denoted by I, II, III, IV and V. In wide temperature range from 93 K to 298, there is no remakable change in absorption intensity.
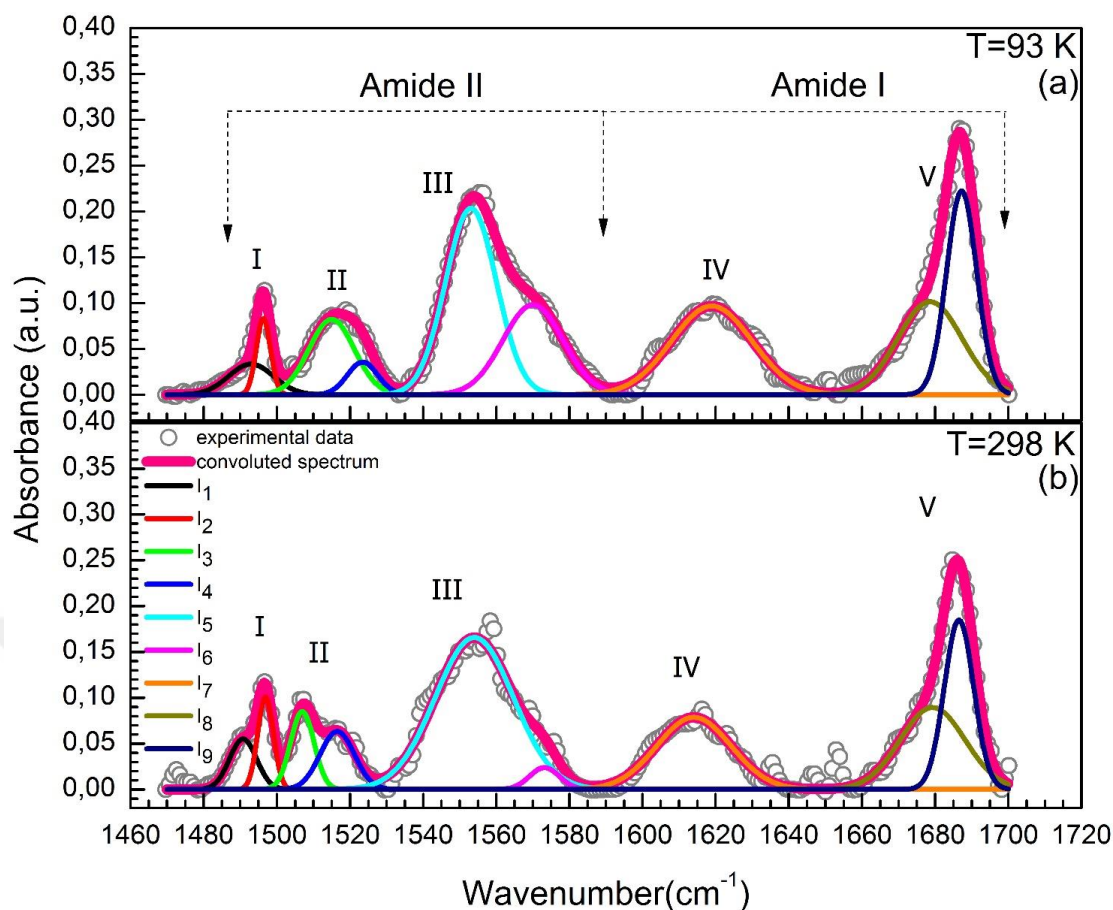
Figure 5.13 : Amide I, Amide II and accompanying H_2O bending modes at 93 K (a) and 298 K (b)

FTIR spectra of peptide nanotubes in the range 1460 cm^{-1} and 1700 cm^{-1} presented in this work highly complicated compared with the literature [137, 138]. Superposition of Amide I and Amide II bands with OH-Bending modes is the reason of observed spectral complexity. Amide I band arises from the stretching of (C=O) carbonyl bonds and displays itself as absorbtion modes denoted by IV and V between 1600 cm^{-1} and 1700 cm^{-1} [139]. Amide II band is a combination of (C-N) stretching and (N-H) bending which reveal themselves between 1460 cm^{-1} and 1600 cm^{-1} as infrared absorbtion modes [138]. Mentioned chemical groups belong to peptide backbone, therefore we have to pay attenition to H_2O molecules H-bonded to COO^- and NH_3^+ groups symmetrically distributed in FF hexagonal rings. Thus, it is expected that Amide I and II bands display complexity.

Main absorption groups I, II, III and V are convoluted into Gaussian modes in spectral range from 1460 cm^{-1} to 1700 cm^{-1} (Figure 5.13 a,b). Functional groups on the FF peptide hexamer, (C=O), (N-H) and (CN) are more stable thus appropriate Gaussian

modes are expected to be narrow and sharp [139]. All groups except IV are combination of two modes. Gaussian modes with lower absorbances belong to OH-Bending vibrations of confined water in FF NT/MT. According to this reasoning, vibrational modes in this spectral region are classified as follows; I_9 – Amide I (C=O) carbonyl stretching mode; I_8-OH-Bending mode of water molecules H-bonded to carbonyl groups (C=O); I_7 – OH-Bending mode of tetrahedral water; I_6 - OH-Bending mode of water molecules H-bonded to (NH) Group; I_5 – Amide II (N-H) bending mode; I_4 - Combined band of Amide II (N-H) bending ve (C-N) stretching modes; I_3 - OH-Bending mode of H_2O correlated with I_4; I_1, I_2 – (C-N) vibration modes in different locations.
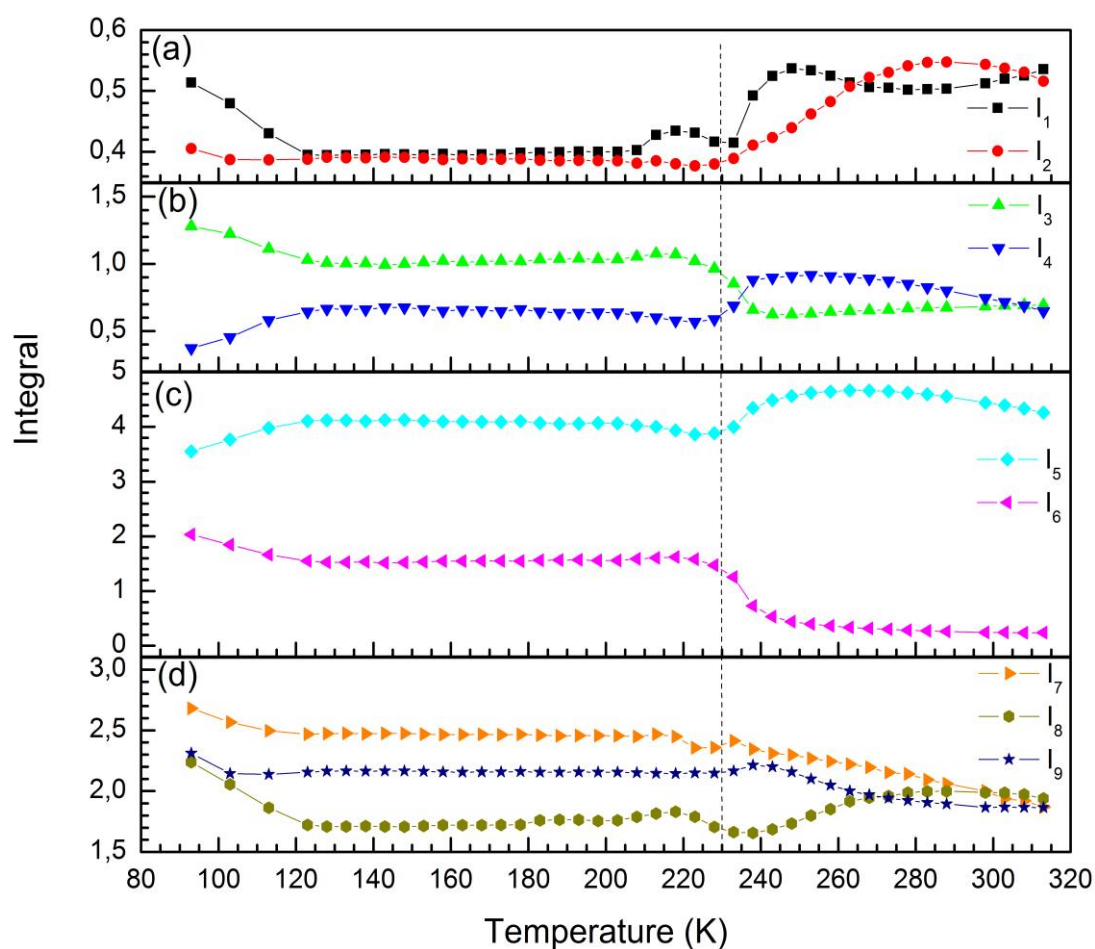
Figure 5.14 : Temperature dependence of the integrated area under vibrational modes in spectral range beween 1460 cm^{-1} and 1700 cm^{-1}. Main groups are seperated into figures respectively; I(a), II(b), III(c), IV and V(d). Dashed line is drawn according to the dielectric spectroscopy results and denotes the phase transition temperature at 230K.

Integrated areas under modes I_{1-9} are shown in Figure 5.14. Vibrational modes are seperated into groups for simplification. General observations from temperature dependence of integrated areas under Gaussian modes are as follows;

In temperature range from 80 K to 110 K, all Gaussion modes exhibit changes. This phenomenon points out an unknown phase transition. In temperature range from 110 K and 230 K, all vibrational modes proceed in stable lines. There is no sign of phase transition which dramatically effects OH-stretching vibrations at 195 K. Here we can argue that only the OH-stretching modes are responsible from the H_2O dipol order established in temperature range 195 K- 230 K.

All vibrational modes exhibit apperant changes starting from the phase transition at 230 K.

In Figure 10a, populations of I_1 and I_2 increases slightly between 0.4 to 0.5 a.u. at T>230 K. It is known that C-N vibrations are not connected with H_2O.

In Figure 10b,c, integrated areas under I_3 and I_6 gradually decrease, whereas I_4 and I_5 exhibit a gradual increase at T>230K. We revealed in previous chapters that long-range dipole order of water molecules are exhausted in this temperature range. Thus it is expected that the excited populations of OH-Bending modes, namely I_3 and I_4, decrease. Quaselasticity constants of OH-Bending decrease with increasing temperature in T>230 K. In spite of this observation, vibrational modes in Amide II group, I_4 and I_5 increase their excited populations with increasing temperature in the same temperature range.

In Figure 10d, temperature dependent integrated areas under carbonyl (C=O) stretching mode in Amide I group and bending modes of H_2O molecules H-Bonded to carbonyl group, I_7 and I_8 are shown. Wavenumbers of water bending related with the tetrahedral H_2O configuration modes are respectively $k_7 = 1620cm^{-1}$ and $k_8 = 1680cm^{-1}$. Similar values are found for water confined in cytoplasmic proteins as 1631 cm^{-1} and 1671 cm^{-1} [131]. It is remarkable that the populations of I_9, I_8 and reach to the same value when temperature increases to 320K. Carbonyl in amide I group is H-Bonded to water molecule in such a motif, C-O…H, so that OH-bending and CH-stretching modes are closely related [129, 5]. Consequently, populations of I_7, I_8 and I_9 focus on the same value. This observation helps to understand vanishing dielectric relaxation processes in dielectric spectroscopy around 320 K. Around 320 K, lifetime of H-Bonds

become too short, in picoseconds [136]. Dipole relaxations in picoseconds are too short to contribute to dielectric polarisations, but in FTIR they demonstrate as seen in Figure 5.14d.

6. SUMMARY OF FINDINGS

In Chapters 4 and 5, obtained results from BDS, DSC and FTIR measurements are broadly discussed. For clarity, we will briefly summarise findings in relation with the questions related to the present work.

The main objective of the thesis was to determine the properties of confined water in FF NT/MT to reveal the origins of functionalities peptide nanostructures.

In BDS study, we have revealed succesive phase transitions at 195 K, 230 K and 415 K, related with the confined water in FF NT/MT. First phase transition at 195 K is related to the onset of long-range tetrahedral network between all water clusters residing the peptide nanotubes. Although, similar temperatures were defined by many authors as glass transition temperature [101] or fragile-to-strong transition [116], our DSC results show no sign of either phenomena. At 195 K, an absorbance peak in all OH-stretching band especially related with tetrahredral water was observed in FTIR spectroscopy, indicating the onset of long-range tetrahedral order of confined water molecules in peptide nanotubes.

The second phase transition at 230 K is the transition from long-range tetrahedral order to short-ranged order, therefore a structural phase transition. Singularity in DSC signal confirms this observation. The region of this particular temperature has long been debated to contain FSC related to Widom line [88, 90, 93, 97, 98]. Nevertheless, we observed no crossover in relaxation times, only a distinct dielectric peak at 230 K. Furthermore, all OH-stretching modes in FTIR spectra related to confined water vanished above 230 K. The high temperaure transition at 415 K, emerges as an irreversible change in the peptide structure, which leads to the loss of water, therefore the stability and functionality of FF NT/MT is deprived through this phase transition [35].

Dielectric loss spectroscopy in broad temperature range (100 K – 450 K) has revealed 4 distinct relaxation processes of nanoconfined water in FF NT/MT. Below the structural phase transition there are two accompanying processes with 4 decimal difference in relaxation rate. Fast process is related to the relatively free water

molecules spaning throughout the nanotube cavity; water molecules H-bonded to carboxyl and protonated amino groups exhibit the slow process. A similar heterogenity appears in FTIR spectra of FF NT/MT, where OH-Band is splitted into two distinct envelopes. The low frequency flank of the envelope indicates strong coupled water molecules with the peptide backbone, whereas water clusters away from the hydrophilic inner walls have higher frequencies [104]. This heterogenity reflects the complex structure of FF NT/MT system and it is the source of observed dynamics. With increasing temperature both processes demonstrate coupled crossovers. Thawing of water molecules bound to carboxylate at T = 162 K coincides with αβ-crossover in process I related to relatively 'free' water. Second stage of the coupling is at about T = 195 K, water molecules bound to amino groups joined to the tetrahedral network, thus the long-range order is completed.

In FTIR, we observe a related phenomenon as establishment of H-Bonds between OH-stretching modes. Wavenumbers of modes belong to tetrahedral water demonstrates redshifts when temperatures increases from 88 K to 195, except a blueshift in the vibration of relatively free water clusters between the rings. The split between dissapered at 195 K and band shape remained same as fully tetrahedral water until 230 K. It is remarkable that, all OH-stretching modes have similar intensities in this temperature range. A similar phenomenon was observed in literature but only for a single temperature which was attributed to the FSC [97]. In our experiments no indication of FSC or Widom line can be made. Furthermore, the intensity of the OH-stretching absorption abrubdtly increased indicating a phase transition. This clear phase transition is observed first time in the literature.

At 230 K, a discontinuity emerges in process II and becomes a slower process III, due to high entropy caused by H-bond defects. An additional, process IV appeared in this temperature range with non-monotonic temperature dependence. The latter process is related with the water clusters between FF hexagonal rings. The same phase transition appeared as the loss of infrared absorption spectra of confined water in FF NT/MT. A new mode appeared in the high frequency flank, indicating the loss of tetrahedral order. This new mod is defined as non-hydrogen bonded OH-mode in other works [104, 131]. Thermal fluctuations reign in this temperature range. Due to increased thermal fluctuations, orientational motions of 'free' water molecules contriubtes to the

net dipole moment and high dielectric constant in the vicinity of room temperature is observed. Consequently, the peak of the dielectric permittivity at 320 K emerged.

Two glass transitions for two distinct phases are revealed, depsite previous results indicating no glass transition in 1nm confinement [93]. First one is T_{g1} = 133 K, which is close to the glass transition of bulk water [114]; the second one is T_{g2} = 205 K which is distinct from the bulk but close values are suggested for confined water [100, 101]. Consequently, we argue that water inside FF NT/MT demonstrates both bulk and confined water characteristics. This is a decisive evidence of connections between porous structures in FF NT/MT allowing bulk water characteristics. By interpolating relaxation times to 10^2 s, we have obtained freezing temperatures T_{f1} = 162.8 K and T_{f2} = 179 K indicating the thawing of solvation shells.

In FTIR measurements, we succesfully investigated OH-stretching, OH-bending regions together with peptide backbone related CH-stretching and Amide I, II bands. Interplay of the OH-Bending modes with the Amide modes reveals the coupling of peptides dynamics with confined water. Above 230 K, when the tetrahedral order of water network is lost the effect of H-bonding on Amide bands is removed. Consequently, we were able to obtain reliable information about the thermal behavior of the peptide backbone. Vibrations of CH-stretching band which belongs to peptide nanotubes, are succesfully observed through the measurement. Intensities are on monotincal increament until 245 K, with a downward kink at about 195 K. This demonstrates the coupling of peptide nanostucture with the confined water. An intrpration of this phenomenon is as follows: Monotonical increase in CH-stretching is probably related with the thermal expansion of peptide backbone. After the kink the increasing slows down demonstrating that established long-range interactions stiffened the backbone. Above 245, abrubdt decrease in CH-stretching intensities are following the trend isothermal compressiblity of water [138] reflecting the stretching relief in the peptide backbone.

7. CONCLUSION

This thesis is the first to state that the functional properties of diphenylalanine peptide nanotube/microtubes such as second harmonic generation, piezoelectricity, pyroelectricity and electrooptical effects are caused by collective response of water dipoles in FF NT/MT to external electric field not to ferroelectricity of peptide backbone. It was found, that dehydrated peptide nanotubes do not exhibit observed anomalies.

Depending on the phase of confined water, two glass transitions of water molecules were found in FF NT/MT. BDS and FTIR measurements both confirm that order of water dipoles in tetrahedral configuration in peptide nanotubes. We have shown that tetrahedral order maintained by ordered positions of hydrogen bond donors and acceptor are responsible for the water dynamics in FF NT/MT.

FTIR measurements revealed that the source of dipole moment is the OH-stretching mode of water molecules in different positions confined in diphenylalanine hexagonal rings.

Our results demonstrate a clear disagreement with the liquid-liquid critical point hypothesis. Furthermore, the structural phase transition at 230 K does not exhibit properties of solid-liquid transition. On the contrary, it was found that the phase transition at 230 K in FF peptides is the transition from long-range tetrahedral order of water molecules into liquid phase at high temperatures.

REFERENCES

[1] **Good M. and Trepat X.** (2018). Living systems engineered, bottom does not explain top. *Nature, 563*, 188-18.

[2] **Tiruvannamalai-annamalai R., Armant D. and Matthew H.** (2014). A Glycosaminoglycan Based, Modular Tissue Scaffold System for Rapid Assembly of Perfusable, High Cell Density, Engineered Tissues. *PLoS ONE*, *9(*1*)*, e84287.

[3] **Ghadiri. M., Granja J., Milligan R., McRae D.E. and Kazanovich N.** (1993). Self-assembling organic nanotubes base on a cyclic peptide architecture. *Nature*, *366(*6453*)*, 324-327.

[4] **Cherny I. and Gazit E.** (2008). Amyloids: Not Only Pathological Agents but Also Ordered Nanomaterials, *Angewandte Chemie – International Edition, 47*(22) 4062-4069.

[5] **Görbitz C.** (2001). Nanotube formation by hydrophobic dipeptides. *Chemistry – A European Journal*, *7(*23*)*, 5153-5159.

[6] **Akdim B., Pachter R. and Nalk R.** (2015). Self-assembled peptide nanotubes as electronic materials: An evaluation from first-principles calculations. *Applied Physics Letters*, *106(*18*)*, 1-5.

[7] **Li Q., Jia Y., Dai L., Yang L and Li J.** (2015). Controlled rod nanostructured assembly of diphenylalanine and their optical waveguide properties. *ACS Nano*, *9*(3), 2689-2695.

[8] **Handelman A., Beker P. and Amdursky N., G.** (2012). Physics and engineering of peptide supramolecular nanostructures. *Physical Chemistry*, *14*(18), 6391-6408.

[9] **Azuri I., Adler-Abramovich L., Gazit E., Hod O. and Kronik L.** (2014). Why are diphenylalanine-based peptide nanostructures so rigid? Insights from first principles calcualations. *Journal of American Chemical Society*, *136*, 963.

[10] **Adler-Abramovich L., Reches M., Sedman V., Allen S., Tendler S. and Gazit E** (2006). Thermal and chemical stability of diphenylalanine peptide nanotubes: Implications for nanotechnological applications. *Langmuir*, *22(3)*, 1313-1320.

[11] **Bystrov V., Seyedhosseini E., Kopyl S., Bdikin I. and Kholkin A.** (2014). Piezoelectricity and ferroelectricity in biomaterials: Molecular modeling and piezoresponse force microscopy. *Journal of Applied Physics*, *116*, 066803

[12] **Kholkin A., Amdursky N., Bdikin I., Gazit E and Rosenman G.** (2010). Strong piezoelectricity in bioinspired peptide nanotubes. *ACS Nano*, *4(*2*)*, 610-614.

[13] **Khanra S., Ghosh K., Ferreira F., Alves V., Punzo F., Yu P. and Guha S.** (2017). Probing nonlinear optical coefficients in self-assembled peptide nanotubes. *Physical Chemistry Chemical Physics*, *19(4)*, 3084-3093.

[14] **Nguyen V., Zhu R., Jenkins K. and Yang R.** (2016). Self-assembly of diphenylalanine peptide with controlled polarization for power generation. *Nature Communications*, *7*, 1-6.

[15] **Lee J., Heo K., Schulz-Schönhagen K., Lee J., Desai M., Jin H. and Lee S.** (2018). Diphenylalanine peptide nanotube energy harvesters. *ACS Nano*, *12(8)*, 8138-8144.

[16] **Bystrov V., Kopyl S., Zelenovskiy P., Zhulyabina O., Salehli F., Ghermani N., Schur V. and Kholkin A.** (2018). Investigation of physical properties of diphenylalanine peptide nanotubes having different chiralities and embedded water molecules. *Ferroelectrics*, *525(1)*, 168-177.

[17] **Kim J., Han T., Kim Y., Park J., Choi J., Churcill D., Kim S. and Ihee H.** (2010). Role of water in directing diphenylalanine assembly into nanotubes and nanowires. *Advanced Materials*, *22(5)*, 583-587.

[18] **Andrade-Filho T., Ferreira F., Alves W. and Rocha A.** (2013). The effects of water molecules on the electronic and structural properties of peptide nanotubes. *Physical Chemistry Chemical Physics*, *15(20)*, 7555-7559.

[19] **Wang J., Liu K. Xing R. and Yan X.** (2016). Peptide self-assembly: thermodynamics and kinetics. *Chemical Society Reviews*, *45(20)*, 5589-5604.

[20] **Sjöström J., Swenson J., Bergman R. and Kittaka S.** (2008). Investigating hydration dependence of dynamics of confined water: Monolayer, hydration water and Maxwell-Wagner processes. *Journal of Chemical Physics*, *128(15)*, 0-9.

[21] **Elamin K., Björklund J, Nyhlen F., Yttergren M., Marttenson L. ve Swenson J.** (2014). Glass transition and relaxation dynamics of propylene glycol-water solutions confined in clay. *Journal of Chemical Physics*, *141*, 034505.

[22] **Cerveny S., F., Swenson J., Vogel M. and Xu L.** (2016). Confined water as a model of supercooled water. *Chemical Reviews*, *116(13)*, 7608-7625.

[23] **Heredia A., Bdikin I., Kopyl S., Mishina E. and Kholkin A.** (2016). Temperature-driven phase transformation in self-assembled diphenylalanine peptide nanotubes. *Journal of Physics D:Applied Physics*, *43*, 462001.

[24] **Ni Y. and Skinner J.** (2016). IR spectra of water in no man's land and the location of the liquid-liquid critical point. *Journal of Chemical Physics*, *145*, 124509.

[25] **Manka A., Pathak H., Tanimura S., Wölk J., Strey R. and Wyzlozil B.** (2012). Freezing in no-man's land. *Physical Chemistry Chemical Physics*, *14(13)*, 4505-4516.

[26] **Carny O. and Gazit E.** (2005). A model for the role of short self-assembled peptides in the very early stages of the origin of life. *FASEB Journal*, *19(9)*, 1051-1055.

[27] **Guo C., Luo Y. and Zhou R.** (2012). Probing the self-assembly mechanism of diphenylalanie-based peptide. *ACS Nano*, *6(5)*, 3907-3918.

[28] **Andrade-Filho T., Martins T., Ferreira F., Alves W. and Rocha A.** (2016). Water-driven stabilization of diphenylalanine nanotube structures. *Theoretical Chemistry Accounts*, *135(8)*, 1-8.

[29] **Reches M. and Gazit E.** (2003). Casting metal nanowires withing discrete self-assembled peptide nanotubes. *Science*, *300(5619)*, 625-627.

[30] **Reches M. and Gazit E** (2006). Controlled pattering of aligned self-assembled peptide nanotubes. *Nature Nanotechnology*, *1,* 195-200.

[31] **Amdursky N., Koren I. and Gazit E.** (2011). Adjustable photoluminescence of peptide nanotube coatings. *Journal of Nanoscience and Nanotechnology*, *11(*10*)*, 9282 – 9286.

[32] **Kol N., Adler-Abramovich L. and Barlam D.** (2005). Self-assembled peptide nanotubes are uniquely rigid bioinspired supramolecular structures. *Nano Letters*, *5(7)*, 1343-1346.

[33] **Niu L., Chen X., Allen S. and Tendler S.J.B** (2007). Using the Bending Beam Model to Estimate the Elasticity of Diphenylalanine Nanotubes. *Langmuir*, *23(*14*)*, 7443-7446.

[34] **Wang M., Xiong S., Wu X. and Chu P. K**. (2011). Effects of Water Molecules on Photoluminescence from Hierarchical Peptide Nanotubes and Water Probing Capability. *Small*, *7(19),* 2801–2807.

[35] **Heredia A., Bdikin I., Kopyl S., Mishina E., Semin S., Sigov A., … Kholkin A. L.** (2010). Temperature-driven phase transformation in self-assembled diphenylalanine peptide nanotubes. *Journal of Physics D: Applied Physics*, *43(*46*)*, 462001.

[36] **Ball P.** (2017). Water is an active matrix of life for cell and molecular biology. *Proceedings of the National Academy of Sciences*, *114(*51*)*, 13327–13335.

[37] **Franks F.** (1985) *Biophysics and Biochemistry at Low Temperatures. Cambridge*, Cambridge University Press.

[38] **Franks F.** (2000) *Water: A Matrix for Life*. 2nd edn, Cambridge, Royal Society of Chemistry.

[39] **Finney, J. L.** (2007). Bernal and the structure of water. *Journal of Physics: Conference Series, 57,* 40–52.

[40] **Martin F. and Zipse H.** (2005). Charge distribution in the water molecule - a comparison of methods. *Journal of computational chemistry, 26*, 97–105.

[41] **Clough S. A., Beers Y., Klein G. P. and Rothman L. S. (1973).** Dipole moment of water from stark measurements of H2O, HDO, and D2O. *J. Chem. Phys., 59(5)*, 2254–2259.

[42] **Xantheas S. S. and Dunning T. H.** (1993). Ab initio studies of cyclic water clusters (H2O)n, n=1–6. I. Optimal structures and vibrational spectra. *The Journal of Chemical Physics*, *99(*11*),* 8774–8792.

[43] **Pauling L.** (1988). *General Chemistry*. Dover Publications, Inc., New York.

[44] **Stillinger F. H.** (1980) Water revisited. *Science 209*, 451–457.

[45] **Finney J. L.** (2004). Water? What's so special about it? *Philosophical transactions of the Royal Society of London. Series B, Biological sciences*, *359(*1448*),*1145–1328.

[46] **Bernal J. D. and Fowler, R. H.** (1933). A Theory of Water and Ionic Solution, with Particular Reference to Hydrogen and Hydroxyl Ions. *The Journal of Chemical Physics*, *1(*8*),* 515–548.

[47] **Pauling L. (1935).** The Structure and Entropy of Ice and of Other Crystals with Some Randomness of Atomic Arrangement. *Journal of the American Chemical Society*, *57(*12*),* 2680–2684.

[48] **Bjerrum N.** (1952). Structure and Properties of Ice. *Science*, *115(*2989*),* 385–390.

[49] **Eisenberg D. and Kauzmann W.** (1969). *The Structure and Properties of Water*. Clarendon Press, Oxford

[50] **Debenedetti P. G.** (2003). Supercooled and glassy water. *Journal of Physics: Condensed Matter*, *15(*45*),* R1669.

[51] **Sciortino F., Geiger A. and Stanley, H. E.** (1991). Effect of defects on molecular mobility in liquid water. *Nature*, *354(*6350*),* 218–221.

[52] **Chaplin M.** (29.01.2020). Water Anomalies, *Water Structure and Science*, http://www1.lsbu.ac.uk/water/water_anomalies.html.

[53] **Fine R. A. and Millero F. J.** (1975). The high pressure properties of deuterium oxide. *The Journal of Chemical Physics*, *63*, 89–95.

[54] **Lifshitz E. M. and Pitaevskii** (1980) *Statistical Physics part 1*, 3rd edn, Pergamon, Oxford.

[55] **Errington J. R. and Debenedetti P. G.** (2001) Relationship between structural order and the anomalies of liquid water. *Nature*, *409*, 318.

[56] **Speedy R. J. and Angell C. A.** (1976). Isothermal compressiblity of supercooled water and evidence for a thermodynamic singularity at -45C. *Journal of Chemical Physics*, *65(*3*),* 851-858.

[57] **Rønne C., Åstrand P, and Keiding S. R.** (1999). THz Spectroscopy of Liquid H2O and D2O. *Phys. Rev. Lett., 82(*14*),* 2888-2891.

[58] **Debenedetti P. G.** (1996). *Metastable liquids: concepts and principles*, Princeton University Press**.**

[59] **Horst S.** (1991). *Glass – Nature, Structure, and Properties*, Springer, pp. 3–5.

[60] **Dehaoui A., Issenmann B., and Caupin F.** (2015). Viscosity of deeply supercooled water and its coupling to molecular diffusion. *Proceedings of the National Academy of Sciences*, *112(*39*),* 12020–12025.

[61] **Kobayashi M. and Tanaka H. (2011).** Relationship between the Phase Diagram, the Glass-Forming Ability, and the Fragility of a Water/Salt Mixture. *The Journal of Physical Chemistry B*, *115(*48*)*, 14077–14090.

[62] **Amann-Winkel K., Böhmer R., Fujara F., Gainaru C., Geil B., and Loerting T**. (2016). Colloquium: Water's controversial glass transitions. *Reviews of Modern Physics*, *88(1)*, 011002.

[63] **Johari G., Hallbrucker A., and Mayer E.** (1987). The glass–liquid transition of hyperquenched water. *Nature*, *330*, 552–553.

[64] **Hallbrucker A., Mayer E., and Johari G.** (1989). Glass-liquid transition and the enthalpy of devitrification of annealed vapor-deposited amorphous solid water: a comparison with hyperquenched glassy water. *The Journal of Physical Chemistry*, *93(*12*)*, 4986–4990.

[65] **Mishima O. and Stanley H. E.** (1989) The relationship between liquid, supercooled and glassy water. *Nature, 396*, 329—336 .

[66] **Velikov V., Borick S. and Angell C.A. (2001).** The glass transition of water, based on hyper- quenching experiment. *Science*, *294(*5550*),* 2335–2338.

[67] **Hestand N. J. and Skinner J. L. (2018).** Perspective: Crossing the Widom line in no man's land: Experiments, simulations, and the location of the liquid-liquid critical point in supercooled water. *The Journal of Chemical Physics*, *149(*14*)*, 140901.

[68] **Sellberg J. A., Huang C., Mcqueen T. A., Loh N. D., Laksmono H., Schlesinger D., … Nilsson A.** (2014). Ultrafast X-ray probing of water structure below the homogeneous ice nucleation temperature. *Nature*, *510(*7505*)*, 381–384.

[69] **Mishima O., Calvert L. and Whalley E.** (1984) Melting icei at 77 K and 10 kbar: a new method of making amorphous solids. *Nature*, *310*, 393–395.

[70] **Kim C. U., Barstow B., Tate M. V. and Gruner S. M.** (2009) Evidence for liquid water during the high-density to low-density amorphous ice transition. *Proc. Natl. Acad. Sci. U.S.A., 106*, 4596.

[71] **Winkel K., Elsaesser M., Mayer E. and Loerting T.** (2008) Water polyamorphism: Reversibility and (dis)continuity. *J. Chem. Phys., 128*, 044510.

[72] **Koza, M., Schober, H., Fischer, H., Hansen, T., and Fujara, F.** (2003) Kinetics of the high-to low-density amorphous water transition. *Journal of Physics: Condensed Matter*, *15*, *321*.

[73] **Mishima O. and Suzuki Y.** (2002). Propagation of the polyamorphic transition of ice and the liquid–liquid critical point. *Nature*, *419*, 599–603.

[74] **Sastry S., Debenedetti P. G., Sciortino F. and Stanley, H. E.** (1996). Singularity-free interpretation of the thermodynamics of supercooled water. *Phys. Rev. E*, *53*, 6144.

[75] **Giovambattista N, Loerting T, Lukanov BR and Starr FW** (2012). Interplay of the glass transition and the liquid-liquid phase transition in water. *Scientific Rep*, *2*, 390.

[76] **Loerting T., Fuentes-Landete V., Handle P. H., Seidl M., Amann-Winkel K., Gainaru C. and Böhmer R.** (2015). The glass transition in high-density amorphous ice. *Journal of Non-Crystalline Solids*, *407*, 423–430.

[77] **Poole P. H., Sciortino F., Essmann U. and Stanley H. E.** (1992). Phase behaviour of metastable water. *Nature*, *360*, 324-328.

[78] **Holten, V., Bertrand, C. E., Anisimov, M. A., and Sengers, J. V.** (2012). Thermodynamics of supercooled water. *J. Chem. Phys., 136*, 094507.

[79] **Honerkamp-Smith A. R., Veatch S. L. and Keller S. L.** (2009). An introduction to critical points for biophysicists; observations of compositional heterogeneity in lipid membranes. *Biochimica Et Biophysica Acta (BBA) - Biomembranes*, *1788(1), 53–63.

[80] **Kumar P., Buldyrev S. V., Starr F. W., Giovambattista N. and Stanley H. E.** (2005). Thermodynamics, structure, and dynamics of water confined between hydrophobic plates.*Physical Review E*, *72*, 051503.

[81] **Franzese G. and Stanley H. E.** (2007). The widom line of supercooled water. *J. Phys.: Condens. Matt.*, *19*, 205126.

[82] **Biddle J. W., Holten V. and Anisimov M. A.,** (2014). Behavior of supercooled aqueous solutions stemming from hidden liquid–liquid transition in water. *J. Chem. Phys., 141*, 074504.

[83] **Kumar P.** (2006). Breakdown of the Stokes-Einstein relation in supercooled water. *Proceedings of the National Academy of Sciences*, *103(35)*, 12955–12956.

[84] **Ito K., Moynihan C. T. and Angell C. A.** (1999). Thermodynamic determination of fragility in liquids and a fragile-to-strong liquid transition in water. *Nature*, *398(6727)*, 492–495.

[85] **Gallo P. and Rovere M.** (2012). Mode coupling and fragile to strong transi- tion in supercooled TIP4P water. *J. Chem. Phys. 137*, 164503.

[86] **Starr F. W., Sciortino F. and Stanley H. E.** (1999). Dynamics of simulated water under pressure. *Phys. Rev. E*, *60*, 6757.

[87] **Hansen J.-P. and McDonald I. R.** (1990). *Theory of simple liquids*. Jordan Hill, Elsevier Science.

[88] **Faraone A., Liu L., Mou C.-Y., Yen C.-W. and Chen S.-H.** (2004) Fragile-to-strong liquid transition in deeply supercooled confined water. *J. Chem. Phys.*, *121*, 10843.

[89] **Chen S.-H., Mallamace F., Mou C.-Y., Broccio M., Corsaro C., Faraone A., and Liu L**. (2006). The violation of the Stokes-Einstein relation in supercooled water. *Proceedings of the National Academy of Sciences*, *103(35)*, 12974–12978.

[90] **Cerveny S., Mallamace F., Swenson J., Vogel M., and Xu L.** (2016). Confined Water as Model of Supercooled Water. *Chemical Reviews*, *116(*13*)*, 7608–7625.

[91] **Swenson J., Elamin K., Jansson H. and Kittaka, S**. (2013). Why is there no clear glass transition of confined water? *Chemical Physics*, *424*, 20–25.

[92] **Takahara S., Nakano M., Kittaka S., Kuroda Y., Mori T., Hamano H. and Yamaguchi, T.** (1999). Neutron Scattering Study on Dynamics of Water Molecules in MCM-41. *J. Phys. Chem. B*, *103(*28*)*, 5814− 5819.

[93] **Swenson J. and Cerveny S.** (2014). Dynamics of deeply supercooled interfacial water. *Journal of Physics: Condensed Matter*, *27(*3*)*, 033102.

[94] **Jansson H., Bergman R. and Swenson, J.** (2011). Role of Solvent for the Dynamics and the Glass Transition of Proteins. *The Journal of Physical Chemistry B*, *115(*14*),* 4099–4109.

[95] **Jähnert S., Chávez F. V., Schaumann G. E., Schreiber A., Schönhoff M. and Findenegg G. H.** (2008). Melting and freezing of water in cylindrical silica nanopores. *Physical Chemistry Chemical Physics*, *10(*39*)*, 6039.

[96] **Yoshida K., Yamaguchi T., Kittaka S., Bellisent-Funel M. and Fouquet P.** (2008). Thermodynamic, structural and dynamics properties of supercooled water confined in mesoporous MCM-41 studied with calorimetric. *Neutron Diffraction, and Neutron Spin Echo Measurements*, *129(*5*)*, 054702.

[97] **Mallamace F., Broccio M., Corsaro C., Faraone A., Majolino D., Venuti V., … Chen S.-H.** (2006). Evidence of the existence of the low-density liquid phase in supercooled, confined water. *Proceedings of the National Academy of Sciences*, *104(*2*)*, 424–428.

[98] **Liu L., Chen S.-H., Faraone A., Yen C.-W. and Mou C.-Y.** (2005). Pressure dependence of fragile-to-strong transition and a possible second critical point in supercooled confined water. *Phys. Rev. Lett. 95*, 117802.

[99] **Jansson H. and Swenson J.** (2003). Dynamics of water in molecular sieves by dielectric spectroscopy. *The European Physical Journal E - Soft Matter*, *12(*0*)*, 51–54.

[100] **Stefanutti E., Bove L. E., Alabarse F. G., Lelong G., Bruni F. and Ricci M. A.** (2019). Vibrational dynamics of confined supercooled water. *The Journal of Chemical Physics*, *150(*22*)*, 224504.

[101] **Roussenova M., Alam M. A., Townrow S., Kilburn D., Sokol P. E., Guillet-Nicolas R. and Kleitz F.** (2014). A nano-scale free volume perspective on the glass transition of supercooled water in confinement. *New Journal of Physics*, *16(*10*)*, 103030.

[102] **Mallamace F., Chen S.-H., Broccio M., Corsaro C., Crupi V., Majolino D., … Stanley H. E.** (2007). Role of the solvent in the dynamical transitions of proteins: The case of the lysozyme-water system. *The Journal of Chemical Physics*, *127(*4*)*, 045104.

[103] **Brubach J.-B., Mermet A., Filabozzi A., Gerschel A. and Roy, P.** (2005). Signatures of the hydrogen bonding in the infrared bands of water. *The Journal of Chemical Physics*, *122(*18*)*, 184509.

[104] **Li F. and Skinner J. L.** (2010). Infrared and Raman line shapes for ice Ih. II. H2O and D2O. *The Journal of Chemical Physics*, *133(24)*, 244504.

[105] **Kremers F. and Schönhals A.** (2003). *Broadband Dielectric Spectroscopy. Springer-Verlag*. Berlin Heidelberg

[106] **Debye P.** (1913). *Ver. Deut. Phys. Gesell. 15*, 777; reprinted 1954 in collected papers of Peter J.W. Debye. Interscience, New York

[107] **Havriliak S. and Negami S.** (1967). A complex plane representation of dielectric and mechanical relaxation processes in some polymers. *Polymer, 8*, 161–210.

[108] **Arrhenius S. A.** (1889). Über die Dissociationswärme und den Einfluß der Temperatur auf den Dissociationsgrad der Elektrolyte. *Z. Phys. Chem. 4,* 96–116.

[109] **Vogel H.,** (1921). The law of the relation between the viscosity of liquids and the temperature. *Phys. Z, 22*, 645.

[110] **Fulcher, G. S.** (1925). Analysis of recent measurements of the viscosity of glasses. *Journal of the American Ceramic Society*, *8(6),* 339-355.

[111] **Ryabov Y., Gutina A., Arkhipov V. and Feldman, Y.** (2001). Dielectric relaxation of water absorbed in porous glass. *The Journal of Physical Chemistry B*, *105(9)*, 1845-1850.

[112] **Ryabov Y. E., Puzenko A. and Feldman, Y.** (2004). Nonmonotonic relaxation kinetics of confined systems. *Physical Review B, 69(1)*, 014204.

[113] **URL** http://www.novocontrol de

[114] **Johari G. P.** (2000). On the amorphization of hexagonal ice, the nature of water's low density amorph, and continuity of molecular kinetics in supercooled water. Invited Lecture. *Physical Chemistry Chemical Physics*, *2(8)*, 1567-1577

[115] **Johari G. P**. (2003). Water's T_g-endotherm, sub-T_g peak of glasses and T_g of water. *The Journal of chemical physics*, *119(5)*, 2935-2937.

[116] **Ferreira P. M. G. L., Ishikawa M. S., Kogikoski S., Alves W. A. and Martinho, H. (2015).** Relaxation dynamics of deeply supercooled confined water in L, L-diphenylalanine micro/nanotubes. *Physical Chemistry Chemical Physics*, *17(48)*, 32126-32131.

[117] **Cui H., Zhou B., Long L. S., Okano Y., Kobayashi H. and Kobayashi A. (2008).** A porous coordination-polymer crystal containing one-dimensional water chains exhibits guest-induced lattice distortion and a dielectric anomal. *Angewandte Chemie International Edition*, *47(18)*, 3376-3380.

[118] **Gutina A., Axelrod E., Puzenko A., Rysiakiewicz-Pasek E., Kozlovich N., and Feldman Y.** (1998). Dielectric relaxation of porous glasses. *Journal of non-crystalline solids*, *235*, 302-307.

[119] **Frunza L., Kosslick H., Frunza S., Fricke R. and Schönhals A.** (2002). On the mobility of sodium ions and of confined liquid crystals in molecular sieves of faujasite type. *Journal of non-crystalline solids*, *307*, 503-509.

[120] **Cerveny S., Barroso-Bujans F., Alegria A. and Colmenero, J.** (2010). Dynamics of water intercalated in graphite oxide. *The Journal of Physical Chemistry C*, *114(6)*, 2604-2612.

[121] **Monasterio M., Gaitero J. J., Manzano H., Dolado J. S. and Cerveny S.** (2015). Effect of chemical environment on the dynamics of water confined in calcium silicate minerals: natural and synthetic tobermorite. *Langmuir*, *31(17)*, 4964-4972.

[122] **Adrjanowicz K., Kolodziejczyk K., Kipnusu W. K., Tarnacka M., Mapesa E. U., Kaminska E., ... Paluch M.** (2015). Decoupling between the Interfacial and Core Molecular Dynamics of Salol in 2D Confinement. *The Journal of Physical Chemistry C*, *119(25)*, 14366-14374.

[123] **Scoppola E., Sodo A., McLain S. E., Ricci M. A. and Bruni, F.** (2014). Water-peptide site-specific interactions: A structural study on the hydration of glutathione. *Biophysical journal*, *106(8)*, 1701-1709.

[124] **Barut G., Pissis P., Pelster R. and Nimtz, G.** (1998). Glass transition in liquids: two versus three-dimensional confinement. *Physical review letters*, *80(16)*, 3543.

[125] **Alcoutlabi M. and McKenna G. B.** (2005). Effects of confinement on material behaviour at the nanometre size scale. *Journal of Physics: Condensed Matter*, *17(15)*, R461.

[126] **Chonde M., Brindza M. Sadtchenko V.** (2006). Glass transition in pure and doped amorphous solid water: An ultrafast microcalorimetry study. *The Journal of Chemical Physics, 125(9)*, 094501.

[127] **Esin A., Baturin I., Nikitin T., Vasilev S., Salehli F., Shur V. Y. and Kholkin A. L.** (2016). Pyroelectric effect and polarization instability in self-assembled diphenylalanine microtubes. *Applied Physics Letters*, *109(14)*, 142902.

[128] **Ravikumar B., Rajaram R. K. and Ramakrishnan V.** (2006). Raman and IR spectral studies of L-phenylalanine L-phenylalaninium dihydrogenphosphate and DL-phenylalaninium dihydrogenphosphate. *Journal of Raman Spectroscopy: An International Journal for Original Work in all Aspects of Raman Spectroscopy, Including Higher Order Processes, and also Brillouin and Rayleigh Scattering*, *37(5)*, 597-605.

[129] **Bystrov V. S., Kopyl S. A., Zelenovskiy P., Zhulyabina O. A., Tverdislov V. A., Salehli F., ... and Kholkin A. L.** (2018). Investigation of physical properties of diphenylalanine peptide nanotubes having different chiralities and embedded water molecules. *Ferroelectrics*, *525(1)*, 168-177.

[130] **Ohno K., Okimura M., Akai N. and Katsumoto Y.** (2005). The effect of cooperative hydrogen bonding on the OH stretching-band shift for water clusters studied by matrix-isolation infrared spectroscopy and density functional theory. *Physical Chemistry Chemical Physics*, *7(16)*, 3005-3014.

[131] **Reátegui E. and Aksan A.** (2009). Effects of the low-temperature transitions of confined water on the structures of isolated and cytoplasmic proteins. *The Journal of Physical Chemistry B*, *113(39)*, 13048-13060.

[132] **Xu L., Kumar P., Buldyrev S. V., Chen S. H., Poole P. H., Sciortino F. and Stanley, H. E.** (2005). Relation between the Widom line and the dynamic crossover in systems with a liquid–liquid phase transition. *Proceedings of the National Academy of Sciences*, *102(46)*, 16558-16562.

[133] **Crupi V., Longo F., Majolino D. and Venuti, V.** (2006). Vibrational properties of water molecules adsorbed in different zeolitic frameworks. *Journal of Physics: Condensed Matter*, *18(*15*)*, 3563.

[134] **Meister K., Strazdaite S., DeVries A. L., Lotze S., Olijve L. L., Voets I. K. and Bakker H. J.** (2014). Observation of ice-like water layers at an aqueous protein surface. *Proceedings of the National Academy of Sciences*, *111(50)*, 17732-17736.

[135] **Maeda Y., Nakamura T. and Ikeda, I.** (2001). Changes in the hydration states of poly(N-alkylacrylamide) during their phase transitions in water observed by FTIR spectroscopy. *Macromolecules*, *34(5)*, 1391-1399.

[136] **Mallamace F., Corsaro C. and Stanley, H. E.** (2013). Possible relation of water structural relaxation to water anomalies. *Proceedings of the National Academy of Sciences*, *110(*13*)*, 4899-4904.

[137] **Middleton D. A., Madine J., Castelletto V. and Hamley, I. W.** (2013). Insights into the molecular architecture of a peptide nanotube using FTIR and solid-state NMR spectroscopic measurements on an aligned sample. *Angewandte Chemie International Edition*, *52(40)*, 10537-10540.

[138] **Mallamace F., Corsaro C., Mallamace D., Vasi S., Vasi C. and Dugo, G.** (2015). The role of water in protein's behavior: The two dynamical crossovers studied by NMR and FTIR techniques. *Computational and structural biotechnology journal*, *13*, 33-37.

[139] **Lekprasert B., Korolkov V., Falamas A., Chis V., Roberts C. J., Tendler S. J. and Notingher I.** (2012). Investigations of the supramolecular structure of individual diphenylalanine nano-and microtubes by polarized Raman microspectroscopy. *Biomacromolecules*, *13(*7*)*, 2181-2187.

APPENDICES

APPENDIX A: RMS Values of Applied Fitting Procedures

APPENDIX A

Table A.1. Root mean square values Gaussian deconvolution procedures for FTIR spectra in each temperature and specified vibration band regions.

Temperature (K)	RMS (OH-Stretching)	RMS (CH-Stretching)	RMS (OH-Bending/Amides)
88	0,000164	0,000096	0,006118
98	0,000166	0,000101	0,004819
108	0,000169	0,000115	0,004171
118	0,000252	0,000101	0,004101
123	0,000171	0,000128	0,004065
128	0,000164	0,000115	0,004064
133	0,000169	0,000116	0,004051
138	0,000166	0,000129	0,004064
143	0,000254	0,000156	0,004068
148	0,000178	0,000116	0,004073
153	0,000166	0,000118	0,00408
158	0,000272	0,000161	0,004074
163	0,00028	0,000157	0,004084
168	0,000249	0,00019	0,004071
173	0,000281	0,000181	0,004057
178	0,000252	0,00021	0,004029
183	0,000236	0,00023	0,00402
188	0,000346	0,000226	0,00402
193	0,001682	0,000253	0,004021
198	0,001215	0,000174	0,00402
203	0,000721	0,000222	0,004026
208	0,00047	0,00023	0,004028
213	0,000434	0,00026	0,00402
218	0,00044	0,000278	0,003979
223	0,0004	0,000248	0,003947
228	0,000402	0,000203	0,003932
233	0,000392	0,000209	0,004489
238	0,000246	0,000141	0,005302
243	0,000149	0,000263	0,00608
248	0,000151	0,000061	0,006809
253	0,00023	0,000214	0,007326
258	0,000233	0,000049	0,007889
263	0,000165	0,000116	0,00816
268	0,000162	0,000082	0,008372
273	0,000159	0,0001	0,008582
278	0,00016	0,000118	0,008725
283	0,00023	0,000094	0,008719
288	0,000227	0,000082	0,0082415

Table A.2. Root mean square values of Havriliak-Negami fitting procedures of dielectric loss spectra in specified temperatures

Temperature (K)	RMS	Temperature (K)	RMS
143	1,02E-04	236	2,48E-04
146	1,09E-04	239	3,05E-04
149	8,75E-05	242	3,02E-04
152	1,05E-04	245	2,90E-04
155	1,20E-04	248	2,24E-04
158	9,79E-05	251	2,31E-04
161	7,06E-05	254	3,29E-04
164	8,19E-05	257	2,56E-04
167	7,34E-05	260	3,90E-04
170	8,00E-05	263	3,55E-04
173	1,05E-04	266	3,83E-04
176	1,16E-04	269	3,55E-04
179	1,31E-04	272	3,61E-04
182	1,26E-04	275	3,82E-04
185	1,92E-04	278	5,53E-04
188	2,59E-04	281	5,68E-04
191	1,48E-04	284	5,62E-04
194	1,41E-04	287	6,14E-04
197	1,58E-04	290	5,89E-04
200	1,37E-04	293	5,68E-04
203	1,50E-04	296	5,29E-04
206	1,68E-04	299	5,59E-04
209	1,90E-04	302	7,82E-04
212	1,62E-04	305	1,01E-03
215	2,59E-04	308	1,10E-03
218	3,63E-04	311	6,98E-04
221	4,51E-04	314	5,60E-04
224	6,36E-04	317	6,07E-04
227	6,69E-04	320	6,31E-04
230	1,86E-04	323	5,42E-04
233	2,19E-04		

CURRICULUM VITAE

Name Surname	**:**	Abuzer Orkun Aydın
Place and Date of Birth	**:**	Bakırköy/İstanbul 06.05.1991
E-Mail	**:**	aydinab@itu.edu.tr

EDUCATION **:**

- **B.Sc.** **:** 2016, Istanbul Technical University, Faculty of Science and Letters, Physics Engineering Department

PROFESSIONAL EXPERIENCE AND REWARDS:

- 2017-2020: TÜBİTAK 115F227 joint project with Portugese on "Phase transitions of self-assembling peptide nanotubes"

PUBLICATIONS, PRESENTATIONS AND PATENTS ON THE THESIS:

- **Aydın, A.O., Salehli, F., Kopyl, S., Kholkin, A., (2020).** Phase Transitions in self-assembled diphenylalanine nanotube/microtubes, investigated by broad temperature FTIR**.** DPG 2020, DRESDEN.